Preface to the tenth volume of Express Polymer Letters

*T. Czigány**

Department of Polymer Engineering, Faculty of Mechanical Engineering, Budapest University of Technology and Economics, Műegyetem rkp. 3., H-1111, Budapest, Hungary

Dear Readers,
The editorial of the first issue of the tenth volume provides a short review of the results and statistics of the previous years. 931 articles were published in the past 9 years, a mere 16% of the submitted ones. 84% was rejected, although a part of them contained results of the acceptable high quality, but we strove to select only cutting edge topics. This is reflected in the fact that about 60% of the articles published in **eXPRESS Polymer Letters** has been downloaded at least 1000 times, which means that these topics attracted the attention of our readers. The download statistics are also reflected in the number of citations. The most downloaded article is *Starch-based completely biodegradable polymer materials* (DOI: 10.3144/expresspolymlett.2009.46), with about 11 000 downloads. *The most cited article in the Web of Science* (WoS) is *The present status and key problems of carbon nanotube based polymer composites* (DOI: 10.3144/expresspolymlett.2007.39), which has already 178 citations. Further seven articles have more than ten citations per annum with the following titles: *Self healing in polymers and polymer composites. Concepts, realization and outlook: A review* (DOI: 10.3144/expresspolymlett.2008.29); *Advances in synthetic optically active condensation polymers – A review* (DOI: 10.3144/expresspolymlett.2011.15); *Dielectric relaxations in PVDF/BaTiO₃ nanocomposites* (DOI: 10.3144/expresspolymlett.2008.35); *Raman spectroscopic characterization of multiwall carbon nanotubes and of composites* (DOI: 10.3144/expresspolymlett.2012.63); *How carbon nanotubes affect the cure kinetics and glass transition temperature of their epoxy composites? – A review* (DOI: 10.3144/expresspolymlett.2009.73); *Multi-walled carbon nanotube filled polypropylene nanocomposites based on masterbatch route: Improvement of dispersion and mechanical properties through PP-g-MA addition* (DOI: 10.3144/expresspolymlett.2008.87); *Crystallization kinetics of poly(lactic acid)-talc composites* (DOI: 10.3144/expresspolymlett.2011.84).

The journals which cite the articles of **eXPRESS Polymer Letters** most frequently are Polymer, Journal of Applied Polymer Science and Macromolecules. The h-index of **eXPRESS Polymer Letters** in WoS is 37, the present impact factor is 2.761. This indicator is being presently fiercely attacked but we consider it important as it is still one of the most important evaluation tools of scientific journals. Impact factor is a helpful compass for the young scientist generation to evaluate the relative rank and quality of various journals. Otherwise, there would be no quality-related orientation where to send their manuscripts. Additionally, nowadays the internet is full of 'predator' journals having titles, appearance and websites which resemble those of high quality journals with good impact factors, and WoS can help to exclude these journals.

When launching the 10th volume of **eXPRESS Polymer Letters** I wish all authors, readers and referees a successful new year and achievement of highly cited research results. Sincerely yours,

Prof. Dr. Tibor Czigány
editor

*Corresponding author, e-mail: czigany@eik.bme.hu

ESR investigation of NR and IR rubber vulcanized with different cross-linking agents

P. Posadas[1*], M. A. Malmierca[1], A. González-Jiménez[1], L. Ibarra[1], A. Rodríguez[1], J. L. Valentin[1], T. Nagaoka[2], H. Yajima[2], S. Toki[3], J. Che[4], L. Rong[4], B. S. Hsiao[4]

[1] Instituto de Ciencia y Tecnología de Polímeros (CSIC) C/ Juan de la Cierva, 3. 28006 Madrid, Spain
[2] Department of Chemistry, Tokyo University of Science, Shinjuku-ku, 162-9601 Tokyo, Japan
[3] National Metal and Materials Technology Center, Mahidol university, Salaya campus, 73170 Nakhon Pathm, Thailand
[4] Department of Chemistry, State University of New York, Stony Brook, 11794-3400 New York, USA

Abstract. This study evaluates the formation of radical species in natural rubber (NR) and poly-isoprene rubber (IR) during the vulcanization process and the uniaxial deformation of the formed networks by means of Electron Spin Resonance (ESR). Vulcanization of NR and IR always shows a radical pathway, where the different vulcanization systems dictate the concentration of radical species in the course of this complex process. The greatest concentration of radicals were detected during the vulcanization with sulfur/accelerator based on efficient systems (EV), followed by conventional (CV) and sulfur donor systems, whereas azide and organic peroxide agents showed smaller concentration of radicals. Independently of the vulcanization system, certain amount of radicals was detected on the vulcanized samples after the end of the vulcanization process. Comparison between different matrices demonstrates that NR always shows higher concentration of radicals than IR in the vulcanization process as well as during uniaxial deformation, fact that could be associated to the presence of non-rubber components in NR.

Keywords: rubber, vulcanization, electron spin resonance

1. Introduction

Technical application of rubbers requires the vulcanization process to create a three dimensional polymer network which provides the characteristic elastic properties of these materials. Depending on the vulcanization system and the type of rubber, in addition to vulcanization conditions, the chemistry of this process changes, having important consequences on the network structure and consequently, on the elastic properties of these rubber materials. The most common vulcanization agents on rubber technology are sulfur and organic peroxides. In the case of sulfur systems, the discussion concerning the nature of the reactions involved in the vulcanization process, i.e. ionic or free radical pathways,

is still ongoing [1–4]. Several works conclude that radical mechanisms are required to justify the cross-link structures formed on NR after the vulcanization with sulfur [2–6]: sulfur cross-links of different lengths, mainly polysulfidic bonds, pendant groups, cyclic sulfides and cis/trans isomerization of the double bonds and/or conjugated sequences in the polymer backbone [7]. In addition, the low reaction efficiency and the long time required to complete vulcanization process do not recommend the use of sulfur without accelerators for commercial purposes [6]. The sulfur-accelerator systems reduce the optimum vulcanization time, improve the elastic properties of NR and minimize the side-reactions during the vulcanization process. They are classi-

fied as conventional (CV), semi-efficient (semi-EV) and efficient (EV) systems depending on the accelerator/sulfur ratio (usually in a range between 0.2 and 12, for the extreme cases). The NR samples usually show different and characteristic mechanical and viscoelastic properties, fatigue and ageing resistance according to the sulfur/accelerator system employed in the vulcanization process [1, 7]. On the other hand, vulcanization of NR with organic peroxides provides materials with higher concentration of non-elastic network defects and rubber network structures characterized by the formation of C–C cross-links with more heterogeneous spatial distribution, as compared to the samples vulcanized with sulfur-accelerators [6]. These structural differences have a critical impact on the drop of elastic properties of these materials, being caused by the complex free radical mechanism (with different radical pathways and side reactions) that characterizes the vulcanization of NR with organic peroxides. Nevertheless, peroxide crosslinking has also several advantages in comparison with sulfur cure with regard to different applications of the rubbers (e.g., compression set at elevated temperatures, co-vulcanization, etc.) [8]. According to this statement, the main objective of this work is to determine the presence and concentration of free radicals on the vulcanization process of NR and poly-isoprene rubber concerning the different vulcanization systems and their influence on the network structure and physical properties of NR. In this sense, Electron Spin Resonance (ESR) is a powerful and unique tool for detecting radicals. ESR has been previously used to evaluate the radical concentration on polyolefins and different rubbers [9–12] vulcanized with organic peroxides. The application to other vulcanization systems, e.g. sulfur based systems, has been limited to model compounds or the analysis of the vulcanization system without rubber [1]. Recently, ESR has been applied to study the polybutadiene vulcanization mechanism [13].

In addition to the study of vulcanization process, the second part of this work will be focused on the study of radicals generated during uniaxial deformation of NR [14], fact that could be related with variations in the network structure and consequently in the final properties of NR after cycles of deformation.

2. Experimental section
2.1. Materials, preparation of samples and rheological measurements

The studied compounds were based on standardized natural rubber (SMRCV60), kindly supplied by Malaysian Rubber, Kuala Lumpur, Malaysia and poly cis-1,4-polyisoprene (IR) kindly supplied by Kraton Polymers, Amsterdam, The Netherlands (KRATON® IR307). Five different vulcanization systems were used in this work: two sulfur based systems with different accelerator/sulfur ratios (A/S) which correspond to a conventional system (named CV with A/S = 0.2) and an efficient system (named EV with A/S = 0.2), respectively; a sulfur donor system (DPTT), an organic peroxide (DCP) and a diazide molecule (BSA) as it was reported in Table 1.

For the ESR measurements during the vulcanization process, samples were prepared in toluene solutions

Table 1. Recipes of the samples

	NR-DPTT	NR-CV	NR-EV	NR-BSA	NR-DCP	IR-DPTT	IR-CV	IR-EV	IR-BSA	IR-DCP
NR			100					—		
IR			—					100		
Zinc oxide*	5	5	5	–	–	5	5	5	–	–
Stearic acid*	1	1	1	–	–	1	1	1	–	–
DPTT[a]	5	–	–	–	–	5	–	–	–	–
Sulfur*	–	2.5	0.56	–	–	–	2.5	0.56	–	–
CBS[b]	–	0.5	6.72	–	–	–	0.5	6.72	–	–
A/S[c]	–	0.2	12	–	–	–	0.2	12	–	–
BSA[d]	–	–	–	3.13	–	–	–	–	3.13	–
DCP[e]	–	–	–	–	1.4	–	–	–	–	1.4

[a]Dipentamethylene thiuram tetrasulfide
[b]N-cyclohexyl-2-bezonthiazole sulfenamide
[c]Accelerator/sulfur rate
[d]Benzene-1,3-disulphonylazide prepared by reacting 1,3 benzene dicloro-sulfonyl with sodium azide in our laboratory [15]
[e]Bis (1-methyl-1-phenylethyl) peroxide (Dicumyl peroxide, (DCP), 97% purity) which was supplied by Merck KGaA (Darmstadt, Germany) and it was used as received
*Sulfur, zinc oxide and stearic acid were supplied by Sigma-Aldrich.

(5% in volume) according the recipes summarized in Table 1. Finally rubber films with thickness about 0.5 mm were obtained by casting. Rubber films were dried at room temperature until constant weight.

For other measurements, the rubber compounding was executed on a laboratory two-roll mill with a cylinder diameter of 15 cm, a length of 30 cm and a friction ratio between them of 1:1.15, following the habitual protocol employed in rubber science and technology. Rolls were kept at 40–50 °C during the mixing procedure.

Vulcanization of rubber samples was executed using a hydraulic press heated by electric resistances at 150 °C at their respective optimum vulcanization time (t_{97}), whereas the samples vulcanized with azides were vulcanized at 105 °C at their corresponding t_{97}.

Vulcanization time was determined by the torque-time curve obtained from the Monsanto Moving Die Rheometer, model MDR 2000E. These vulcanization curves were used to obtain the optimum vulcanization time, t_{97}, defined as the time required for reaching the 97% of the maximum elastic torque.

2.2. Determination of cross-link density

Cross-link densities were determined by equilibrium swelling measurements. Equilibrium swelling experiments in toluene were performed according to the protocol described elsewhere [16]. The solvent density $\rho_s = 0.87$ g/mL was used for toluene. The influence of insoluble components (such as zinc oxide) was corrected according to Equation (1) [16]:

$$V_{rubber} = \frac{w_d}{\rho_{rubber}} - \left[w_d \cdot \left(\frac{w_{ZnO}}{w_{compound}} \right) \cdot \frac{1}{\rho_{ZnO}} \right] \quad (1)$$

where w_d is the sample weight after drying, ρ_{rubber} is the density of NR (0.92 g/cm^3); w_{ZnO} is the ZnO weight, $w_{compound}$ is the recipe weight and ρ_{ZnO} is the density of ZnO (5.6 g/cm^3).

Assuming an affine model to characterize the elastic behavior of swollen networks, cross-link density (ν) was obtained by using the Flory-Rehner equation (Equation (2)) [17]:

$$\nu \left[\frac{mole}{cm^3} \right] = \frac{-\left[\ln(1 - V_{rubber}) + V_{rubber} + \chi V_{rubber}^2 \right]}{V_1 \left[V_{rubber} - \dfrac{V_{rubber}}{2} \right]} \quad (2)$$

where V_{rubber} is the volume fraction of polymer in the swollen mass, V_1 is the molar volume of the solvent

and χ is the Flory-Huggins polymer-solvent interaction parameter.

It is well known that the χ parameter depends on the solvent-rubber pair and the volumetric fraction of rubber. For this reason a variable χ parameter has been used according to the recommendations made elsewhere [16].

2.3. Electron spin resonance (ESR) experiments

Electron spin resonance (ESR) measurements were performed on a JEOL spectrometer ES-FA200 X-band. The external standard of ESR spectrum for g-value and line width were the third and fourth resonant lines of Mn^{2+}, which were at 2.034 and 1.981, respectively. The sweep time was 30 seconds. Two accumulations were enough to get an ESR absorption curve with high signal to noise ratio. A double integration of the first derivative curve of ESR signal at room temperature from benzene solution of 4-hidroxy-2,2,6,6,-tetramethyl piperidinooxyl radical (TEMPOL) with a known radical concentration was used as a standard to calculate the radical concentration of rubber samples [14, 18–20]. The radical concentration is defined per gram of rubber.

Measurements on un-vulcanized rubber films in order to evaluate the formation of radicals during the vulcanization process were performed at 150 °C, except azide sample where the temperature was 105 °C. We decided the starting time as fast as the sample is set in the chamber since the temperature of the sample reach the setting temperature easily due to the thinness of the sample (0.5 mm) and measuring time (1 minute), although the data in initial one minute has some uncertainty necessarily.

Measurements of vulcanized rubbers under deformation were carried out by a home-built stretching machine combined with the ESR instrument at room temperature. Samples were stretched under a constant stretching speed of 10 mm/min up to a desired strain while ESR measurements were taken. The strain was increased up to 200% which was the maximum strain due to an instrumental limitation. Details for measurements were described elsewhere [21].

3. Results
3.1. Formation and evolution of free radicals during the vulcanization process

The vulcanization process for IR and NR was monitored by their corresponding rheometer curves as

shown in Figure 1. Both rubber matrices show similar trends in the vulcanization curves for the different systems.

The DPTT system shows the fastest cross-linking reaction and together with the EV system are characterized by higher increment of torque (associated to the formation of cross-links between the rubber chains, as it is shown in Table 2) as compared with the other vulcanization systems. Although both systems show some reversion in the vulcanization curve, i.e. decrease in the torque after reaching the maximum value, the sample vulcanized with CV system presents the highest reversion. This process has been related with rubber chain scission and the breaking down of cross-links during the vulcanization process. In the samples vulcanized with low A/S ratio this phenomenon is more evident because of the thermolability of polysulfidic bonds which are predominant for CV systems [22].

Opposite to sulfur/accelerator systems, the vulcanization with peroxide (DCP) does not show any scorch time, because the cross-linking reaction takes place immediately after the fast homolytic decomposition of DCP at the vulcanization temperature. In a similar way, the scorch time for DPTT system is very short and it is not recorded by the rheometer [23].

The main goal of this investigation is to evaluate the formation of free radicals during the vulcanization process according to the different vulcanization systems. For this reason, ESR experiments were performed on uncured compounds at the same temperature as the rheometer curves, e.g. 150 °C for all samples with exception of samples vulcanized with BSA which were measured at 105 °C. For that reason the results extracted from the rheometer could be used to understand the ESR measurements.
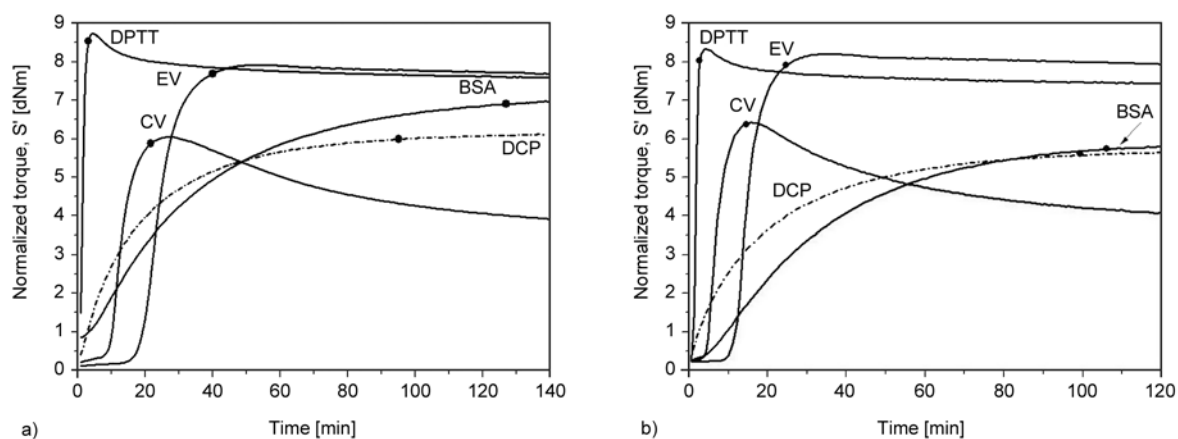
3.1.1. Peroxide system

Figure 2 shows the first derivative of the ESR spectra for IR and NR samples vulcanized with DCP at different vulcanization times. The graph shows the magnetic field range from 318 to 326 H/mT.

Independently of the vulcanization time, it is possible to identify four peaks for the IR sample (Figure 2a), in a similar way as in the case of polyolefins crosslinked with DCP [10].

The mechanism of peroxide vulcanization is clearly based on free radical pathways. It is initiated by the thermal homolytic scission of the peroxide molecule, creating two radicals. These radicals are able to react with diene polymer backbones (e.g. IR and NR) via abstraction of the more labile allylic hydrogen atoms or via addition to the double bonds, forming polymer radicals. In the simplest cross-linking reaction (ignoring numerous other side reactions that do not generate junctions between rubber chains), two competing termination reactions may take place [8, 24–26]. On one hand, recombination of two polymer radicals to form a tetra-functional carbon-carbon cross-link and on the other hand, addition of one polymer radical to a double bond of another rubber

Table 2. densities of the samples vulcanized at their optimum vulcanization times measured by swelling experiments

Samples NR	Crosslink density [mol/cm^3·10^5]	Samples IR	Crosslink density [mol/cm^3·10^5]
DPTT	10.41±0.03	DPTT	10.3±0.2
CV	6.64±0.03	CV	6.24±0.03
EV	8.84±0.02	EV	8.4±0.2
BSA	6.8±0.3	BSA	7.2±0.3
DCP	5.49±0.09	DCP	6.3±0.2

Figure 1. Rheometric curves a) IR samples. b) NR samples. Symbols (●) indicate the optimum vulcanization time (t_{97}) for each sample.
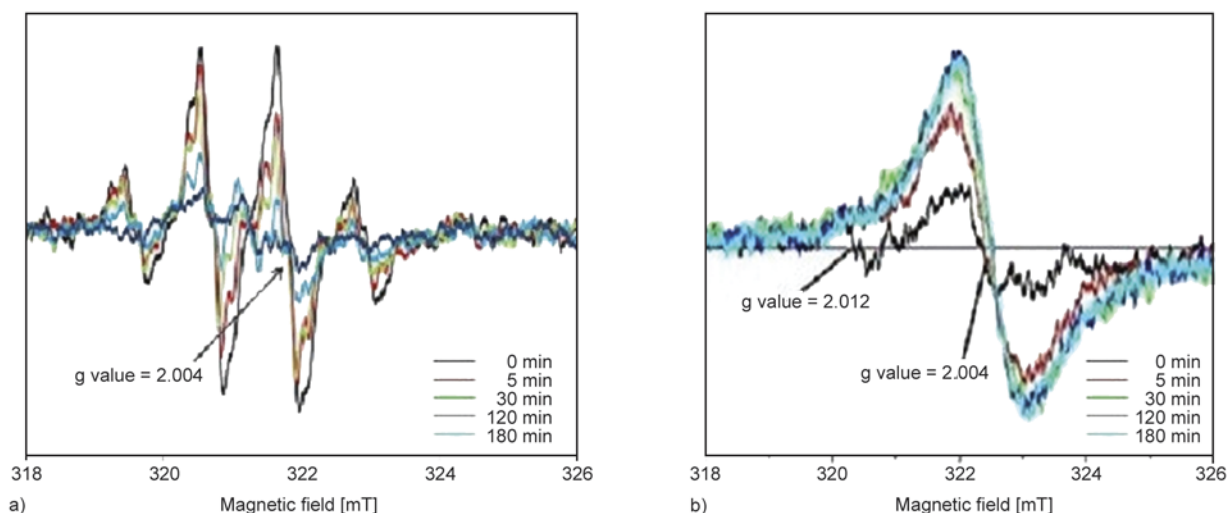
Figure 2. The first derivative of ESR spectra of DCP samples at different time during vulcanization at 150°C, a) IR samples and b) NR samples

chain giving rise to a cross-link and a new active free radical.

Taking into account this mechanism, the process is initiated by the thermal homolytic scission of the peroxide. Nevertheless, these radicals are not detected by the ESR experiments because they are very reactive radicals with a very short life time at the measured temperatures [27–30]. In addition, it is important to take into consideration the unavoidable uncertainties associated to the ESR data acquired during the first minute.

The intensity of the signal in the ESR spectrum depends on the stability of radicals (which determines the rate of decay) rather than the rate of their formation. For that reason, signals observed in the ESR spectra for IR samples vulcanized with DCP (Figure 2a) should be related to the formation of different polymer radicals. According to the intensity ratio and the g values around 2.0048 it is possible to assign them to allylic radicals. When the vulcanization time increases, the intensity of this signal increases because more allylic radicals are generated but some of them react with another polymer radical creating carbon-carbon crosslinks. After 120 minutes, the intensity of this signal diminishes because most of the allylic radicals have reacted. This statement agrees with the vulcanization curve (obtained with the rheometer) and determines the end of the vulcanization process.

It is important to remark that the ESR signal becomes broader with the vulcanization time because the formation of additional cross-links restricts the mobility of the radicals.

Previous work based on the study of free radicals in cross-linked EPDM rubbers attributed the peak with the g value around 2.012 to alkyl radicals generated in the initial steps of the peroxide vulcanization process. These alkyl radical intermediates are quite reactive and will readily react via abstraction of the allylic hydrogen in the diene monomer [11]. In the case of NR or IR rubber, the concentration of double bonds are higher than EPDM rubber and for that reason, alkyl radicals are less probable to be detected. Nevertheless, the NR ESR spectrum recorded at the earliest stage seems to show a signal with a g value close to 2.012 (Figure 2b).

In the case of NR sample vulcanized with DCP, the allyl radicals (assigned to the signal at $g = 2.004$) increases with the vulcanization time and become broader because the presence of non-rubber components which could hinder the mobility of the radicals. In addition these non-rubber components are able to reduce the ESR spectral resolution due to the incomplete averaging of anisotropies of magnetic parameters [11].

3.1.2. Sulfur cure systems

The sulfur vulcanization has been studied by using three different systems: conventional (CV with high sulfur concentration, A/S = 0.2), efficient (EV with high accelerator concentration, A/S = 12) and a sulfur donor (DPTT without addition of sulfur).

In spite of sulfur vulcanization mechanism is still a controversial issue, there is a widespread agreement about the basic steps of this process, which can be divided into three stages [2, 3]:

1. Accelerators chemistry where the active sulfurating agent is created.
2. Cross-link chemistry where the cross-links between rubber chains are formed.
3. Post-vulcanization chemistry where the shortening of sulfur bridges in addition to other degradation process takes place.

According to this mechanism, sulfur vulcanization is a complex process where radical route is considered as one of the main pathways which could explain the network structures reported for NR [2–5].

In this sense, the evaluation of model compounds with solid-state ^{13}C-NMR reveals that the main structures generated during sulfur vulcanization correspond to allylic attacks in both the secondary and primary carbons [31–37].

CV system

Figure 3 shows the first derivative of ESR spectra for IR-CV and NR-CV samples at different vulcanization times. This sulfur/accelerator system seems to form a more complex mixture of free radicals than the peroxide system according to the multiple peaks observed in Figure 3. This behavior could be associated on one hand to the number of ingredients (chemical species) in the recipe that are able to generate radicals and, on the other hand, the numerous reactions between them.

At the beginning of the vulcanization process (chemistry of accelerators) the concentration of free radicals increases very fast (see Figure 3) and it is possible to identify many different species (g = 1.974, 1.978, 2.004 and 2.024, respectively) which could be formed by the reaction of sulfur, zinc oxide,

stearic acid and accelerator system [2]. The active sulfurating agent formed during this step reacts with the rubber chain and it is able to graft the sulfur atoms in the macromolecule. This precursor moiety is converted into a cross-link by the direct reaction with another rubber molecule via a persulfenyl intermediate (RS$_y$•) [2]. For that reason, during the cross-linking reaction, most of the free radical species (evolved in the accelerator chemistry) disappear, but the total concentration of radicals in the system seems to be unaffected.

In order to understand this fact, it is mandatory to take into consideration that once the sulfur cross-links are formed, further desulfuration or degradation reactions take place (according to the vulcanization curves showed in Figure 1). In the desulfuration reactions, the removal of sulfur atoms changes the length distribution of sulfur bridges without any variation in the cross-link density [2]. In contrast, the degradation reactions lead to loss of cross-links and it results in complex structures like cyclic sulfides, main chain modifications and *cis/trans* isomerization [2]. Rubber samples vulcanized with conventional systems are characterized by the predominance of polysulfidic linkages in the network structure (C–S$_x$–C, where x identify the number of sulfur atoms in the sulfidic bridge), which are more sensitive to temperature than shorter di- or mono-sulfidic cross-links because of their lower dissociation energy (approximately 150 kJ/mol for polysulfidic bridges with four sulfur atoms) [2]. After the dissociation process, another active sulfur radical species are formed and they could react again to i) reform other sulfur cross-links with different lengths and/or
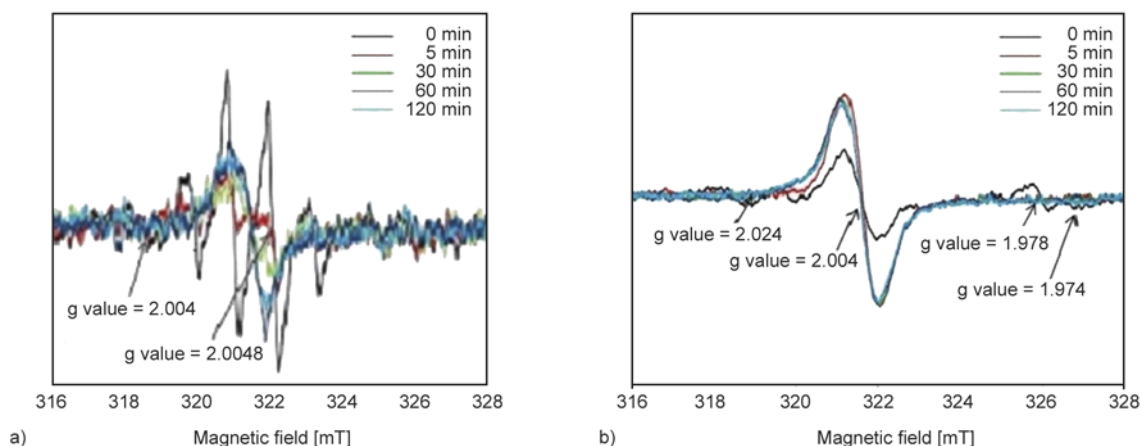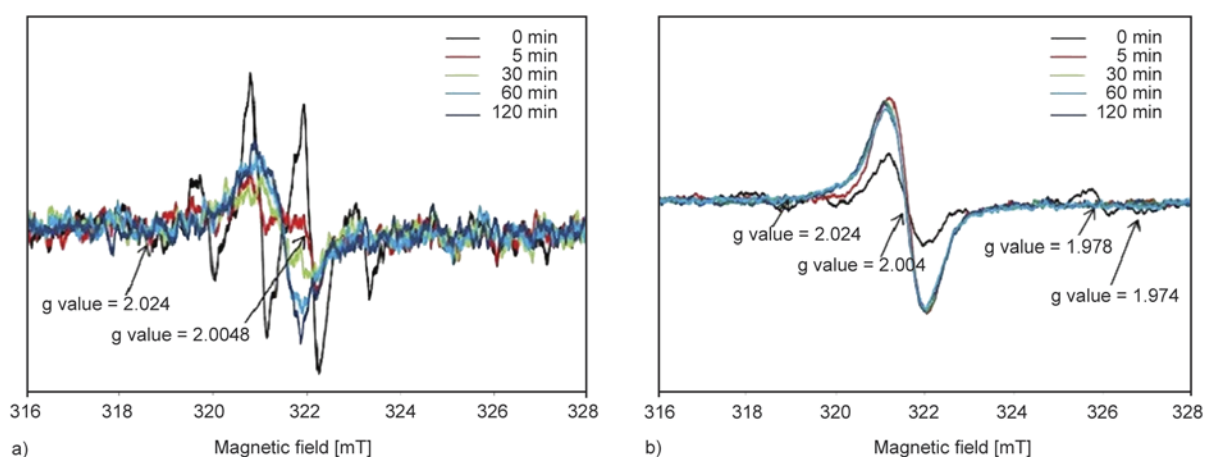

Figure 3. The first derivative of ESR spectra of CV samples at different time during vulcanization at 150°C, a) IR samples and b) NR samples

ii) form side products like RS_zH [2]. For that reason, the free radical species identified in the last steps of the vulcanization process correspond to carbon and sulfur radicals in rubber materials situated at $g = 2.004$ (these radicals are not distinguished because they have almost the same g value).

EV-cure system
Figure 4 shows the first derivative of ESR spectra for IR and NR samples vulcanized with an efficient vulcanization system at different reaction times. Spectra split into four peaks at short time, which can be attributed to radical species formed during the accelerator chemistry, as it was explained for the CV system.

The g-values in the ESR derivatives around 2.004 correspond to carbon or sulfur radicals generated in the course of the cross-linking reaction or during

the post vulcanization stage according to the statements widely explained for the CV systems.

DPTT system
Figure 5 shows the first derivatives of ESR spectra for samples vulcanized with the sulfur donor DPTT at different times. These spectra show the same peaks than the other sulfur-based systems (CV and EV) at the initial vulcanization time. However, in the samples vulcanized with DPTT, these radicals remain active throughout the vulcanization process.

It is important to remind that DPTT is capable to generate sulfidic cross-links without the addition of sulfur to the rubber compound. In the case of sulfur donor systems, the thermal scission of DPTT takes place via homolytic cleavage producing free radical species. Although other unsymmetrical cleavage is also possible, these reactions are less probable

Figure 4. The first derivative of ESR spectra of EV samples at different time during vulcanization at 150°C, a) IR samples and b) NR samples
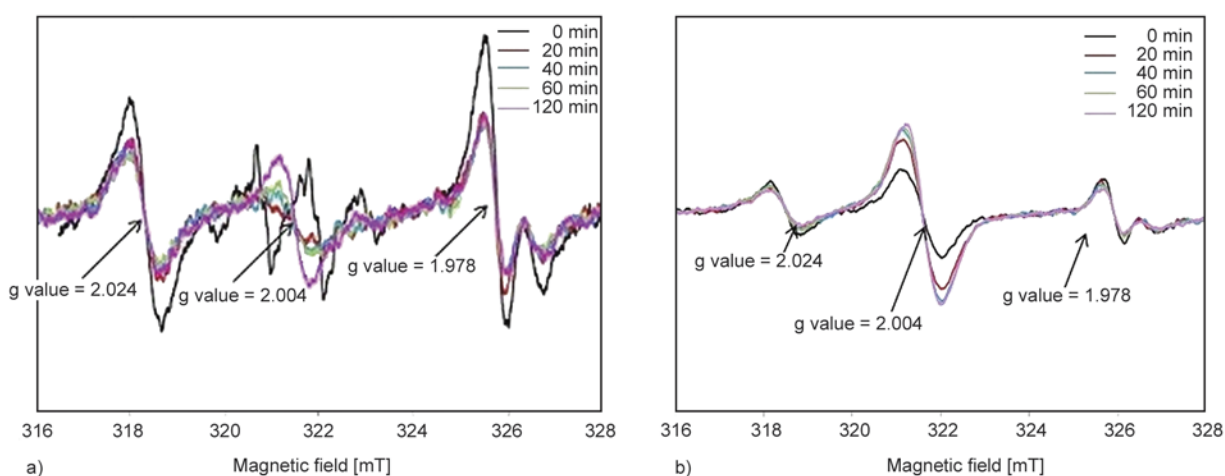

Figure 5. The first derivative of ESR spectra of DPTT samples at different time during vulcanization at 150°C, a) IR samples and b) NR samples

because require the breakdown of the more stable C–S bond. For this reason, only the two central sulfur atoms of DPTT molecule are able to create crosslinks [22, 23].

According this statement, the detection of ESR signals corresponding to the radical species formed during the chemistry of accelerators at larger vulcanization times identifies that their lifetime is enlarged in the DPTT system in comparison with the other sulfur based vulcanzation systems. This fact demonstrates that these radicals are more stable in the sulfur donor system, because there are not free sulfur molecules ready to react with them.

3.1.3. BSA system

Figure 6 shows the first derivatives of ESR spectra for samples vulcanized with BSA at different vulcanization times.

Besides sulfur and peroxide systems, there are some other less common vulcanization agents such as organic azides, which are capable to cross-link unsaturated rubber as NR, BR, SBR, EPDM and PDMS [15, 38, 39]. At temperatures near 100 °C, azides react by 1,3 dipolar cycle-addition mechanism giving rise to hetero-cycles of the 1,3 triazoline type. These derivates decompose releasing nitrogen and giving rise to aziridine and imine derivatives, the amount obtained from these products vary, depending on the type of olefin involved [15]. However, sulfonyl azides decompose to form a sulfonyl nitrene at elevated temperatures (above 155 °C). The nitrene exist in both the singlet and the triplet state. Both states can react with hydrocarbons but they do it in different ways. The reaction involving the singlet nitrene

is an insertion at the C–H bond giving a secondary sulfonamide, while the triplet nitrene reacts by abstraction of a proton from the hydrocarbon resulting in the formation of a macroradical and this reaction can follow by a recombination of two macroradicals to form a cross-link [40].

The ESR measurements of BSA system were executed at 105 °C in order to promote the cross-linking reaction in absence of radicals, according to the mechanism describe before. At this temperature, the cross-linking mechanism of azide molecules is controlled through the formation of the heterocyclic 1,2,3, triazoline intermediate, which is unstable at higher temperatures. Nevertheless, BSA system is able to create nitrogenous radical which seems to have a similar behavior than alkoxy radicals obtained during the vulcanization with organic peroxides, as it is shown in Figure 6.

3.2. Comparison of radical amounts produced by different vulcanization system

The concentration of radical species produced by the different vulcanization agents are compared in Figure 7. The first important conclusion extracted from this study is that all the vulcanization systems, e.g. organic peroxide, sulfur/accelerator, sulfur donor system and azide molecules, produce free radical species during the vulcanization process of NR and IR matrices. The appearance of ESR-detectable species requires the accumulation of high concentration of radicals. Usually carbon-centered radicals are extremely reactive and consequently not detectable by ESR at the vulcanization temperature. However, the formation of cross-links reduces the
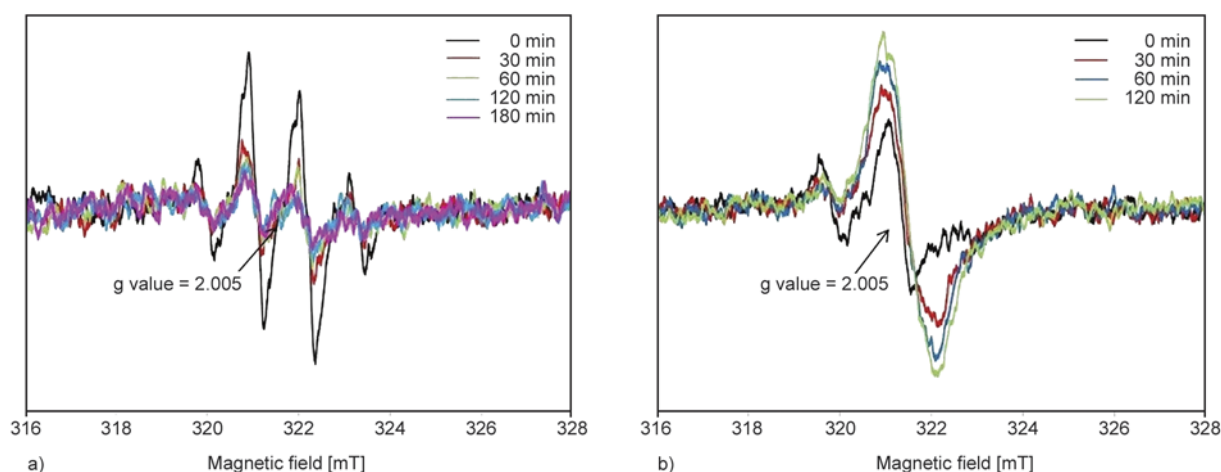

Figure 6. The first derivative of ESR spectra of BSA samples at different time during vulcanization at 105°C, a) IR samples and b) NR samples
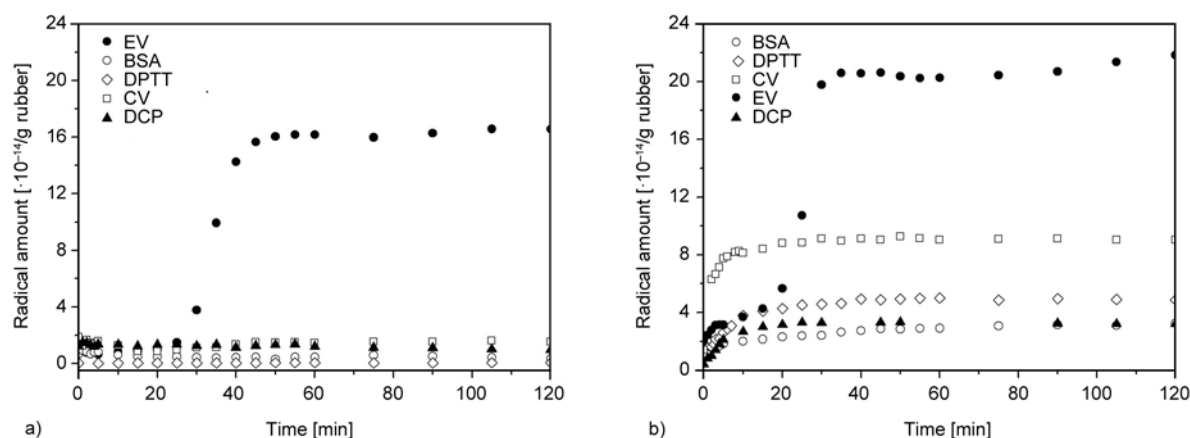
Figure 7. Radical concentration produced by different vulcanization agent a) in IR rubber and b) in NR rubber

mobility and the accessible space to rubber segments, limiting the reaction of radicals and enlarging their lifetime.

In a previous work, the peroxide vulcanization of different ethylene-propylene-diene rubbers were investigated by using ESR technique, showing the increase of ESR intensities with the vulcanization time until it reach a maximum, followed by a long decay of this intensity at larger times because of the consumption of the formed radicals [11].

Opposite to this behavior, NR and IR matrices show an increasing concentration of radical species with the vulcanization time until a plateau is reached. The concentration of radicals remain almost constant over the optimum vulcanization time (as measured by rheometric curves), indicating that the radicals generated during vulcanization process have a long lifetime. The enhanced stability of radicals in NR matrix is caused by the high concentration of double bonds in the polymer backbone in comparison with the EPDM matrices [11]. In addition, the more restricted mobility of polymer radicals with the vulcanization time (because of the development of cross-linking reaction) not only enlarge the lifetime of radicals, but also it worsens the ESR spectral resolution due to the incomplete averaging of anisotropies of magnetic parameters [11].

In this sense, the ESR spectra for NR samples always show worst resolution and higher radical concentration than the IR samples, independently of the vulcanization system. Differences between rubber matrices are explained neither by the differences in the chemical structure of polymer radicals nor by the effect of cross-links in the segmental mobility of the polymer backbone (both NR and IR have almost the same cross-link density at the optimum vulcaniza-

tion time according the equilibrium swelling experiments). These results seem to indicate the importance of non-rubber components in NR during the creation of different radical species during the vulcanization process, independently of the used cure system. Additionally, thermal degradation of these non-rubber components at the vulcanization temperature would be one of the main factors in the formation of radicals, although they have not a clear influence on the creation of additional cross-links.

The EV system always shows the highest concentration of free radicals (almost double) during the vulcanization. In order to understand this result, the two closer sulfur/accelerator systems, e.g. EV and CV, have been compared. In first term, and taking into account the previous statements, the higher concentration of free radicals during the vulcanization with EV system should be mainly ascribed to the highest amount of accelerant (CBS) in the recipe. According to previous studies, the molecule of CBS produces radicals at 150 °C [14, 21].

The cross-link density is around 30% higher for samples vulcanized with the EV system. This fact could enhance the lifetime of radical species, but it is not enough to justify the difference in the concentration of radicals. In second term, the thermal stability of mono- and di-sulfidic linkages – which are the main type of cross-links in the EV systems – is higher in comparison to the poly-sulfidic bridges that are mainly formed during the vulcanization with the CV system. The shorter sulfidic cross-links are characterized by higher dissociation energies (289 kJ/mol for di-sulfidic bonds [2]). This difference in bond association energies is related to the formation of monosulfidic radicals RS$^{\bullet}$, which are not stabilized by neighboring sulfur atoms [2]. This fact

should reduce the radical species for EV systems during the post-vulcanization stage.

3.3. Evolution of radical amounts under the tensile deformation

Spectra for all samples were made at different strain. All resonance lines show a broad absorption with the same *g* value of 2.004, which is assigned to carbon and sulfur radicals as it was described in the previous sections. Since the sample volume in the ESR cavity decreases with strain, the raw spectra were corrected by the volume change assuming that Poisson's ratio of the samples was kept as 0.5. The experiments were rather difficult because the thin stripe samples were elongated in a small ESR cavity, samples were easily torn during elongation. Only four samples were succeeded to get the data. As an example, radical concentrations for sulfur accelerated vulcanization at different strains are showed in Figure 8.

During deformation, the rupture of network points and polymer chains may occur accompanying the formation of radicals. Network densities for all the studied samples are similar (see Table 2), consequently the differences in the creation of radicals during deformation should be directly related to the different nature of network points formed during the vulcanization process.

The radical concentration remains constant with strain in the vulcanized IR samples as it is showed in Figure 8a. Only the sample vulcanized with the EV system shows a slight increase in the radical concentration at low strain. Opposite to this behavior, the radical concentration increases with strain for the NR samples, independently of the vulcanization system. In addition, it is important to point out the cer-

tain amounts of radicals are detectable by ESR in the un-stretched state (strain 0) for samples vulcanized with EV system, demonstrating their stability and extremely long lifetime.

4. Conclusions

ESR detectable species requires the accumulation of high concentration of radicals. For that reason, the extremely reactive carbon-centered radicals are not detectable by ESR at the vulcanization temperature. However, the formation of cross-links reduces the mobility and accessible conformations of rubber segments, limiting the reaction of radical species and enlarging their lifetime. In this sense, the first important conclusion is that all the studied vulcanization systems, e.g. organic peroxide, sulfur/accelerator, sulfur donor system and azide molecules, produce free radical species during the vulcanization process of NR and IR matrices.

In the case of peroxide and BSA systems only the radical with the *g* value around 2.004 is detected by ESR. This radical is attributed to the allylic radical in the polymer backbone generated during the cross-linking reaction. Sulfur systems seem to form more complex mixture of free radicals according to the higher number of peaks detected by ESR. This behavior could be associated on one hand, to the high number of ingredients inside the rubber matrix that are able to generate radicals and on the other hand, the numerous reactions between them. At the beginning of the vulcanization process, the concentration of free radicals increases very fast and it is possible to identify many different kinds of radicals species (*g* = 1.974, 1.978, 2.004 and 2.024) which could be formed by the reaction of sulfur, zinc oxide, stearic acid and the accelerator system. These radicals dis-
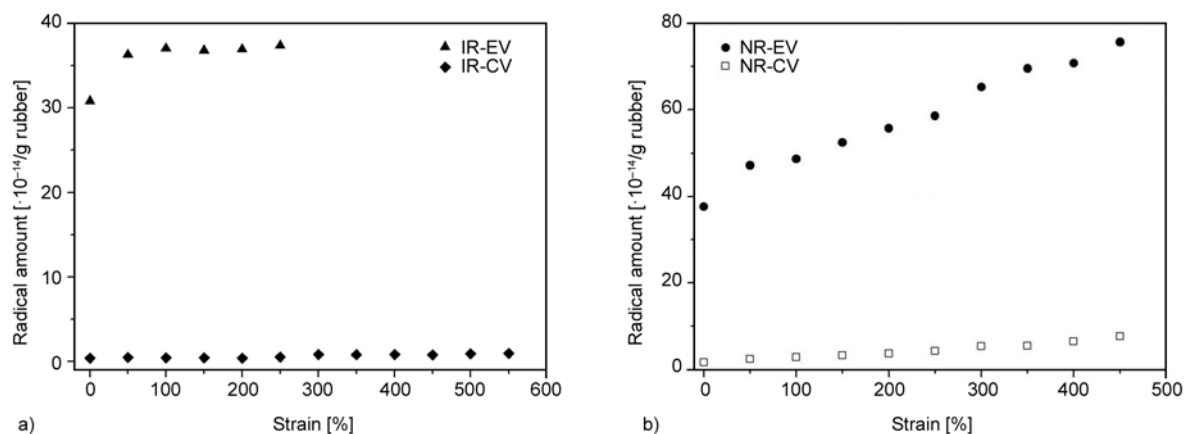

Figure 8. Evolution of radical amount vs. strain in a) IR E and IR-CV systems, b) in NR-E and NR-CV systems

appear during the cross-linking reaction in the case of sulfur/accelerator systems. However, these radicals remain active for longer times in those samples vulcanized with sulfur donor system. The higher lifetime of these radicals could be attributed to their enhanced stability as a consequence of the lack of reactive sulfur molecules in the system.

The ESR signals for NR samples are always broader than in the case of IR samples due to the presence of non-rubber components which could hinder the mobility of radicals and additionally they provoke the incomplete averaging of anisotropies of magnetic parameters.

In addition, the concentration of radicals remains almost constant over the optimum vulcanization time measured by the rheometer, indicating that radicals generated during the vulcanization process have a long lifetime. EV vulcanization system shows the highest concentration of radical species, because of large amount of the accelerator (CBS). During deformation, the NR samples always show higher concentration of radicals than the IR counterparts. Additionally, the concentration of radical species increases with deformation for NR compounds.

Acknowledgements

References

[1] Coleman M. M., Shelton J. R., Koenig J. L.: Sulfur vulcanization of hydrocarbon diene elastomers. Industrial and Engineering Chemistry Product Research and Development, **13**, 154–166 (1974).
DOI: 10.1021/i360051a002

[2] Ghosh P., Katare S., Patkar P., Caruthers J. M., Venkatasubramanian V.: Sulfur vulcanization of natural rubber for benzothiazole accelerated formulations: From reaction mechanisms to a rational kinetic model. Rubber Chemistry and Technology, **76**, 592–693 (2003).
DOI: 10.5254/1.3547762

[3] Heideman G., Datta R. N., Noordermeer J. W. M., van Baarle B.: Activators in accelerated sulfur vulcanization. Rubber Chemistry and Technology, **77**, 512–541 (2004).
DOI: 10.5254/1.3547834

[4] Krejsa M. R., Koenig J. L.: A review of sulfur cross-linking fundamentals for accelerated and unaccelerated vulcanization. Rubber Chemistry and Technology, **66**, 376–410 (1993).
DOI: 10.5254/1.3538317

[5] Manik S. P., Barnerjee S.: Sulfenamide accelerated sulfur vulcanization of natural rubber in presence and absence of dicumyl peroxide. Rubber Chemistry and Technology, **43**, 1311–1326 (1970).
DOI: 10.5254/1.3547331

[6] Valentín J. L., Posadas P., Fernández-Torres A., Malmierca M. A., González L., Chassé W., Saalwächter K.: Inhomogeneities and chain dynamics in diene rubbers vulcanized with different cure systems. Macromolecules, **43**, 4210–4222 (2010).
DOI: 10.1021/ma1003437

[7] Chapman A. V., Porter M.: Natural rubber science and technology. Oxfor Science Publications, New York (1988).

[8] Dluzneski P. R.: Peroxide vulcanization of elastomers. Rubber Chemistry and Technology, **74**, 451–492 (2001).
DOI: 10.5254/1.3547647

[9] Camara S., Gilbert B. C., Meier R. J., van Duin M., Whitwood A. C.: EPR studies of peroxide decomposition, radical formation and reactions relevant to cross-linking and grafting in polyolefins. Polymer, **47**, 4683–4693 (2006).
DOI: 10.1016/j.polymer.2006.04.015

[10] Liu J., Yu W., Zhao C., Zhou C.: EPR/rheometric studies on radical kinetics in melt polyolefin elastomer initiated by dicumyl peroxides. Polymer, **48**, 2882–2891 (2007).
DOI: 10.1016/j.polymer.2007.03.053

[11] Zachary M., Camara S., Whitwood A. C., Gilbert B. C., van Duin M., Meier R. J., Chechik V.: EPR study of persistent free radicals in cross-linked EPDM rubbers. European Polymer Journal, **44**, 2099–2107 (2008).
DOI: 10.1016/j.eurpolymj.2008.04.008

[12] Yamazaki T., Seguchi T.: Electron spin resonance study on chemical crosslinking reaction mechanisms of polyethylene using a chemical agent. V. Comparison with polypropylene and ethylene-propylene copolymer. Journal of Polymer Science Part A: Polymer Chemistry, **38**, 3383–3389 (2000).
DOI: 10.1002/1099-0518(20000915)38:18<3383::AID-POLA170>3.0.CO;2-M

[13] Dondi D., Buttafava A., Zeffiro A., Palamini C., Lostritto A., Giannini L., Faucitano A.: The mechanisms of the sulfur-only and catalytic vulcanization of polybutadiene: An EPR and DFT study. European Polymer Journal, **62**, 222–235 (2015).
DOI: 10.1016/j.eurpolymj.2014.11.012

[14] Toki S., Takagi R., Ito M., Hsiao H. S.: Rupture, orientation and strain-induced crystallization of polymer chain and network in vulcanized polyisoprene during uniaxial deformation by *in-situ* electron spin resonance (ESR) and synchrotron X-ray analysis. Polymer, **52**, 2453–2459 (2011).
DOI: 10.1016/j.polymer.2011.03.037

[15] de Benito G. J. L., Ibarra R. L. M., González H. L.: The use of benzene 1,3-sulphonyl azide as an elastomer cross-linking agent. I, Dienic elastomers. Kautschuk und Gummi, Kunststoffe, **43**, 146–149 (1990).

[16] Valentín J. L., Carretero-Gonzalez J., Mora-Barrantes I., Chassé W., Saalwächter K.: Uncertainties in the determination of cross-link density by equilibrium swelling experiments in natural rubber. Macromolecules, **41**, 4717–4729 (2008).
DOI: 10.1021/ma8005087

[17] Flory P., Rehner J.: Statistical mechanics of cross-linked polymer networks II. Swelling. Journal of Chemical Physics, **11**, 521–526 (1943).
DOI: 10.1063/1.1723792

[18] Ito M., Isago H., Suzuki N.: ESR study of silica-filled SBR with different rubber/filler interactions. Journal of Applied Polymer Science, **108**, 1385–1392 (2008).
DOI: 10.1002/app.27843

[19] Ito M., Takizawa A.: Difference in the stability of network between natural rubber and polyisoprene vulcanizates. Kautschuk und Gummi Kunststoffe, **65**, 24–27 (2012).

[20] Suzuki N., Ito M., Yatsuyanagi F.: Effects of rubber/filler interactions on deformation behavior of silica filled SBR systems. Polymer, **46**, 193–201 (2005).
DOI: 10.1016/j.polymer.2004.10.066

[21] Funatsu J., Takagi R., Ito M.: ESR study of vulcanizates under the deformed state. Journal of Applied Polymer Science, **113**, 2791–2795 (2009).
DOI: 10.1002/app.30340

[22] González L., Rodríguez A., Valentín J. L., Marcos-Fernández, A., Posadas P.: Conventional and efficient crosslinking of natural rubber: Effect of heterogeneities on the physical properties. Kautschuk und Gummi Kunststoffe, **58**, 638–643 (2005).

[23] Posadas P., Fernández-Torres A., Valentín J. L., Rodríguez A., González L.: Effect of the temperature on the kinetic of natural rubber vulcanization with the sulfur donor agent dipentamethylene thiuram tetrasulphide. Journal of Applied Polymer Science, **115**, 692–701 (2010).
DOI: 10.1002/app.30828

[24] González L., Rodríguez A., Marcos-Fernández A., Chamorro C.: New aspects of the crosslinking reaction of natural rubber with dicumil peroxide filler effect. Kautschuk und Gummi Kunststoffe, **47**, 715–721 (1994).

[25] González L., Rodríguez A., Marcos A., Chamorro C.: Crosslink reaction mechanisms of diene rubber with dicumyl peroxide. Rubber Chemistry and Technology, **69**, 203–214 (1996).
DOI: 10.5254/1.3538365

[26] Valentín J. L. Fernández-Torres A., Posadas P., Marcos-Fernández A., Rodríguez A., González L.: Measurements of freezing-point depression to evaluate rubber network structure. Crosslinking of natural rubber with dicumyl peroxide. Journal of Polymer Science Part B: Polymer Physics, **45**, 544–556 (2007).
DOI: 10.1002/polb.21060

[27] Gilbert B. C., Dobbs A. J.: Organic peroxide. Wiley, New York (1972).

[28] Shida T.: Electron spin resonance and optical studies of tert-butyl peroxide ions produced by γ-irradiation. Journal of Physical Chemistry, **72**, 723–727 (1968).
DOI: 10.1021/j100848a055

[29] Zhou W., Zhu S.: ESR study of peroxide-induced crosslinking of high density polyethylene. Macromolecules, **31**, 4335–4341 (1998).
DOI: 10.1021/ma970973s

[30] Zwolenik J. J.: Photolytic generation and kinetic electron spin resonance spectrometry of cumylperoxy radicals. Journal of Physical Chemistry, **71**, 2464–2469 (1967).
DOI: 10.1021/j100867a012

[31] Andreis M., Liu J., Koenig J. L.: Solid-state carbon-13 NMR studies of vulcanized elastomers. V. Observation of new structures in sulfur-vulcanized natural rubber. Journal of Polymer Science Part B: Polymer Physics, **27**, 1389–1404 (1989).
DOI: 10.1002/polb.1989.090270702

[32] Clough R. S., Koenig J. L.: Solid-state carbon-13 NMR studies of vulcanized elastomers. VII. Sulfur-vulcanized cis-1,4 polybutadiene at 75.5 MHz. Rubber Chemistry and Technology, **62**, 908–927 (1989).
DOI: 10.5254/1.3536283

[33] Komoroski R. A., Shockcor J. P., Gregg E. C., Savoca J. L.: Characterization of elastomers and rubber chemicals by modern NMR techniques. Rubber Chemistry and Technology, **59**, 328–346 (1986).
DOI: 10.5254/1.3538204

[34] Krejsa M. R., Koenig J. L.: Solid-state C-13 NMR studies of vulcanized elastomers X. *N-t*-butyl-2-benzothiazole sulfenamide accelerated sulfur vulcanization of *cis*-polyisoprene at 75.5 MHz. Rubber Chemistry and Technology, **65**, 427–443 (1992).
DOI: 10.5254/1.3538622

[35] Skinner T. D.: The CBS-accelerated sulfuration of natural rubber and cis-1,4-polybutadiene. Rubber Chemistry and Technology, **45**, 182–192 (1972).
DOI: 10.5254/1.3544698

[36] Zaper A. M., Koenig J. L.: Solid state carbon-13 NMR studies of vulcanized elastomers. II, Sulfur vulcanization of natural rubber. Rubber Chemistry and Technology, **60**, 252–277 (1987).
DOI: 10.5254/1.3536129

[37] Zaper A. M., Koenig J. L.: Solid state carbon-13 NMR studies of vulcanized elastomers. III, Accelerated sulfur vulcanization of natural rubber. Rubber Chemistry and Technology, **60**, 278–297 (1987).
DOI: 10.5254/1.3536130

[38] Damiron D., Okhay N., Al Akhrass S., Cassagnau P., Drockenmuller E.: Crosslinked PDMS elastomers and coatings from the thermal curing of vinyl-functionalized PDMS and a diazide aliphatic crosslinker. Journal of Polymer Science Part A: Polymer Chemistry, **50**, 98–107 (2012).
DOI: 10.1002/pola.24991

[39] De Benito G. J. L., Ibarra R. L. M., González H. L.: The use of 1,3 bis benzene sulphonyl azide as an elastomer crosslinking agent. II. Saturated elastomers. Kautschuk und Gummi Kunststoffe, **43**, 697–700 (1990).

[40] Jørgensen J. K., Ommundsen E., Stori A., Redford K.: Synthesis, characterisation and decomposition of 1,3-benzene disulfonyl azide; A cross-linking agent for polyolefins. Polymer, **46**, 12073–12080 (2005).
DOI: 10.1016/j.polymer.2005.10.077

Numerical simulations of residual stress and inhomogeneous conductivity effects in CNT-filled resins cured by electric field

R. Matsuzaki[*], S. Hatori*

Department of Mechanical Engineering, Tokyo University of Science, 2641 Yamazaki, Noda, Chiba 278-8510, Japan

Abstract. To achieve uniform curing of resin, internal heating with the addition of carbon nanotubes (CNTs) has attracted considerable attention. Numerical simulations of the residual stress in CNT-filled resins cured by an electric field were carried out in the present study, taking into account the CNT dispersion within the resins. The simulations were based on an unsteady-heat-transfer equation and the cure reaction; the residual stress due to the thermal expansion and cure shrinkage was calculated using a finite element method. In addition, microscope images of actual CNT-filled resins were used for modeling the inhomogeneous electrical conductivity due to CNT aggregates. The simulation results show that, compared to external heating, Joule heating, or resistive heating, in which a conductive material itself generates heat from the passage of an electric current, enables more uniform curing and generally suppresses the residual stress. However, high local residual stress was observed around the high-electrical conductivity region in the model with inhomogeneous electrical conductivity. The present results thus highlight the need to take into account the inhomogeneity of CNT-filled resins for accurate evaluation of the residual stress.

Keywords: polymer composites, nanocomposites, mechanical properties, modeling and simulation, carbon nanotubes

1. Introduction

External heating, such as that in the autoclave curing of thermosetting composites, may induce inhomogeneities in the temperature distribution or in the progression of curing because the temperature of the material's surface is raised by convective heat transfer from the atmosphere. The inhomogeneity of the curing process is especially evident in complex or thick composite structures, where residual stress and strain are induced, and the inhomogeneity may eventually initiate defects such as matrix cracks and deterioration of properties [1–3]. In order to achieve more uniform curing of the thermosetting resin, internal heating via an electric field has attracted considerable attention because it allows the material to be heated from the inside. Compared with conventional external heating, it has been reported that inter-nal heating leads to improved mechanical properties [4–7], adhesive bonding [8], and heating efficiency, as well as shorter curing cycles [9–11].

It is possible to increase the amount of heat generated by internal heating, such as microwave or Joule heating, by adding conductive fillers like carbon nanotubes (CNTs) [12–14] or carbon black [15] to the uncured thermosetting resin. At the same time, the inclusion of nanofillers leads to superior mechanical, conductive [16–18], and dielectric [19] properties compared with neat resins [20–23]. However, conventional microwave-heating equipment is very expensive, especially for curing large-scale structures, thus offsetting the advantages of improved energy efficiency. In addition, because the composite structures need to be enclosed within the conventional microwave-heating equipment, the struc-

---

[*]Corresponding author, e-mail: rmatsuza@rs.tus.ac.jp

tures must be smaller than the equipment's heating chamber. The expensive production costs and the limit on the size of molded composites represent serious problems for the application of the composites in consumer products such as automobiles. This highlights the need to develop new methods for uniform heating and curing that do not require expensive tools and accessories.

To meet this demand, we had developed in earlier studies a microwave curing method using thin-film-type electrode arrays and CNTs added to the epoxy resin, as shown in Figure 1a [24–27]. The method yields a heating efficiency as high as 70% and a drastic increase in the amount of heat generated when the added CNT content reaches the percolation threshold [28]. However, in microwave-based curing processes, because an inhomogeneous electrical conductivity (such as in the presence of CNT aggregates) may induce localized heat generation (Figure 1b) [28–31], it is clear that the distribution of CNTs must be taken into account for an accurate evaluation of the residual stress. Whereas numerical simulations can be used to assess the effect of an inhomogeneous CNT distribution on residual stress, simulations of this kind have yet to be conducted.

Therefore, in the present study, we performed numerical simulations to investigate how an inhomogeneous CNT distribution affects CNT-filled thermosetting resins cured via an electric field. The inhomogeneous electrical conductivity was modeled using the microscope images of actual CNT aggregates, and the simulations were based on the analysis of unsteady heat transfer, including Joule heating and heat generated by the curing reaction. The residual stress due to the thermal expansion and cure shrinkage was calculated using the finite element method based on linear viscoelastic models. We compared the residual stress induced by internal (electric field) and external (heat flux) heating. Finally, we compared homogeneous and inhomogeneous conductivity models to investigate the effect of the conductivity distribution of a CNT-filled resin on the residual stress.

2. Materials and methods
2.1. Inhomogeneous conductivity and heat transfer models
2.1.1. Inhomogeneous conductivity model of CNT-filled resin
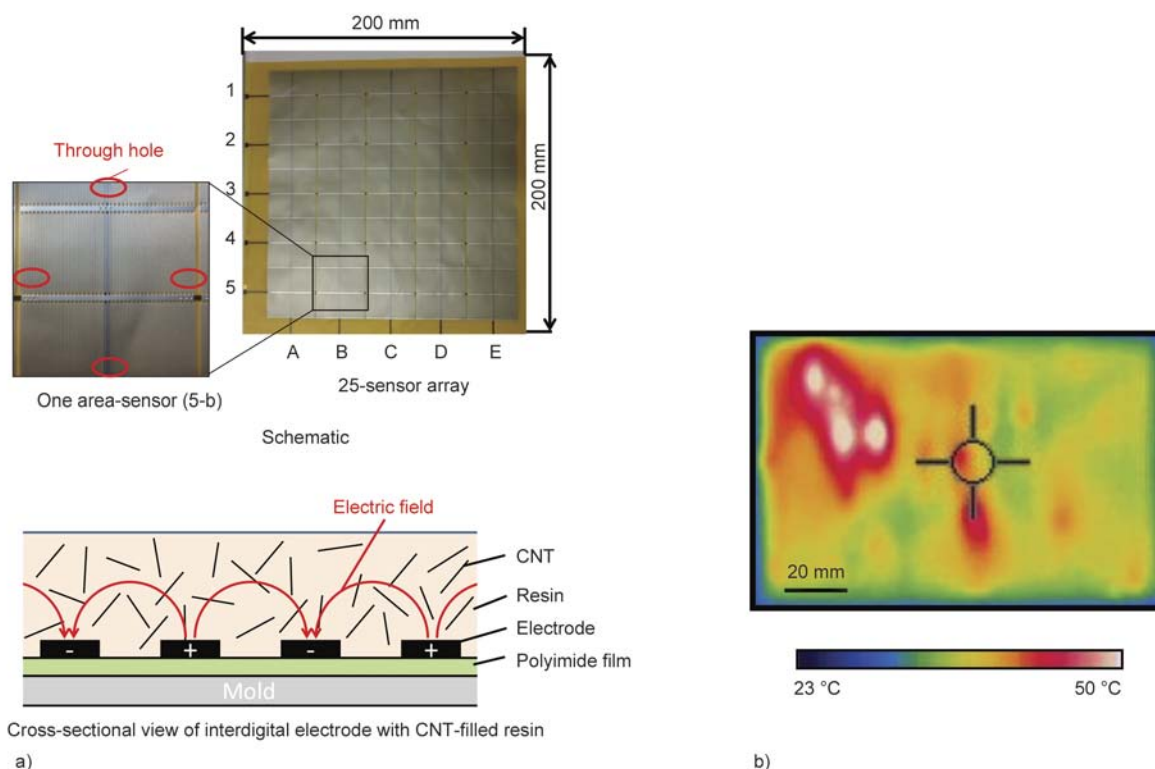Because it is difficult to attain uniform dispersion without the formation of CNT aggregates, the CNT

Figure 1. Microwave curing using thin-film-type electrode arrays and CNTs added to the epoxy resin. (a) Schematic of multifunctional interdigital electrode array (MIEA) film and cross-sectional view of interdigital electrode with CNT-filled resin. (b) Localized heat generation inside an interdigital electrode with CNT-filled resin.

distribution should be taken into account when modeling the electrical conductivity. In order to model the electrical conductivity of the CNT-filled resin, we used optical microscope images of 0.05–1.0 wt% CNT-filled resins (Figure 2a). For preparation of CNT-filled resin, the CNTs (VGCF-X, Showa Denko, 3 μm in length, and 15 nm in diameter) were dried in an oven at 100 °C for 1 h, after which they were mixed with unsaturated polyester (PC-184-C, Sundhoma) in a planetary kneader machine (NBK-1, Nissei) at 1700 rpm for 3 min. The sample mixtures were thereafter treated in an ultrasonic bath sonicator (US-2K, AS ONE) for 2 h, with further mixing of 3 min in the kneader machine every 30 min. The image of each CNT–filled resin was binarized (i.e., converted into a black and white image), and the CNT area ratio VCNT was calculated by assuming that the CNTs are displayed as dark areas in the images. By using the electrical conductivity measured for each CNT weight percentage shown in Figure 3a [32], we obtained the relationship between the microscopic electrical conductivity and CNT area ratio V_{CNT}, shown in Figure 3b. In order to model the electrical conductivity distribution of a macroscopic region, the corresponding CNT distribution image was obtained and binarized; examples of the

model and binarized image of the 0.2 wt% CNT-filled resin are shown in Figure 2b and 2c. The binarized image was discretized into small regions, whose corresponding V_{CNT} was calculated (Figure 2d); the electrical conductivity of each microscopic region was then allocated (Figure 2e) based on the relationship between V_{CNT} and the electrical conductivity revealed in Figure 3b. The size of the microscopic region was determined to match the mesh size of the numerical analysis, which is 0.1 mm×0.1 mm in the present study. It should be noted that the depiction in Figure 2d was generated by interpolating the 0.1 mm×0.1 mm mesh value in Figure 2c. Figure 2e was also generated by interpolating the measured values in Figure 3b. The validity of this approach was confirmed by the agreement between the macroscopic electrical conductivity obtained from the inhomogeneous conductivity model and the conductivity measured for the resin with the same added CNT content.

2.1.2. Unsteady-heat-transfer equation

The unsteady-heat-transfer equation for the heat generated by the resin cure reaction and by Joule heating under an electric field is given by Equation (1):
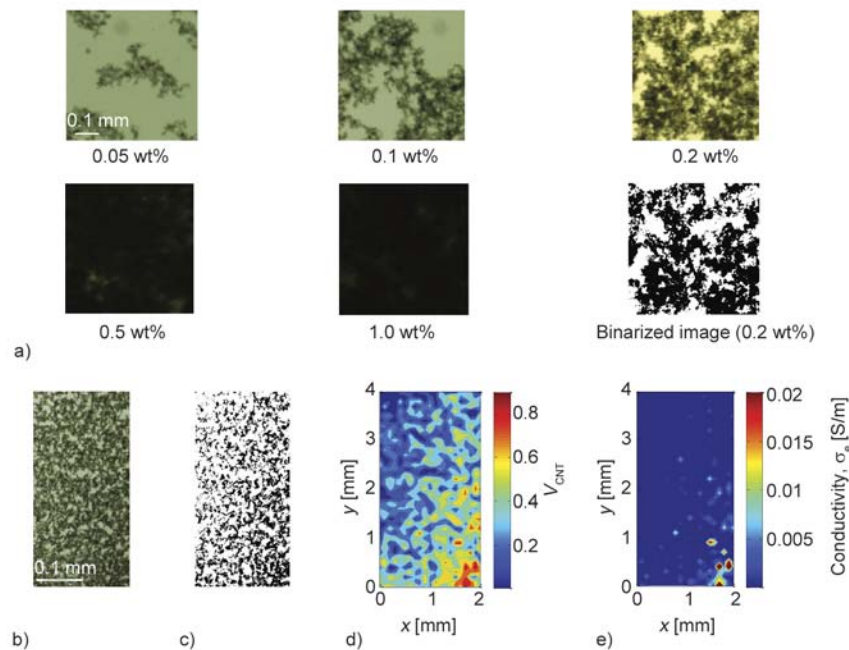

Figure 2. Modeling of inhomogeneous electrical conductivity of CNT-filled resins. (a) Microscope image of CNT-filled resins with various CNT concentrations [wt%] and binarized image of 0.2 wt% CNT-filled resin. (b) Analytical model of 0.2 wt% CNT-filled resin. (c) Binarized image of (b). (d) Distribution of CNT area ratio (VCNT). (e) Distribution of electrical conductivity (σ_e).
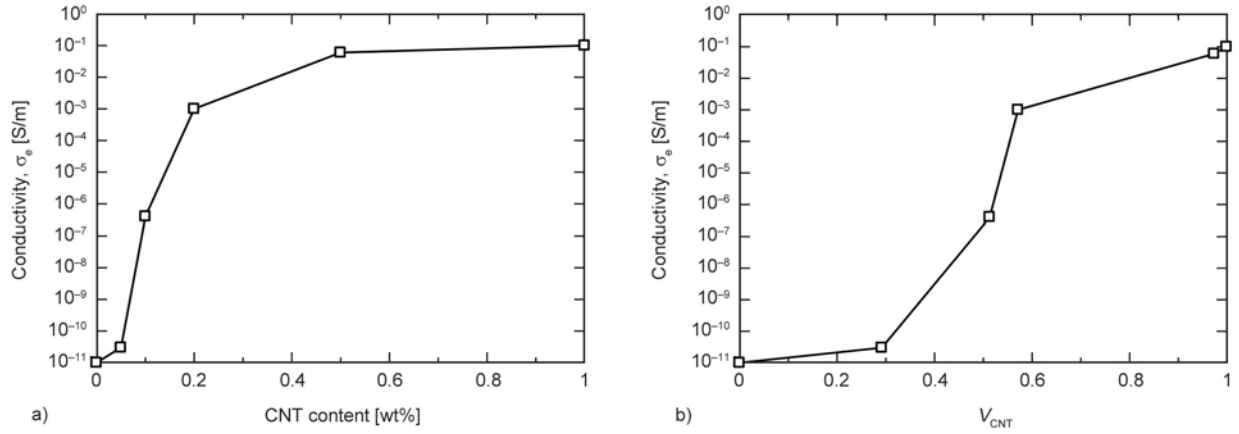
Figure 3. CNT content, electric conductivity σ_e, and CNT area ratio V_{CNT} of CNT-filled resins. (a) Relationship between electrical conductivity and CNT content [32]. (b) Relationship between electrical conductivity and V_{CNT}.

$$\rho c \frac{\partial T}{\partial t} = \frac{\partial}{\partial x}\left(k_{xx}\frac{\partial T}{\partial x}\right) + \frac{\partial}{\partial y}\left(k_{yy}\frac{\partial T}{\partial y}\right) + \dot{Q}_j + \rho\dot{Q}_c \quad (1)$$

where T is the temperature, ρ is the density, c is the specific heat, $\dot{Q}_j$ is the heat generation rate per unit volume due to Joule heating, and $\dot{Q}_c$ is the heat generation rate per unit weight due to the curing reaction; k_{xx} and k_{yy} are the coefficients of thermal conductivity in the x and y direction, respectively. The heat generation rate due to Joule heating $\dot{Q}_j$ under an electric field **E** is given by Equation (2):

$$\dot{Q}_j = \mathbf{J}\cdot\mathbf{E} = (\sigma_e\mathbf{E})\cdot\mathbf{E} = \sigma_e\|\nabla V\| \quad (2)$$

where **J** is the electric current density, σ_e is the electrical conductivity, and V is the applied voltage. The heat generation rate due to the cure reaction $\dot{Q}_c$ is given by the following Equation (3), using a cure reaction model for unsaturated polyester resins [33]:

$$\dot{Q}_c = H_r\frac{d\alpha}{dt} = H_r k_1\exp\left(-\frac{E_a}{RT}\right)(\alpha)^m(1-\alpha)^n \quad (3)$$

where α is the degree of cure, k_1 is the reaction rate constant, E_a is the activation energy, R is the gas constant, m and n are reaction orders, and H_r is the total heat of reaction.

2.2. Analysis of residual stress and strain
2.2.1. Strain induced by thermal expansion and cure shrinkage
The rate of change in volumetric strain of the resin induced by thermal expansion and cure shrinkage is given by Equation (4) [34]:

$$\left(\frac{1}{V_0}\frac{dV}{dt}\right) = \left(\frac{1}{V_0}\frac{dV}{dt}\right)_{thermal} - \left(\frac{1}{V_0}\frac{dV}{dt}\right)_{polymerization} \quad (4)$$

where V_0 is the initial volume, the first term of the right-hand side represents the contribution of bulk thermal expansion and contraction, and the second term is the volumetric strain change due to the cure shrinkage. These two terms are given by Equations (5) and (6):

$$\left(\frac{1}{V_0}\frac{dV}{dt}\right)_{thermal} = \{\beta_{gel}(T)(1-\alpha) + \beta_{cured}(T)\alpha\}\frac{dT}{dt} \quad (5)$$

$$\left(\frac{1}{V_0}\frac{dV}{dt}\right)_{polymerization} = \lambda_{chem}\frac{d\alpha}{dt} \quad (6)$$

where β_{gel} and β_{cured} are the coefficients of thermal expansion of the uncured and fully cured resin, respectively, and λ_{chem} is the total polymerization shrinkage. The coefficients β_{gel} and β_{cured} are functions of the temperature T and are given by Equation (7):

$$\beta_{gel} = e_1 T + f_1; \quad \beta_{cured} = e_2 T + f_2 \quad (7)$$

where e_1, f_1, e_2, and f_2 are material-dependent parameters.

2.2.2. Viscoelastic model taking into account temperature and degree of cure
To model the material behavior when changing from a liquid to a solid state during the curing process, the mechanical behavior of the polymer resins is

expressed by the following linear viscoelastic constitutive Equation (8):

$$\sigma(t) = \int_0^t E(\xi(t) - \xi'(\tau)) \frac{d\varepsilon}{d\tau} d\tau \qquad (8)$$

where σ is the relaxation stress, E is the relaxation modulus, and ε is the strain. ξ and ξ' are reduced time variables that depend on temperature and the degree of cure (see also Equation (12)). For the relaxation modulus, we used the following generalized Maxwell model (Equation (9)) that takes into account the temperature and degree of cure [35]:

$$E(\xi,\alpha) = E_\infty + (E_u - E_\infty) \sum_{i=1}^n W_i \exp\left(\frac{-\xi(\alpha,T)}{\tau_i(\alpha)}\right) \qquad (9)$$

where E_∞ is the fully relaxed modulus, E_u is the unrelaxed modulus, W_i is the weight factor for the ith element, and τ_i is the discrete stress relaxation time of each element. τ_i depends on the degree of cure and is expressed by Equations (10) and (11):

$$\log(\tau_i(\alpha)) = \log(\tau_i(\alpha_{ref})) + f'(\alpha) - $$
$$- (\alpha - \alpha_{ref}) \log\left(\frac{\tau_p(\alpha_{ref})}{\tau_i(\alpha_{ref})}\right) \qquad (10)$$

$$f'(\alpha) = 0.0536 + 0.0615\alpha + 0.9227\alpha^2 - 1 \qquad (11)$$

where α_{ref} is the reference degree of cure (= 0.98), and τ_p is the maximum stress relaxation time at the reference degree of cure. The reduced times are given by Equation (12):

$$\xi = \int_0^t \frac{1}{a_T} dt, \ \xi' = \int_0^\tau \frac{1}{a_T} dt,$$
$$\log a_T = \left(-a_1 \exp\left(\frac{1}{\alpha-1}\right) - a_2\right)(T - T_{ref}) \qquad (12)$$

where a_T is the shift factor, T_{ref} (= 30 °C) is the reference temperature, and a_1 and a_2 are material-dependent parameters.

2.2.3. Residual stress analysis using finite element method

The residual stress is calculated using the finite element method on the basis of the principle of virtual work (see Equation (13)):

$$\int_V (\delta\varepsilon)^T \sigma_{res} dV = \int_V (\delta\mathbf{u})^T \mathbf{b} dV + \int_V (\delta\mathbf{u}) \mathbf{t} dS \qquad (13)$$

where ε is the total strain vector, $\mathbf{u}$ is the displacement vector, $\mathbf{b}$ is the body force vector per unit volume, $\mathbf{t}$ is the surface force vector per unit area, and S is the mechanical boundary [m^2].

Let us consider the unknown state at the time $t = t + \Delta t$, where the state at the time t is known. Equation (13) can then be linearized as shown by Equation (14):

$$\Delta t \int_{V_t} (\delta\varepsilon)^T \dot{\sigma}_{res} dV = \int_{V_{t'}} (\delta\mathbf{u})^T \mathbf{b} dV + \int_{S_{t'}} (\delta\mathbf{u}) \mathbf{t} dS - $$
$$- \int_{V_t} (\delta\varepsilon)^T \sigma_{res} dV \qquad (14)$$

where the subscripts t and t' for V and S represent the system states at times t and t', respectively. The total strain rate vector $\dot{\varepsilon}$ is composed of the residual strain rate vector $\dot{\varepsilon}_{res}$ and the initial strain rate vector $\dot{\varepsilon}_0$, which can be expressed in terms of the volumetric strain change (see Equation (15)):

$$\dot{\varepsilon} = \dot{\varepsilon}_{res} + \dot{\varepsilon}_0 = \dot{\varepsilon}_{res} + \left\{ \frac{1}{3V_0} \frac{dV}{dt} \ \frac{1}{3V_0} \frac{dV}{dt} \ 0 \right\}^T \qquad (15)$$

$\dot{\sigma}_{res}$ is given as follows, using the stress–strain and strain–displacement matrices $\mathbf{D}$ and $\mathbf{B}$, respectively, as described by Equation (16):

$$\dot{\sigma}_{res} = \mathbf{D}\dot{\varepsilon}_{res} = \mathbf{D}(\dot{\varepsilon} - \dot{\varepsilon}_0) = \mathbf{D}(\mathbf{B}\dot{\mathbf{d}}_e - \dot{\varepsilon}_0) \qquad (16)$$

where $\dot{\mathbf{d}}_e$ represents the nodal displacement vector in an element. Here, $\mathbf{D}$ is composed of the relaxation modulus E and Poisson's ratio v. It should be noted that the Poisson's ratio is constant and does not depend on the degree of cure [2]. By substituting Equation (16) into Equation (14), the following Equation (17) can be obtained:

$$\int_{V_t} (\delta\varepsilon)^T \mathbf{D}(\Delta\varepsilon - \Delta\varepsilon_0) dV = \int_{V_{t'}} (\delta\mathbf{u})^T \mathbf{b} dV + $$
$$+ \int_{S_{t'}} (\delta\mathbf{u}) \mathbf{t} dS - \int_{V_t} (\delta\varepsilon)^T \sigma_{res} dV \qquad (17)$$

Using the total nodal displacement vector $\Delta\mathbf{d}$ and $\mathbf{B}$ when the body and surface forces are zero, Equation (17) can be rewritten as shown by Equation (18):

$$\left(\sum_{elements} \int_{V_t} \mathbf{B}^T \mathbf{D} \mathbf{B} dV\right) \Delta\mathbf{d} = $$
$$= \sum_{elements} \int_{V_t} \mathbf{B}^T \mathbf{D} \Delta\varepsilon_0 dV - \sum_{elements} \int_{V_t} \mathbf{B}^T \sigma_{res} dV \qquad (18)$$

By solving the system of linear equations in Equation (18), we can obtain the total nodal displacement vector $\Delta\mathbf{d}$; thereby, the residual stress $\dot{\boldsymbol{\sigma}}_{res}$ can be calculated from Equation (16).

2.3. Simulation of residual stress

2.3.1. Analytical conditions

We investigated the effect of the curing process on the residual stress by modeling the interdigital electrodes, as shown in Figure 4a. We compared models of external heating by heat flux and internal heating by an electric field, schematically illustrated in Figures 4b and 4c, respectively. In the models, the heat transfer coefficient h between the resin at the top of the model and the atmosphere was 10 W/(m^2·K), and the initial temperatures of the resin (T_0) and atmosphere (T_w) was 25 °C. The electrical conductivity distribution of the 0.2 wt% CNT-loaded resin shown in Figure 2e was used for the inhomogeneous electrical conductivity model, while a constant electric conductivity $\sigma_e = 10^{-3}$ S/m was employed in the homogeneous model, corresponding to the average electrical conductivity of the 0.2 wt% CNT-loaded resin. The applied voltage V was set to a value such that the minimum degree of cure in the model reached 0.95 after 1600 s from the start of the analysis. The applied voltages and heat flux values for heating the CNT-filled resin are summarized in Table 1. The residual stress was analyzed by the finite element method using four-node quadrilateral elements, assuming a plane-strain state. To establish the boundary conditions, the y directional displacement was constrained to the bottom line; an x directional displacement constraint was also added at the middle point of the bottom line to keep the model fixed. The material properties are shown in Tables 2 and 3 [33–36]. In addition, we investigated more rapid and uniform curing cases: the interdigital elec-

Table 1. Values of applied voltage and heat flux for heating the CNT-filled resin from the bottom of the model

Heat flux q [J/(m^2·s)]	753.2
Applied voltage (homogeneous model) [V]	72.1
Applied voltage (inhomogeneous model) [V]	42.8

Table 2. Material properties and parameters of cure kinetics and volumetric change for the thermosetting resin (Equations (1)–(7)) [33, 34, 36]

ρ	[kg/m^3]	1094.9
K	[W/(m·K)]	0.14
c	[J/(mol·kg)]	1630
k_1	[1/K]	$6.167 \cdot 10^{20}$
E_a	[J/mol]	$1.674 \cdot 10^5$
m		0.524
n		1.476
R	[J/(mol·K)]	8.314
H_r	[J/kg]	$7.750 \cdot 10^4$
e_1	[J/(mol·K)]	$9.167 \cdot 10^{-7}$
e_2	[J/(mol·K)]	$9.167 \cdot 10^{-3}$
f_1	[J/kg]	$2.425 \cdot 10^5$
f_2	[J/kg]	$5.250 \cdot 10^{-5}$
λ_{chem}		0.07

Table 3. Constants of the viscoelastic model for $\alpha_{ref} = 0.98$ (Equations (8)–(12)) [35]

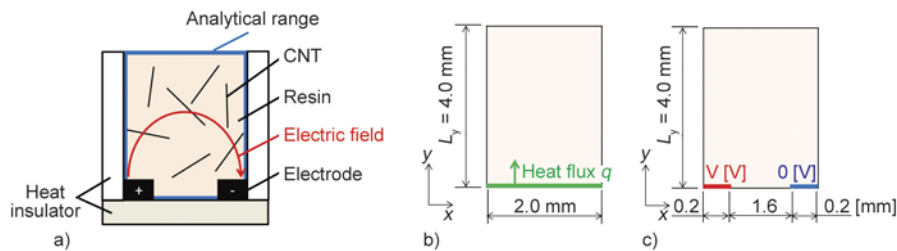| i	τ_i [min]	W_i
1	$2.92 \cdot 10^1$	0.059
2	$2.92 \cdot 10^3$	0.066
3	$1.82 \cdot 10^5$	0.083
4	$1.10 \cdot 10^7$	0.112
5	$2.83 \cdot 10^8$	0.154
6	$7.94 \cdot 10^9$ (τ_p)	0.262
7	$1.95 \cdot 10^{11}$	0.184
8	$3.32 \cdot 10^{12}$	0.049
9	$4.92 \cdot 10^{14}$	0.025
E_∞ [GPa]	0.031	
E_u [GPa]	0.32	
a_1 [1/K]	1.4	
a_2 [1/K]	0.0712	

Figure 4. Analytical models and applied voltage conditions using electrodes and heat flux for heating the CNT-filled resins for single-sided heating. (a) Schematic cross-sectional view of the analytical model by (b) heat flux and (c) electric field using electrodes.
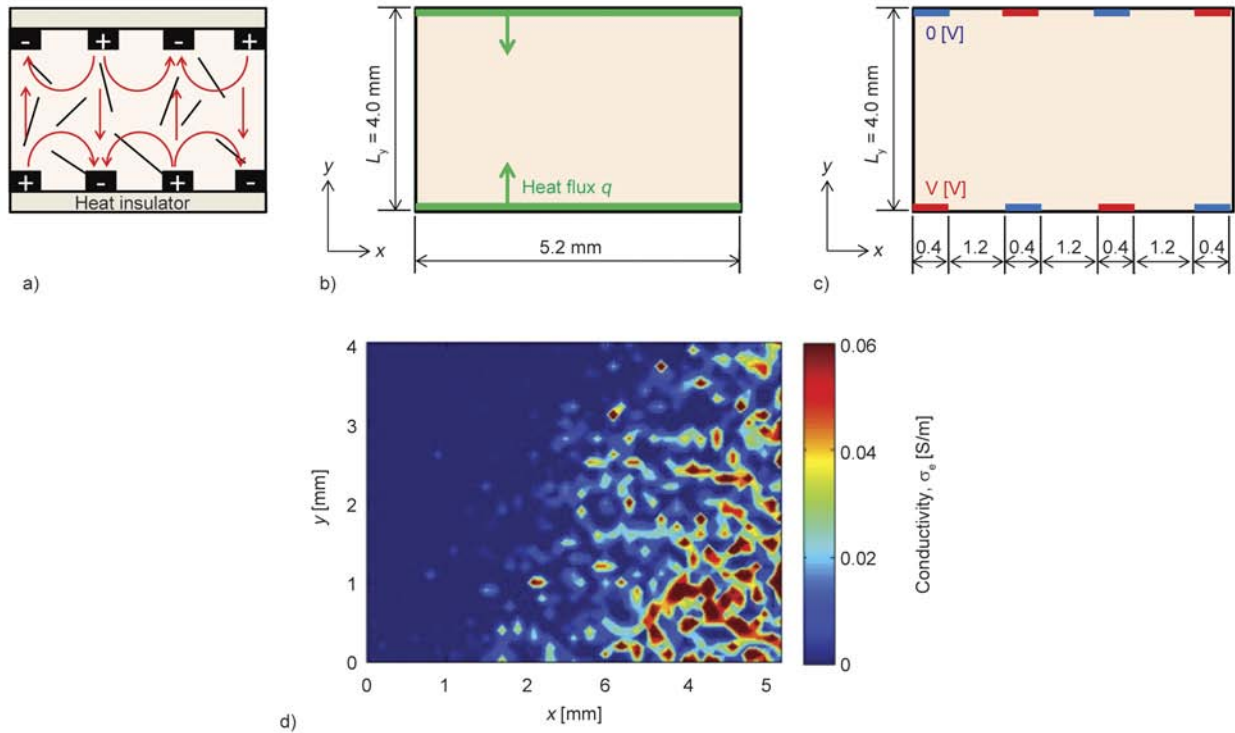
Figure 5. Analytical models and applied voltage conditions using electrodes and heat flux for heating the CNT-filled resins for double-sided heating. (a) Cross-sectional view of analytical model by (b) heat flux and (c) electric field using electrodes. (d) Inhomogeneous electrical conductivity σe for the double-sided heating model.

Table 4. Values of applied voltage and heat flux for heating the CNT-filled resin from both sides

Heat flux q [J/(m²·s)]	561.7
Applied voltage (homogeneous model) [V]	53.1
Applied voltage (inhomogeneous model) [V]	17.1

trode films were placed on the upper and lower surfaces of the mold, and the electric field was applied to the CNT-filled resin between the mold plates, as shown in Figure 5a. Figure 5b and 5c show schemes of heat-flux and electric-field heating, respectively; the heat flux and electric field parameters are summarized in Table 4. Homogeneous ($\sigma_e = 10^{-3}$ S/m) and inhomogeneous models (Figure 5d) of the electrical conductivity of the CNT-filled resin were also obtained.

3. Results and discussion

Figure 6 shows the distributions of residual stress in the x and y directions after 3600 s of heating by heat flux and an electric field in both homogeneous and inhomogeneous models. The results show that the residual stress is suppressed in the case of electric-field heating, compared with the case of heat-flux heating. The different residual stress distributions are attributed to the non-uniform curing process
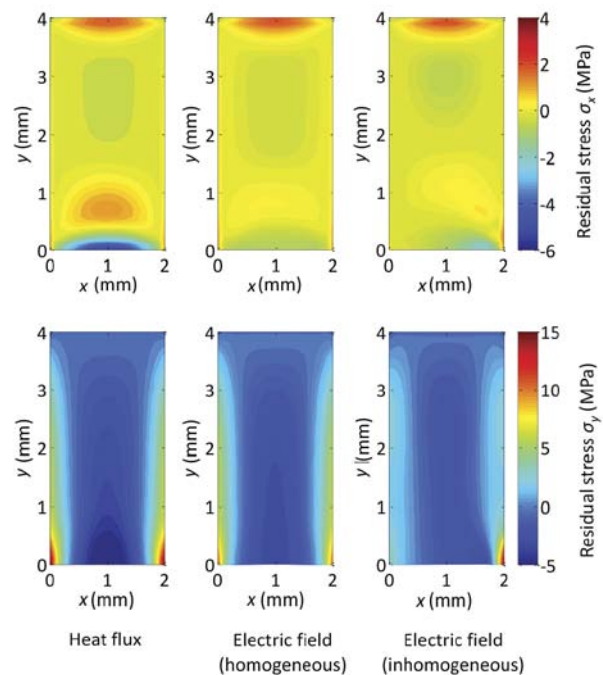
Figure 6. Cross-sectional contour plots of residual stresses σx and σy of CNT-filled resin heated from the bottom of the mold. After 3600 s of heating by heat flux and electric field.

along the thickness direction. Figure 7 shows the difference between the maximum and minimum degree of cure ($\alpha_{y=0} - \alpha_{y=4}$) at $x = 1.0$ mm. Around
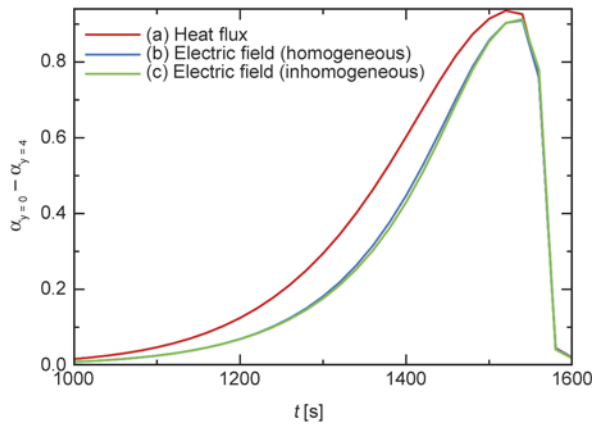
Figure 7. Difference between maximum and minimum degree of cure (α_{max} and α_{min}) at $x = 1.0$ mm of CNT-filled resin heated from the bottom of the mold

1000–1600 s, the difference in the degree of cure for electric-field heating (homogeneous and inhomogeneous) case is smaller than the difference observed for heat-flux heating. This happens because upon application of the electric field, the Joule heating generates heat inside the model; thus, heating and curing can progress uniformly along the thickness direction. In the present analytical model, residual stress occurs because the part that is already cured constrains the cure shrinkage of the portion whose curing is still in progress. Therefore, the uniform curing progress achieved by applying the electric field successfully prevents the development of residual stress. Compared to the homogeneous-electrical-conductivity model, a higher local residual stress can be seen in the lower right region of the inhomogeneous model.

Figure 8 shows the residual stress in the case of double-sided heating. Similar to the case of one-sided heating, the electric-field heating generally suppresses residual stress compared with the heat-flux model. However, very high local residual stress is present in the lower right region of the inhomogeneous model, even compared with the heat-flux model. This is due to the very high electrical conductivity in the lower right part of the inhomogeneous model, as shown in Figure 5d, and to the large amount of heat generated in the high-electrical-conductivity region.

4. Conclusions

In the present study, numerical simulations were performed to evaluate the residual stress of CNT-filled resins cured under an electric field, taking into account the distribution of CNTs in the resins. The simulations were set up using the linear viscoelastic model and the unsteady-heat-transfer equation for the heat generated by Joule heating and the cure reaction. In addition, microscope images of actual CNT-filled resins were used to model the inhomogeneous electric conductivity due to CNT aggregates. The simulation results show that compared with external heating using heat flux, even though the electric field generally suppresses the residual stress, the inhomogeneous electrical conductivity due to the CNT aggregates may induce very high local residual stress. Therefore, in order to accurately determine the residual stress of CNT-filled resins, it is necessary to take into consideration the inhomogeneity of the electrical conductivity.
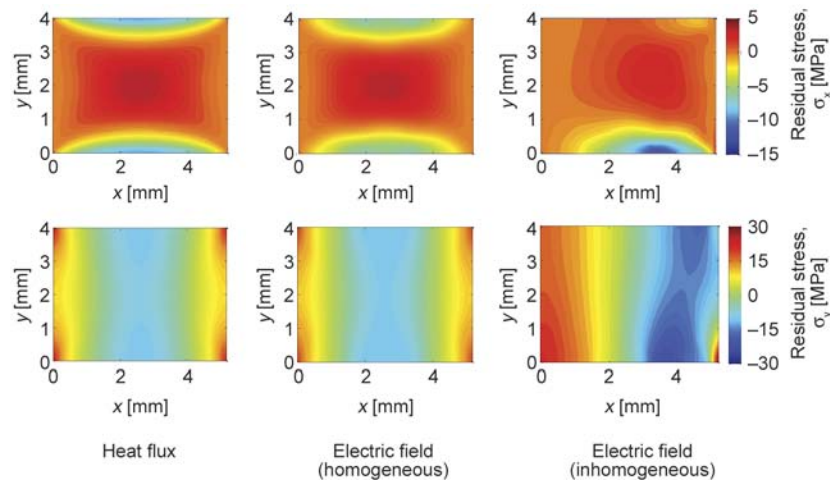

Figure 8. Cross-sectional contour plots of residual stresses σ_x and σ_y for CNT-filled resin heated from both sides of the mold after 3600 s of heating by heat flux and electric field

References

[1] Plepys A. R., Farris R. J.: Evolution of residual stresses in three-dimensionally constrained epoxy resins. Polymer, **31**, 1932–1936 (1990).
DOI: 10.1016/0032-3861(90)90019-U

[2] Bogetti T. A., Gillespie Jr J. W.: Process-induced stress and deformation in thick-section thermoset composite laminates. Journal of Composite Materials, **26**, 626–660 (1992).
DOI: 10.1177/002199839202600502

[3] Thostenson E. T., Chou T-W.: Microwave and conventional curing of thick-section thermoset composite laminates: Experiment and simulation. Polymer Composites, **22**, 197–212 (2001).
DOI: 10.1002/pc.10531

[4] Maenz S., Mühlstädt M., Jandt K. D., Bossert J.: Mechanical properties of microwave cured glass fibre epoxy composites prepared by resin transfer moulding. Journal of Composite Materials, in press (2014).
DOI: 10.1177/0021998314557295

[5] Papargyris D. A., Day R. J., Nesbitt A., Bakavos D.: Comparison of the mechanical and physical properties of a carbon fibre epoxy composite manufactured by resin transfer moulding using conventional and microwave heating. Composites Science and Technology, **68**, 1854–1861 (2008).
DOI: 10.1016/j.compscitech.2008.01.010

[6] Zhou J., Shi C., Mei B., Yuan R., Fu Z.: Research on the technology and the mechanical properties of the microwave processing of polymer. Journal of Materials Processing Technology, **137**, 156–158 (2003).
DOI: 10.1016/s0924-0136(02)01082-8

[7] Tanrattanakul V., Jaroendee D.: Comparison between microwave and thermal curing of glass fiber–epoxy composites: Effect of microwave-heating cycle on mechanical properties. Journal of Applied Polymer Science, **102**, 1059–1070 (2006).
DOI: 10.1002/app.24245

[8] Zhou S., Hawley M. C.: A study of microwave reaction rate enhancement effect in adhesive bonding of polymers and composites. Composite Structures, **61**, 303–309 (2003).
DOI: 10.1016/s0263-8223(03)00061-8

[9] Chen M., Siochi E. J., Ward T. C., McGrath J. E.: Basic ideas of microwave processing of polymers. Polymer Engineering and Science, **33**, 1092–1109 (1993).
DOI: 10.1002/pen.760331703

[10] Bayerl T., Duhovic M., Mitschang P., Bhattacharyya D.: The heating of polymer composites by electromagnetic induction – A review. Composites Part A: Applied Science and Manufacturing, **57**, 27–40 (2014).
DOI: 10.1016/j.compositesa.2013.10.024

[11] Thostenson E. T., Chou T-W.: Microwave processing: Fundamentals and applications. Composites Part A: Applied Science and Manufacturing, **30**, 1055–1071 (1999).
DOI: 10.1016/S1359-835X(99)00020-2

[12] Higginbotham A. L., Moloney P. G., Waid M. C., Duque J. G., Kittrell C., Schmidt H. K., Stephenson J. J., Arepalli S., Yowell L. L., Tour J. M.: Carbon nanotube composite curing through absorption of microwave radiation. Composites Science and Technology, **68**, 3087–3092 (2008).
DOI: 10.1016/j.compscitech.2008.07.004

[13] Rangari V. K., Bhuyan M. S., Jeelani S.: Microwave curing of CNFs/EPON-862 nanocomposites and their thermal and mechanical properties. Composites Part A: Applied Science and Manufacturing, **42**, 849–858 (2011).
DOI: 10.1016/j.compositesa.2011.03.014

[14] Sung P-C., Chiu T-H., Chang S-C.: Microwave curing of carbon nanotube/epoxy adhesives. Composites Science and Technology, **104**, 97–103 (2014).
DOI: 10.1016/j.compscitech.2014.09.003

[15] Liu F., Qian X., Wu X., Guo C., Lei Y., Zhang J.: The response of carbon black filled high-density polyethylene to microwave processing. Journal of Materials Processing Technology, **210**, 1991–1996 (2010).
DOI: 10.1016/j.jmatprotec.2010.07.014

[16] Wang G., Tan Z., Liu X., Chawda S., Koo J-S., Samuilov V., Dudley M.: Conducting MWNT/poly(vinyl acetate) composite nanofibres by electrospinning. Nanotechnology, **17**, 5829–5835 (2006).
DOI: 10.1088/0957-4484/17/23/019

[17] Reia da Costa E. F., Skordos A. A., Partridge I. K., Rezai A.: RTM processing and electrical performance of carbon nanotube modified epoxy/fibre composites. Composites Part A: Applied Science and Manufacturing, **43**, 593–602 (2012).
DOI: 10.1016/j.compositesa.2011.12.019

[18] Bauhofer W., Kovacs J. Z.: A review and analysis of electrical percolation in carbon nanotube polymer composites. Composites Science and Technology, **69**, 1486–1498 (2009).
DOI: 10.1016/j.compscitech.2008.06.018

[19] Wang L., Dang Z-M.: Carbon nanotube composites with high dielectric constant at low percolation threshold. Applied Physics Letters, **87**, 042903/1–042903/3 (2005).
DOI: 10.1063/1.1996842

[20] Rul S., Lefèvre-schlick F., Capria E., Laurent C., Peigney A.: Percolation of single-walled carbon nanotubes in ceramic matrix nanocomposites. Acta Materialia, **52**, 1061–1067 (2004).
DOI: 10.1016/j.actamat.2003.10.038

[21] Khare R., Bose S.: Carbon nanotube based composites – A review. Journal of Minerals and Materials Characterization and Engineering, **4**, 31–46 (2005).
DOI: 10.4236/jmmce.2005.41004

[22] Lee S-B., Choi O., Lee W., Yi J-W., Kim B-S., Byun J-H., Yoon M-K., Fong H., Thostenson E. T., Chou T-W.: Processing and characterization of multi-scale hybrid composites reinforced with nanoscale carbon reinforcements and carbon fibers. Composites Part A: Applied Science and Manufacturing, **42**, 337–344 (2011).
DOI: 10.1016/j.compositesa.2010.10.016

[23] Gibson R. F.: A review of recent research on mechanics of multifunctional composite materials and structures. Composite Structures, **92**, 2793–2810 (2010).
DOI: 10.1016/j.compstruct.2010.05.003

[24] Kobayashi S., Matsuzaki R., Todoroki A.: Multipoint cure monitoring of CFRP laminates using a flexible matrix sensor. Composites Science and Technology, **69**, 378–384 (2009).
DOI: 10.1016/j.compscitech.2008.10.029

[25] Matsuzaki R., Kobayashi S., Todoroki A., Mizutani Y.: Control of resin flow/temperature using multifunctional interdigital electrode array film during a VaRTM process. Composites Part A: Applied Science and Manufacturing, **42**, 782–793 (2011).
DOI: 10.1016/j.compositesa.2011.03.004

[26] Matsuzaki R., Kobayashi S., Todoroki A., Mizutani Y.: Full-field monitoring of resin flow using an area-sensor array in a VaRTM process. Composites Part A: Applied Science and Manufacturing, **42**, 550–559 (2011).
DOI: 10.1016/j.compositesa.2011.01.014

[27] Matsuzaki R., Kobayashi S., Todoroki A., Mizutani Y.: Cross-sectional monitoring of resin impregnation using an area-sensor array in an RTM process. Composites Part A: Applied Science and Manufacturing, **43**, 695–702 (2012).
DOI: 10.1016/j.compositesa.2011.12.024

[28] Hatori S., Matsuzaki R., Todoroki A.: Cost-effective open microwave heating of polymer resin using interdigital electrode array film and dispersed carbon nanotubes. Composites Science and Technology, **92**, 9–15 (2014).
DOI: 10.1016/j.compscitech.2013.11.029

[29] Bykov Y. V., Rybakov K. I., Semenov V. E.: High-temperature microwave processing of materials. Journal of Physics D: Applied Physics, **34**, R55–R75 (2001).
DOI: 10.1088/0022-3727/34/13/201

[30] Fotiou I., Baltopoulos A., Vavouliotis A., Kostopoulos V.: Microwave curing of epoxy polymers resinforced with carbon nanotubes. Journal of Applied Polymer Science, **129**, 2754–2764 (2013).
DOI: 10.1002/app.39003

[31] Mas B., Fernández-Blázquez J. P., Duval J., Bunyan H., Vilatela J. J.: Thermoset curing through joule heating of nanocarbons for composite manufacture, repair and soldering. Carbon, **63**, 523–529 (2013).
DOI: 10.1016/j.carbon.2013.07.029

[32] Li J., Ma P. C., Chow W. S., To C. K., Tang B. Z., Kim J-K.: Correlations between percolation threshold, dispersion state, and aspect ratio of carbon nanotubes. Advanced Functional Materials, **17**, 3207–3215 (2007).
DOI: 10.1002/adfm.200700065

[33] Park H. C., Lee S. W.: Cure simulation of thick composite structures using the finite element method. Journal of Composite Materials, **35**, 188–201 (2001).
DOI: 10.1177/002199801772662217

[34] Ruiz E., Trochu F.: Numerical analysis of cure temperature and internal stresses in thin and thick RTM parts. Composites Part A: Applied Science and Manufacturing, **36**, 806–826 (2005).
DOI: 10.1016/j.compositesa.2004.10.021

[35] Kim Y. K., White S. R.: Stress relaxation behavior of 3501-6 epoxy resin during cure. Polymer Engineering and Science, **36**, 2852–2862 (1996).
DOI: 10.1002/pen.10686

[36] Rouison D., Sain M., Couturier M.: Resin transfer molding of natural fiber reinforced composites: Cure simulation. Composites Science and Technology, **64**, 629–644 (2004).
DOI: 10.1016/j.compscitech.2003.06.001

Compressibility of carbon fabrics with needleless electrospun PAN nanofibrous interleaves

S. V. Lomov[1*]*, K. Molnár*[2,3]

[1]Department of Materials Engineering, KU Leuven, Kasteelpark Arenberg 44, 3001 Leuven, Belgium
[2]Department of Polymer Engineering, Faculty of Mechanical Engineering, Budapest University of Technology and Economics, Műegyetem rkp. 3., H-1111, Budapest, Hungary
[3]MTA–BME Research Group for Composite Science and Technology, Műegyetem rkp. 3., H-1111, Budapest, Hungary

Abstract. The present paper investigates how the presence of nanofiber interleaves affects the compressibility of the layup during manufacturing of the composites and hence determining the theoretically attainable fiber volume fraction at the given processing pressure. The results show that up to the interleave areal density of 10 g/m^2 per nanofiber layer the decrease of fiber volume fraction does not exceed 3% for a laminate of carbon fiber woven fabric. Interleaves inside a fabric laminate are more compressible than a plain electrospun veil. It can be explained as the nanofibers penetrate between the carbon fibers when applying compression during composite manufacturing. It can be stated that there is a strong interference between the interleaves and the carbon reinforcement, which can lead to effective toughness improvement of the composite without significant alteration of fiber volume content.

Keywords: polymer composites, needleless electrospinning, carbon fiber, nanofiber, compressibility

1. Introduction

Electrospinning is a simple and popular method for producing different nanofiber structures, fiber mats are the most common format. These nanofiber webs can have several applications, including medical [1–3], pharmaceutical [4, 5], sensor [6], filtering [7–9], clothing, construction engineering applications as well as composites [10, 11]. Nanofibers have unique properties such as high surface to mass ratio and flexibility that makes possible to use them as reinforcement of composites. Polymer nanofibers can be applied as a secondary reinforcement of hybrid composites, where thin fiber meshes are applied as interleaves. Such application of electrospun nanofibers was patented by Dzenis and Reneker [12]. Thin nanofiber interleaves of several micrometres can hinder crack propagation and moreover it seems that the thickness – and therefore the in-

plane properties – of the laminate are not altered significantly. Nanofiber layers can increase both the quasi-static and impact [13–15] performance of composites. The appropriate pressure and material selection is crucial for achieving a significant improvement in interlaminar properties. Theoretically, by adjusting the thickness of the interleaves and choosing the appropriate nanofiber material the properties of the composite can be tailored from rigid to tough kind of damage. This effect was demonstrated experimentally for Nylon 6.6 interleaves in [16, 17].

The toughening effect of polyacrylonitrile (PAN) nanofibrous interleaves in carbon fiber-reinforced structures was proved in [18]. It was demonstrated that the presence of electrospun PAN nanofibrous interleaves can effectively increase the impact properties of carbon reinforced composites without

---

compromising their in-plane mechanical properties. This was achieved with low weight fraction of the nanofibers, which do not alter the thickness of the composite laminates. Thicker interleaves may potentially improve the quality of the toughening, but they can significantly alter the thickness of composites, therefore reducing their in-plane strength. The compressibility of fibers and the consequent thickness of composites also influence residual stresses and geometrical unconformities in the produced part [19, 20]. The present paper investigates how the presence of the interleaves of different areal weight affects compressibility of the fabric layup during manufacturing of the composites and hence the fiber volume fraction attainable at the given processing pressure.

Fibrous nano-additions, even in small amounts, can significantly increase the compression resistance of fabric layups. This was demonstrated for the case of carbon nanotubes (CNT) grown on fibers (woven fabrics), both for random and aligned CNT forests [21–23]. For the CNT load of about 10 g/m² per fabric layer the layup thickness increases up to 20% for a random CNT forest and up to 30% for an aligned CNT forest at the same compaction pressure. This increase of the layup thickness decreases proportionally the fiber volume fraction in the composite laminate, significantly compromising its in-plane mechanical properties. This phenomenon is also observed in fabrics without nano-additions [24, 25]. The high compression resistance of the CNT forests, which is transformed in the CNT-grafted fabric in the low compressibility of the layups, is explained in [26, 27] by high contacts density in a CNT forest and high resistance of the stiff CNTs to bending.

Compression behavior of random fibrous assemblies is controlled by a number of factors as fiber bending rigidity and friction and fiber orientation and density in an assembly. Descriptive and to certain extent predictive theories for compression resistance can be found in [28, 29]. So far as the listed properties of two different fiber assemblies are close, one can expect that the compression response of these assemblies is close as well; the differences of these properties lead to different compression resistance.

Electrospun nanofibers have larger bending rigidity than CNTs. Bending rigidity of a typical multiwall CNT with diameter of 20 nm, 20 walls and the wall Young modulus of 1000 GPa is estimated as

$1 \cdot 10^{-20}$ N·m² [26]. Bending rigidity of a typical PAN nano-fiber with diameter of 200 nm [20] and Young modulus of 8 GPa [30] is estimated as $1 \cdot 10^{-17}$ N·m². The larger bending rigidity brings larger compaction resistance. Moreover, the coefficient of friction for PAN fibers (about 0.3 [31]) is much higher than that of CNTs (about 0.005 [32, 33]), which will also brings higher compaction resistance. However, the orientation distribution of PAN fibers in an interleave is close to in-plane, whilst CNTs' orientation distribution in a forest grown on the fibers is either close to being spatially uniform or to radial alignment. Also the number of contacts per unit volume between the PAN fibers is much lower than in a CNT forest with the same areal density due to larger diameter of the PAN fibers. These factors (flat orientation and lower number of contacts) decrease the compaction resistance of a PAN nano-fiber interleave or veil in comparison with CNT forests. The two competing tendencies make it difficult to predict *a priori*, whether the compaction resistance of fabrics with PAN nanofiber interleaves will follow the same trend as of the previously studied fabrics with grown CNTs, and whether the fiber volume fraction of laminates with PAN nanofiber interleaves will be significantly compromised for higher nanofiber contents. The present paper seeks an experimental answer to this question. We will see that the compression resistance of carbon fabrics is affected by the presence of PAN nanofiber interleaves less than by CNT growth.

2. Materials and sample preparation
Nanofibers are generated from polyacrilonitrile (PAN) powder dissolved in dimethyl-formamide (DMF) in a concentration of 12 mass%. The PAN was supplied by a carbon fiber manufacturer that wished to be anonymous, while DMF was a product of Molar Chemicals, Hungary.

The nanofibers were produced by a novel method, called *corona*-electrospinning developed by Molnár *et al*. [34]. The schematic drawing of the electrospinning setup can be seen in Figure 1. The setup consists of a high voltage power supply, a rotating needleless spinneret, a sheet metal collector electrode, a solution feed unit and moving belt that is just in front of the collector screen and therefore nanofibers are deposed on the surface of this substrate making possible the continuous nanofiber production.
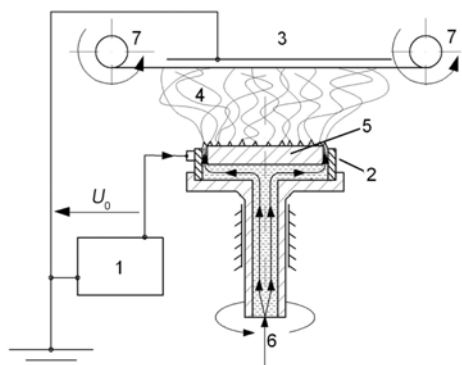
Figure 1. The applied electrospinning setup, 1: high voltage power supply, 2: circular electrode having sharp edge, 3: grounded collector screen, 4: fiber formation space, 5: lid, 6: solution feed, 7: traction of the collector textile (coating of the carbon fabrics takes place between these rolls) [34]

The method compared to the single-needle setup has a high throughput. The solution is continuously fed through a circular-shaped duct that is bounded by a sharp metal edge from outside and a plastic lid from inside. High local field strength is formed along the sharp metal edge and Taylor-cones are formed from the liquid contacting this edge. The forming cones along the circular electrode look like a medieval crown and thus the name was given for the technology. The slight rotation of the whole spinneret is necessary to homogeneously disperse the solution material along the electrode hence avoiding the local overflow of the solution.

In our experiments the *corona-spinneret* was an aluminum-based construction having a diameter of 100 mm. The rotation speed was 120 rpm. MA2000 NT 65/P (Hungary) type power supply was used to generate the necessary high voltage of 55 kV for

fiber formation. Solution was fed through a syringe pump (Aitecs SEP-10P Plus, Lithuania) with a flow rate of 30 mL/h. To remove the evaporated solvent from the electrospinning space, ventilation was applied. Nanofibers in homogeneous layers were produced.

PAN nanofiber veils were deposited on a stationary substrate – 0.2 mm thick aluminum sheet with deposition times of 15 min (3.64 g/m^2), 30 min (5.80 g/m^2), 60 min (17.8 g/m^2), 120 min (52.8 g/m^2). The values in brackets indicate areal density of the veils, measured on a 100×100 mm area. The scatter of these values is about 1 g/m^2 (standard deviation in five measurements). The areal density does not depend linearly on deposition time because it takes time to homogeneously disperse the liquid along the long electrospinning edge. After the starting process a continuous production is developed. In the case of the 15 and 30 min samples the ventilation was used in swinging mode to achieve a more homogeneous deposition of the fibers. That leads to an increased deposition area of the fibers resulting in smaller areal densities.

In order to investigate the interaction of classical fiber and nanofiber layers carbon fabric was coated by nanofibers. Sigratex KDL 8003 (SGL Technologies GmbH, Germany), a plain weave carbon fabric with an areal density of 200 g/m^2 was chosen for these experiments. The carbon fabrics were cut into 200 mm wide strips. The carbon fabric was coated directly by nanofibers as the carbon fabric layer was attached to the rollers (according to Figure 1.) and continuous traction speed of 200 mm/min was applied. In that sense the nanofibers are deposed on

Figure 2. Carbon plain weave fabric without (a) and with (b) PAN nanofiber veil

Table 1. Parameters of the carbon fabric and PAN nanofibers

Fabric		Nanofibers	
ID	Sigratex KDL 8003	Material	PAN
Fibers	HT carbon 3K	Diameter [nm]	195±46
Fabric areal density [g/m^2]	200	Interleave/veil areal density [g/m^2]	5 … 30
Yarn linear density [tex]	200		
Ends/picks count [yarns/cm]	5		
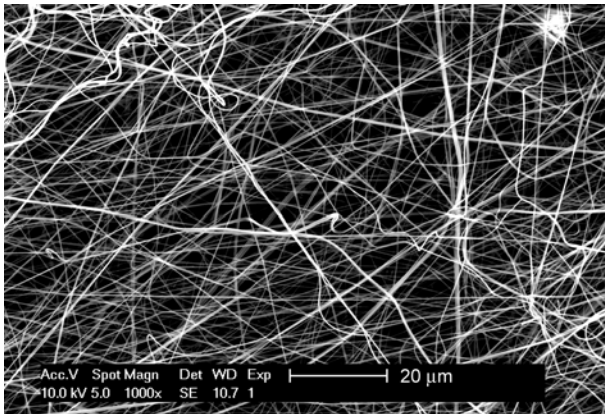
Figure 3. SEM image of PAN nanofiber veil

the surface of the continuously moving carbon fabric stripes. Different coating thicknesses were produced as the carbon fiber material was passing through the equipment 1, 2 and 4 times, respectively. At the compression experiments a reference fabric was also applied (Figure 2). The main data of the applied materials is summarized in Table 1. Figure 2 shows a surface view of the fabric before and after coating, and Figure 3 – a fabric sample with veil.

3. Test method

The test method was the same as the one which was used for measurement of compressibility of fabrics with grown CNT forests [21, 22] where the reader is referred to for more detailed description. Figure 4 shows the test setup as well as representative compression data for four plies of virgin cloth over three loading cycles. In the data in Figure 4, and throughout the manuscript, the sample thickness (*h*) is normalized by the number of plies so that single- and stacked-ply data can be compared directly. Figure 4b shows a nonlinear stiffening response $h = h(p)$, where *p* is the applied pressure, with significant hysteresis. The fiber volume fraction is directly proportional to the thickness. A displacement-controlled testing machine Instron 4467 was used with a 1 kN load cell at a test speed of 1 mm/min. Self-aligning pivots were used (Figure 4a). The compression plate diameter was 70 mm. The specimens of the veils were cut to the size approximately 100×100 mm, and positioned for compression in such a way that the compression plate was situated in the middle of the specimen. To get to higher pressures for fabric and fabric+veil specimens, they were cut to the size of approximatively 50×50 mm, which were placed in the middle of the compression plate. Three tests were first performed without a specimen to establish the reference curves 'displacement of
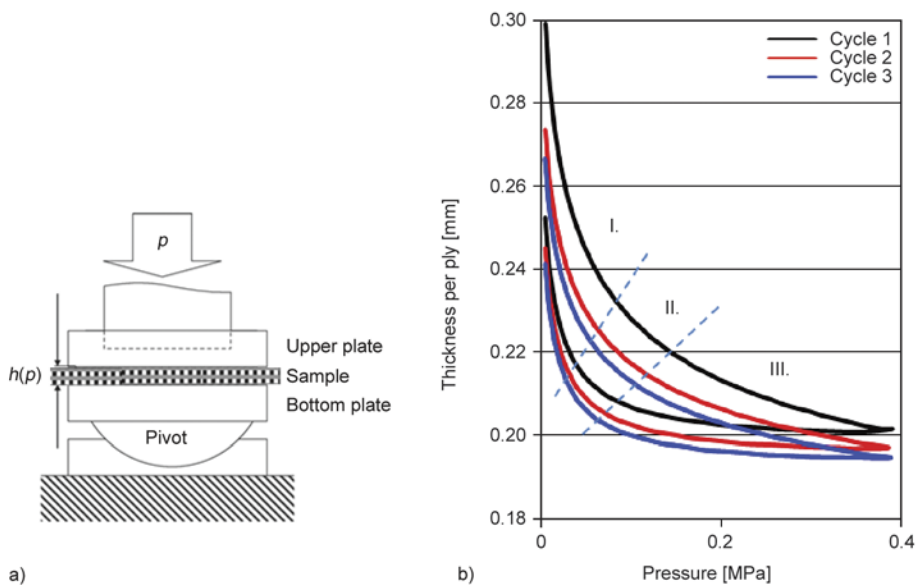

Figure 4. Compression test setup (a) and typical test results (b) – compression curves for compression of four layers of fabric without interleaves

the head x vs pressure' $x_0 = x_0(p)$, so that the specimen thickness was calculated as $h(p) = x(p) - x_0(p)$, where x is the measured head displacement with the specimen. The reference curves were re-registered after testing, to confirm the stability of the measurement. The neat veils produced onto the aluminum sheets were tested in compression together with the aluminum substrate; the reference curve $x_0(p)$ was determined in compression of an empty aluminum sheet.

One fabric layer and four-ply stacks of fabric were tested to study the nesting effects during the compression. Three successive compression cycles (loading-unloading) were performed for each specimen. For each material type (veils of different areal density; fabrics without nanofibers, one layer and four layers; fabrics with nanofibers interleave, one layer and four layers) five specimens were tested, with the three compression cycles imposed on each specimen.

4. Results and discussion

The measured compression diagrams follow patterns typical for compression of fibrous assemblies. The compressibility of random fibrous assemblies in general (non-woven textiles, bulk fibers like wool) is well understood. A typical pressure vs. thickness diagram, shown in Figure 4b, demonstrate the same features as are outlined in [22] for a general case of compression of a textile. Figure 4b shows three successive cycles of compression of the same sample. For each cycle, region I of the diagram (low pressure) is controlled by change of the fiber crimp, and the low compression resistance is given by low bending resistance of the fibers. Region II is intermediate. In the high pressure region III the fibers come close together, the number of contacts of between them increases dramatically, there is no more freedom for the fibers to bend, and the resistance to compression is more and more defined by high Hertzian contact forces rather than by bending of the fibers. Fibers themselves can be considered as not compressible in the range of pressure used in composite manufacturing. If the compaction load is released and then applied again in a second, third etc. cycle, then a certain part of the deformation is not recovered when the load is released, and the thickness under given load decreases for each successive cycle. This hysteresis behavior is studied in [28]. Typically after the third cycle the differences between the sub-

sequent cycles become negligible. For typical composite preforms the practically interesting region of the final state of the preform on the compression diagram is shown in Figure 4b by the rectangle. To reach this range, a typical assembly has to be compacted into regions II–III of the diagram, with pressure from the vacuum range (0.8…1.0 bar) up to several bars.

4.1. Compressibility of PAN nanofiber veils

Figure 5 shows compression diagrams of PAN nanofiber veils (only curves for the veil deposition time 15 and 120 min are shown). Five tests, each with three compression cycles, were done for every variant of the nanofiber deposition time. For better clarity only the 3 most different characteristics are depicted.

One can note a significant unevenness of the veils: the veil thickness at the maximum pressure of 0.23 MPa can be different by two or even three times for the same veil deposition time. All veils show a distinct 'sticking' behavior. After the first compression the compressibility of the veil is drastically decreased, especially for thinner veils (15 min, also observed for 30 min case). Significant hysteresis is observed for the first compression cycle for thinner veils and for all compression cycles for thicker veils (120 min, also observed for 60 min).

In spite of the high scatter, a clear trend of the compressibility can be revealed, if one considers the veil thickness at a given pressure. A natural choice of the pressure level for such a comparison is 0.1 MPa (1 bar), which is characteristic for vacuum assisted composite manufacturing. Thickness of a material at 0.1 MPa pressure in a loading half-cycle will be called in this paper '1 bar thickness'. Figure 6 shows 1 bar veil thickness as a function of veil areal density.

1 bar veil thickness exhibits large scatter for the first compression cycle and stabilizes for the subsequent cycles. The dependency '1 bar veil thickness – veil areal density' is well approximated by a logarithmic function. One can expect that because of an additive nature of depositing the nanofibers the veil thickness should be proportional to the veil areal density. This is not the case. A material with higher areal density densifies more effectively. One can speculate that this reflects the fact that during electrospinning the coverage of the surface by nanofibers is higher for longer deposition times. Fibers try to fill the sur-
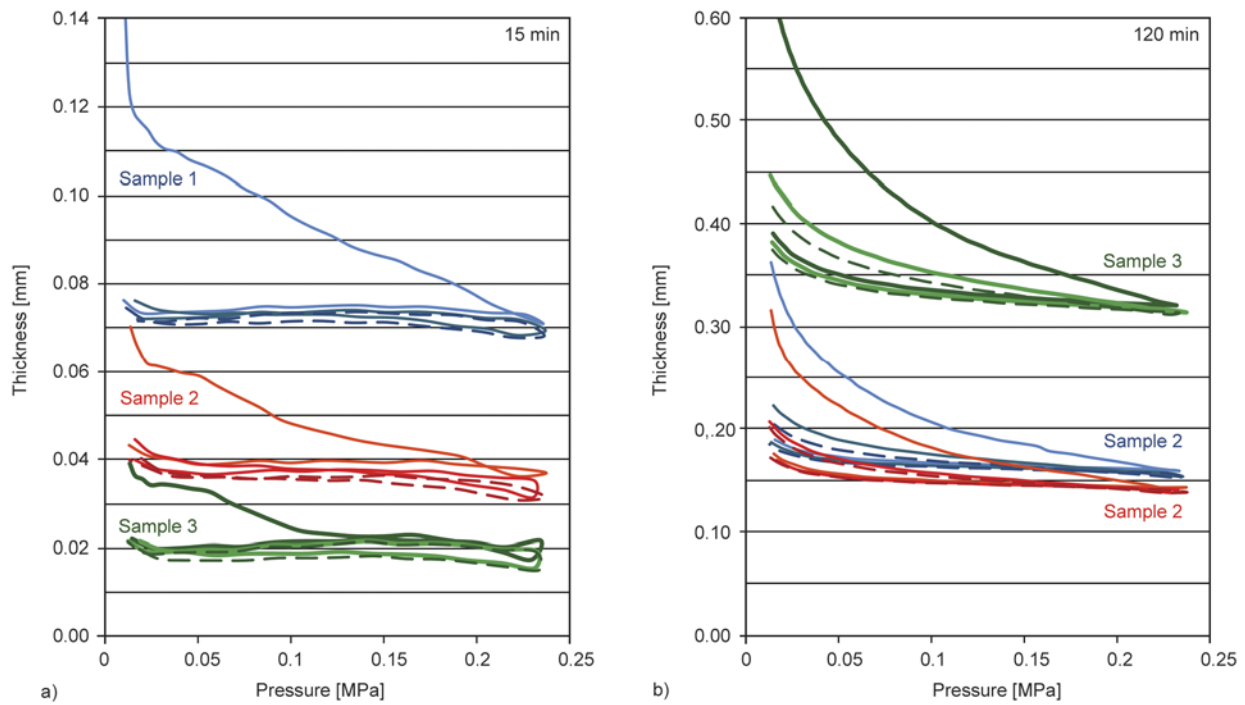
Figure 5. Compression diagrams of PAN nanofiber veils. Veil deposition time: (a) 15 min, (b) 120 min.
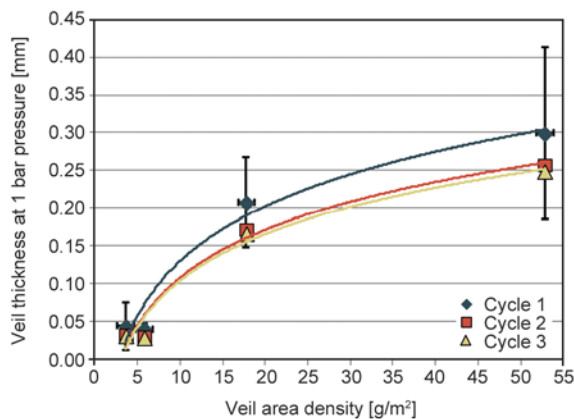

Figure 6. Veil thickness at pressure 1 bar in function of the veil areal density. Error bars show standard deviation in five tests (logarithmic fit was applied).

face first, and then start building up thickness of the veil.

4.2. Compressibility of woven laminates with interleaves

Figure 7 shows compression diagrams obtained from tests with woven laminates with interleaves, as well as compression diagrams for the non-interleaved fabric. The diagrams depict dependency of the thickness of one layer on the applied pressure, for tests with one and four layers in three successive compression cycles. Five diagrams for each variant (three cycles each) of the material are shown together, to give an impression of the scatter of the compaction response.

Each of these five three-cycle diagrams have the same qualitative characteristic shape as shown in Figure 4b.

Standard features of the textile compaction are evidenced by the diagrams for non-interleaved fabric laminates (Figure 7a, 7b, see also Figure 4b): characteristic fast stiffening of the compressed fabric; significant decrease of the compacted stiffness in the second compaction cycle in comparison with the first cycle at the same pressure, and stabilization of the thickness at the third cycle; nesting, i.e. less thickness per one ply in compaction of four fabric plies in comparison with compaction of one ply.

When nanofiber interleaves are added, the compression diagrams are shifted up (compare Figure 7a, 7c, 7e or Figure 7b, 7d, 7f); the thickness of the fabric ply or laminate at a given pressure increases. The increase looks marginal for 5 g/m² veil areal density, but becomes considerable for 28 g/m². The nesting is present also in the case of the presence of the nanofiber interleaves, as well as in their absence (compare Figure 7a–7b, 7c–7d and 7e–7f). To quantify this behavior, the 1 bar fabric ply thickness with and without nanofiber interleaves is considered.

Figure 8a and 8b shows dependency of the 1 bar ply thickness of the areal density of the interleave in one ply. The steady increase of the ply thickness is observed. The rate of increase can be roughly estimated as 3 μm thickness increase per 1 g/m² increase
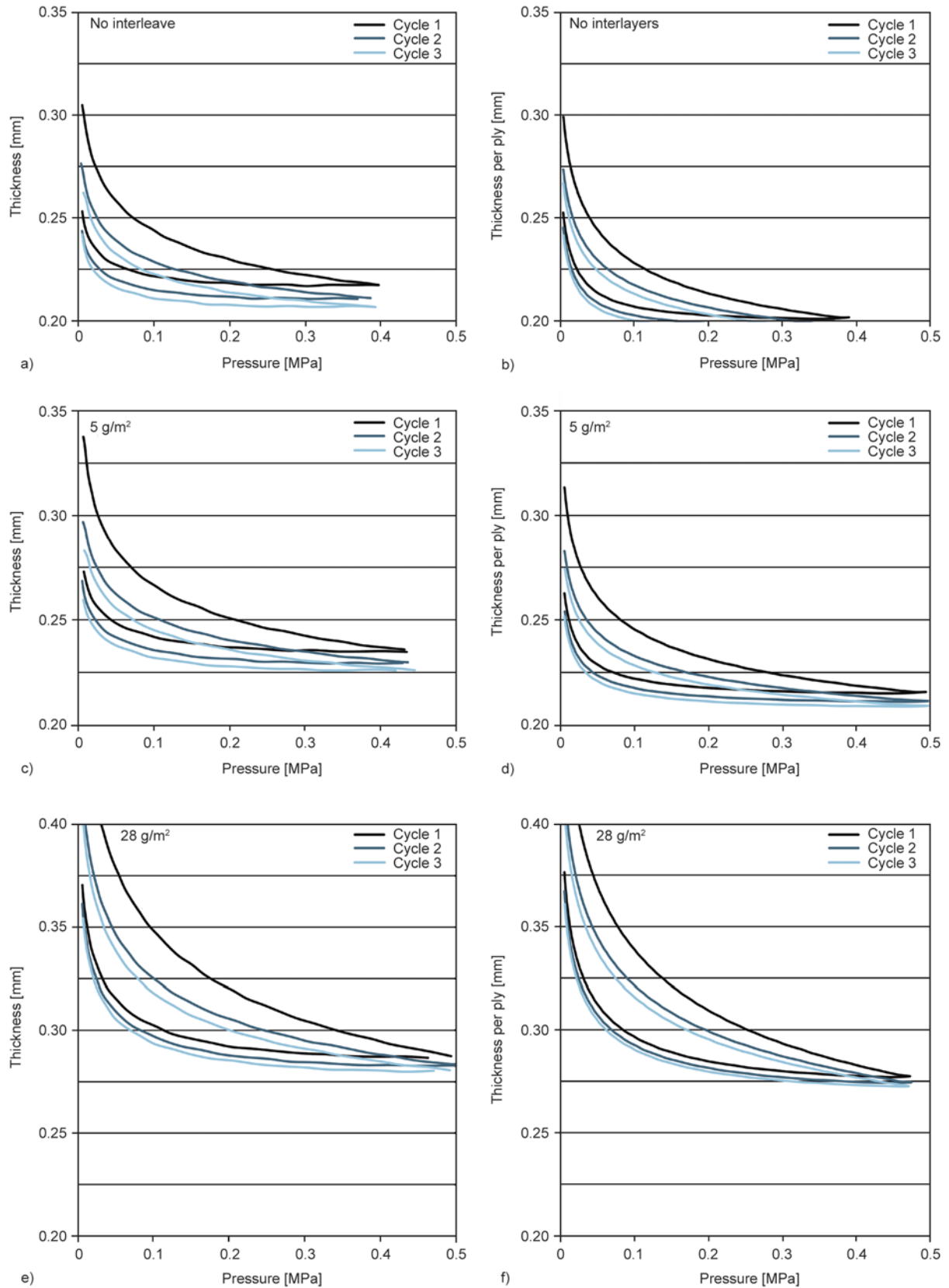
Figure 7. Compression diagrams of carbon woven fabrics with interleaves of PAN nanoveils: thickness of one ply versus pressure. Left column (a, c, e): compression of one fabric ply, right column (b, d, f): compression of four plies. Veil interleave average areal density per ply is shown on the graphs. Diagrams of the most typical curve of the five tests and three compression cycles, are shown in each graph, respectively.
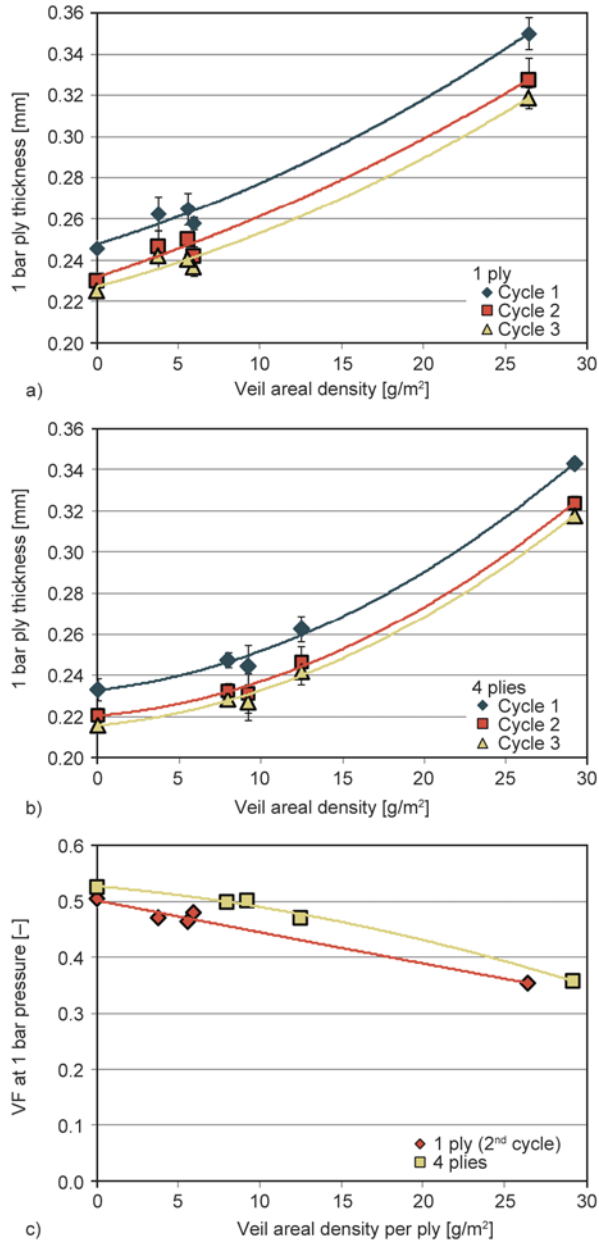
Figure 8. 1 bar ply thickness of carbon woven laminates and fiber volume fraction at 1 bar pressure as functions of the veil areal density: (a) thickness, compression of one ply; (b) thickness, compression of four plies; (c) fiber volume fraction (*VF*)

of the veil areal density. Interestingly in the range of areal density up to 30 g/m² this rate is much smaller than the increase of the 1 bar thickness of the veil itself, compressed without fabric, cf. Figure 6. This phenomenon will be quantified in the next sub-section.

Increase of the laminate thickness leads to decrease of the fiber volume fraction in the consolidated composite. Figure 8c shows dependency of the 1 bar fiber volume fraction on the nanofibers interleave areal density for the second compression cycle. The

second cycle was chosen as a cycle giving a representative condition of the laminate layers; the reader is referred to [18] for more extensive discussion of this choice. The fiber volume fraction *VF* was calculated based on the laminate thickness per one ply t_1 as shown by Equation (1):

$$VF = \frac{m}{t_1 \rho} \tag{1}$$

where *m* is the areal density of the fabric ply, ρ is the carbon fiber density. As it is seen from Figure 8c, up to the interleave areal density of 10 g/m² per fabric layer the fiber volume fraction for a four-ply laminate (this is a practically important case) stays over 50%, with the fiber volume fraction of the laminate without nanofibers being 53%. Interleave areal density up to 10 g/m² can be considered as a practically admissible values. The dependency of *VF* on the interleave areal density is almost linear. It is remarkable that the nesting intensity defined by Equation (2), i.e., the ratio:

$$k = \frac{t_1(1) - t_1(4)}{t_1(1)} \tag{2}$$

where $t_1(N)$ is thickness of one ply in an *N*-plies laminate, stays the same, $k \cong 0.12$ with increase of the interleave areal density. The fabric layers 'feel' the surface relief of one another in spite of the presence of nanofibers between them. This may point to penetration of the nanofibers inside the fabric plies, which will be supported by the observations in the next sub-section.

4.3. Nanofibers veil thickness and the added thickness of nanofibers interleave

Figure 9 compares nanofibers 1 bar veil thickness, which was reported in Section 4.1, with the added thickness of nanofibers interleave, calculated based on the measurements of the laminate thickness reported in Section 4.2. The latter for a given compaction pressure (1 bar) is calculated as shown by Equation (3):

$$t_{\text{CNF}} = t_1^{1-\text{NF}} - t_1^1 \tag{3}$$

where t_1^1 and $t_1^{1-\text{NF}}$ are thicknesses per one ply of a laminate with and without nanofiber interleaves at the same compaction pressure. As it is seen from Figure 9, the values of $t_{\text{nanofibers}}$ in laminates and even in compression of one ply of the fabric with a veil
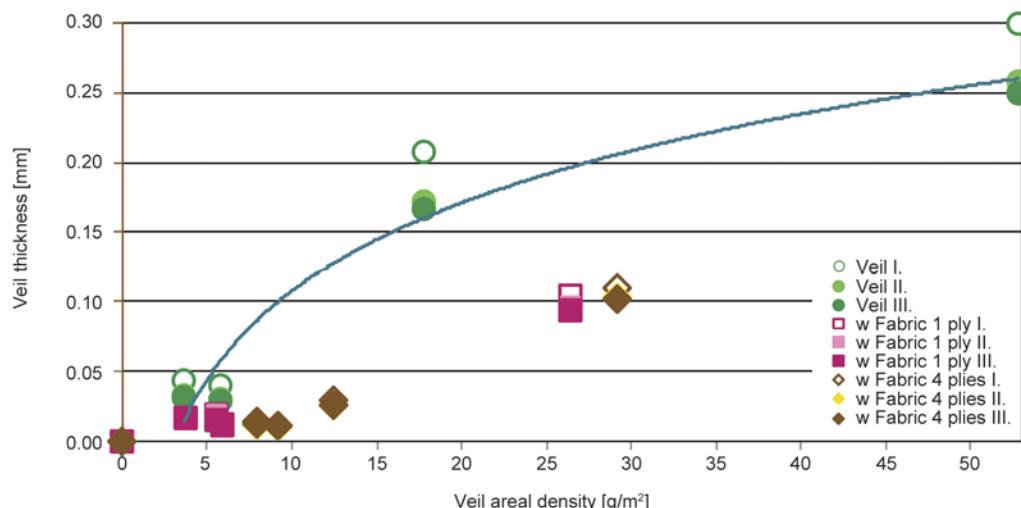
Figure 9. 1 bar veil thickness (average values) as a function of the veil areal density, for the veil itself and veils inside inter-leaved fabric laminates

on its surface are much smaller that free nanofibers veil thickness for the same veil areal density and the same applied pressure of 1 bar. The nanofibers veil thickness is reduced roughly twice.

A possible interpretation of this fact is that nanofibers penetrate inside the fabric during compaction, which is supported by the measurements of the nesting effect discussed above. This suspected interpenetration of nanofibers inside fabric layers can serve in advantage for increasing delamination resistance, potentially increasing the bridging effect of the inter-leave by their stronger interaction with fibers in the yarns – a subject worth investigating in future work.

5. Conclusions

Nanofiber interleaves in woven fabric laminates decrease compressibility of the laminate, increasing the laminate thickness for a given pressure and correspondingly decreasing fiber volume fraction in the consolidated laminate. The fiber volume fraction decreases almost linearly with the increase of the nanofibers areal density. However, up to areal density of the interleaves of 10 g/m^2 the decrease of the fiber volume fraction is below 3% and is practically acceptable.

The thickness of the nanofibers interlayers inside a woven laminate at a given pressure is twice smaller, than the thickness of CNT veils with the same areal density and under the same compacting pressure. This fact points to strong interference between the interleaves and the carbon reinforcement, which can lead to effective toughness improvement of the composite.

References
[1] Jing X., Mi H-Y., Salick M. R., Cordie T. M., Peng X-F., Turng L-S.: Electrospinning thermoplastic polyurethane/graphene oxide scaffolds for small diameter vascular graft applications. Materials Science and Engineering: C, **49**, 40–50 (2015).
DOI: 10.1016/j.msec.2014.12.060

[2] Erben J., Pilarova K., Sanetrnik F., Chvojka J., Jencova V., Blazkova L., Havlicek J., Novak O., Mikes P., Prosecka E., Lukas D., Kostakova E. K.: The combination of meltblown and electrospinning for bone tissue engineering. Materials Letters, **143**, 172–176 (2015).
DOI: 10.1016/j.matlet.2014.12.100

[3] Braghirolli D. I., Steffens D., Pranke P.: Electrospinning for regenerative medicine: A review of the main topics. Drug Discovery Today, **19**, 743–753 (2014).
DOI: 10.1016/j.drudis.2014.03.024

[4] Nagy Zs. K., Balogh A., Vajna B., Farkas A., Pátyi G., Kramarics Á., Marosi Gy.: Comparison of electrospun and extruded Soluplus®-based solid dosage forms of improved dissolution. Journal of Pharmaceutical Sciences, **101**, 322–332 (2012).
DOI: 10.1002/jps.22731

[5] Balogh A., Drávavölgyi G., Faragó K., Farkas A., Vigh T., Sóti P. L., Wagner I., Madarász J., Pataki H., Marosi Gy., Nagy Zs. K.: Plasticized drug-loaded melt electrospun polymer mats: Characterization, thermal degradation, and release kinetics. Journal of Pharmaceutical Sciences, **103**, 1278–1287 (2014).
DOI: 10.1002/jps.23904

[6] Orriach-Fernández J. F., Medina-Castillo A. L., Díaz-Gómez J. E., Muñoz de la Peña A., Fernández-Sánchez J. F., Fernández-Gutiérrez A.: A sensing microfibre mat produced by electrospinning for the turn-on luminescence determination of Hg^{2+} in water samples. Sensors and Actuators B: Chemical, **195**, 8–14 (2014).
DOI: 10.1016/j.snb.2014.01.010

[7] Ahmed F. E., Lalia B. S., Hashaikeh R.: A review on electrospinning for membrane fabrication: Challenges and applications. Desalination, **356**, 15–30 (2015).
DOI: 10.1016/j.desal.2014.09.033

[8] Carroll T., Booker N. A., Meier-Haack J.: Polyelectrolyte-grafted microfiltration membranes to control fouling by natural organic matter in drinking water. Journal of Membrane Science, **203**, 3–13 (2002).
DOI: 10.1016/S0376-7388(01)00701-3

[9] Sang Y., Gu Q., Sun T., Li F., Liang C.: Filtration by a novel nanofiber membrane and alumina adsorption to remove copper(II) from groundwater. Journal of Hazardous Materials, **153**, 860–866 (2008).
DOI: 10.1016/j.jhazmat.2007.09.035

[10] Huang Z-M., Zhang Y-Z., Kotaki M., Ramakrishna S.: A review on polymer nanofibers by electrospinning and their applications in nanocomposites. Composites Science and Technology, **63**, 2223–2253 (2003).
DOI: 10.1016/S0266-3538(03)00178-7

[11] Andrady A. L.: Science and technology of polymer nanofibers. Wiley, New Jersey (2008).

[12] Dzenis Y. A., Reneker D. H.: Delamination resistant composites prepared by small diameter fiber reinforcement at ply interfaces. U.S. Patent 6265333, USA (2001).

[13] Kelkar A. D., Mohan R., Bolick R., Shendokar S.: Effect of nanoparticles and nanofibers on Mode I fracture toughness of fiber glass reinforced polymeric matrix composites. Materials Science and Engineering: B, **168**, 85–89 (2010).
DOI: 10.1016/j.mseb.2010.01.015

[14] Liu L., Huang Z-M., He C. L., Han X. J.: Mechanical performance of laminated composites incorporated with nanofibrous membranes. Materials Science and Engineering: A, **435–436**, 309–317 (2006).
DOI: 10.1016/j.msea.2006.07.064

[15] Zhang J., Lin T., Wang X.: Electrospun nanofibre toughened carbon/epoxy composites: Effects of polyetherketone cardo (PEK-C) nanofibre diameter and interlayer thickness. Composites Science and Technology, **70**, 1660–1666 (2010).
DOI: 10.1016/j.compscitech.2010.06.019

[16] Palazzetti R., Yan X., Zucchelli A.: Influence of geometrical features of electrospun nylon 6,6 interleave on the CFRP laminates mechanical properties. Polymer Composites, **35**, 137–150 (2014).
DOI: 10.1002/pc.22643

[17] Palazzetti R., Zucchelli A., Trendafilova I.: The self-reinforcing effect of Nylon 6,6 nano-fibres on CFRP laminates subjected to low velocity impact. Composite Structures, **106**, 661–671 (2013).
DOI: 10.1016/j.compstruct.2013.07.021

[18] Molnár K., Kostáková E., Mészáros L.: The effect of needleless electrospun nanofibrous interleaves on mechanical properties of carbon fabrics/epoxy laminates. Express Polymer Letters, **8**, 62–72 (2014).
DOI: 10.3144/expresspolymlett.2014.8

[19] Sorrentino L., Bellini C.: Compaction influence on spring-in of thin composite parts: Experimental and numerical results. Journal of Composite Materials, **49**, 2149–2158 (2014).
DOI: 10.1177/0021998314542362

[20] Ersoy N., Garstka T., Potter K., Wisnom M. R., Porter D., Stringer G.: Modelling of the spring-in phenomenon in curved parts made of a thermosetting composite. Composites Part A: Applied Science and Manufacturing, **41**, 410–418 (2010).
DOI: 10.1016/j.compositesa.2009.11.008

[21] Lomov S. V., Gorbatikh L., Houlle M., Kotanjac Z., Koissin V., Vallons K., Verpoest I.: Compression resistance and hysteresis of carbon fibre tows with grown carbon nanotubes/nanofibres. Composites Science and Technology, **71**, 1746–1753 (2011).
DOI: 10.1016/j.compscitech.2011.08.007

[22] Lomov S. V., Gorbatikh L., Kotanjac Z., Koissin V., Houlle M., Rochez O., Karahan M., Mezzo L., Verpoest I.: Compressibility of carbon woven fabric with carbon nanotubes grown on the fibres. Composites Science and Technology, **71**, 315–325 (2011).
DOI: 10.1016/j.compscitech.2010.11.024

[23] Lomov S. V., Wicks S., Gorbatikh L., Verpoest I., Wardle B. L.: Compressibility of nanofibre-grafted alumina fabric and yarns: Aligned carbon nanotube forests. Composites Science and Technology, **90**, 57–66 (2014).
DOI: 10.1016/j.compscitech.2013.10.017

[24] Sorrentino L., Bellini C.: Analysis of laminate thickness influence on compressibility behavior in a rift process. International Journal of Engineering and Technology, **6**, 1259–1267 (2014).

[25] Chen Z-R., Ye L.: A micromechanical compaction model for woven fabric preforms. Part II: Multilayer. Composites Science and Technology, **66**, 3263–3272 (2006).
DOI: 10.1016/j.compscitech.2005.07.010

[26] Lomov S. V., Gorbatikh L., Verpoest I.: A model for the compression of a random assembly of carbon nanotubes. Carbon, **49**, 2079–2091 (2011).
DOI: 10.1016/j.carbon.2011.01.043

[27] Lomov S. V., L. Gorbatikh V. I., Verpoest I.: Compression behaviour of a fibre bundle with grafted carbon nanotubes. Carbon, **49**, 4458–4465 (2011).
DOI: 10.1016/j.carbon.2011.06.044

[28] Carnaby G. A., Pan N.: Theory of the compression hysteresis of fibrous assemblies. Textile Research Journal, **59**, 275–284 (1989).
DOI: 10.1177/004051758905900505

[29] Komori T., Itoh M., Takaku A.: A model analysis of the compressibility of fiber assemblies. Textile Research Journal, **62**, 567–574 (1992).
DOI: 10.1177/004051759206201002

[30] Mikolajczyk T., Rabiej S., Szparaga G., Boguń M., Fraczek-Szczypta A., Błażewicz S.: Strength properties of polyacrylonitrile (PAN) fibres modified with carbon nanotubes with respect to their porous and supramolecular structure. Fibres and Textiles in Eastern Europe, **17**, 13–20 (2009).

[31] Svetnickienė V., Čiukas R.: Technical and classical yarns friction properties investigation. Mechanika, **60**, 54–58 (2006).

[32] Bhushan B., Ling X., Jungen A., Hierold C.: Adhesion and friction of a multiwalled carbon nanotube sliding against single-walled carbon nanotube. Physical Review B, **77**, 165428/1–165428/12 (2008).
DOI: 10.1103/PhysRevB.77.165428

[33] Falvo M. R., Taylor R. M., Helser A., Chi V., Brooks F. P., Washburn S., Superfine R.: Nanometre-scale rolling and sliding of carbon nanotubes. Nature, **397**, 236–238 (1999).
DOI: 10.1038/16662

[34] Molnár K., Nagy Zs. K., Marosi Gy., Mészáros L.: Electrospinning spinneret and modified electrospinning method for producing nanofibers in productive ways. Hungarian patent P1200677, Hungary (2012).

Synthetic routes to degradable copolymers deriving from the biosynthesized polyhydroxyalkanoates: A mini review

Y. Ke[1], X. Y. Zhang[1], S. Ramakrishna[2], L. M. He[1], G. Wu[3]*

[1]Department of Biomedical Engineering, Key Laboratory of Biomaterials of Guangdong Higher Education Institutes, College of Life Science and Technology, Jinan University, 510632 Guangzhou, China
[2]Guangdong-Hongkong-Macau Institute of CNS Regeneration (GHMICR), Jinan University, 510632 Guangzhou, China
[3]Biomaterial Research Institute, School of Materials Science and Engineering, South China University of Technology, 510641 Guangzhou, China

Abstract. Polyhydroxyalkanoates are a family of natural polyesters being produced as intracellular carbon and energy reserves by a wide variety of microorganisms. They have developed rapidly in both research and development efforts globally in the last 15 years. Till now, over 100 different types of PHAs have been successfully biosynthesized using both genetic engineering and fermentation techniques. Their unique biodegradable, biocompatible and thermoplastic characteristics make PHAs promising candidates for the commodity and biomedical applications. This review focused on the chemical synthesis of the derivatives of the biosynthesized PHAs.

Keywords: *polymer synthesis, biopolymers, biodegradable polymers, biocompatible polymers*

1. Introduction

Hydroxyalkanoates (PHAs) are a family of polyesters that accumulate as carbon/energy or reducing-power storage. Till now, over 100 different types of PHA have been successfully biosynthesized using both genetic engineering and fermentation techniques [1–4]. Their unique biodegradable, biocompatible and thermoplastic characteristics make PHAs promising candidates for commodity applications, including recyclable packing materials, kitchen films, diapers, sanitary napkins. Recently, much interest is focused on the biomedical applications as surgical suture and swabs, wound dressings, vascular graft, blood vessel, and scaffold for new tissue in growth [5–7].

Poly(3-hydroxybutyrate) (P3HB) is the most common short-chain-length PHA, first discovered in 1925 by Lemoigne who described it as a lipid inclu-

sion in the bacterium *Bacillus megaterium* [8]. Several inherent deficiencies of PHB have limited its medical applications, including the brittleness due to the high crystallinity and the narrow thermal processing window because of the thermal instability. PHA copolyesters containing, besides 3-hydroxybutyrate (3HB, Figure 1a), 4-hydroxybutyrate (4HB, Figure 1b) [9–11], 3-hydroxyvalerate (3HV, Figure 1c) [12–16], 4-hydroxyvalerate (4HV, Figure 1d) [17–18], hydroxypropionate (HP, Figure 1e) [19–20], hydroxyhexanoate (HHx, Figure 1f) [21–23], and hydroxyoctanoate (HO, Figure 1g) [24] units can be produced by different microorganisms. Varying the copolymer composition affords obtaining copolyesters with adjustable mechanical and processing properties exceeding those of the P3HB homopolymer. Terpolyesters poly(3-hydroxybutyrate-*co*-3-hydroxyvalerate-*co*-4-hydroxybutyrate)
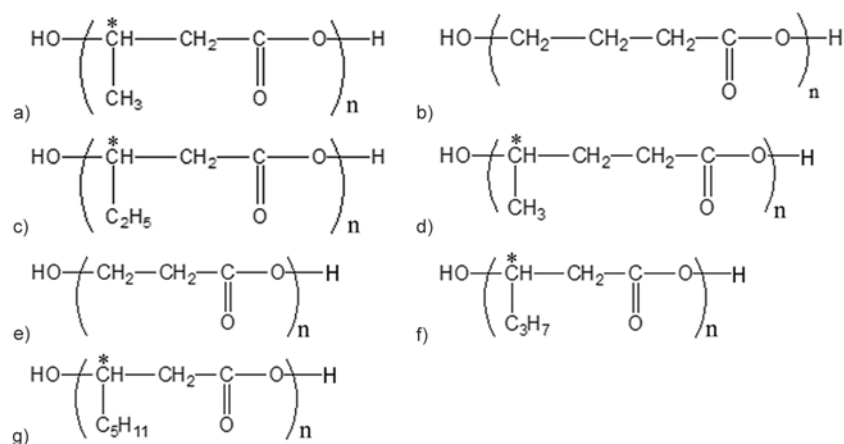
Figure 1. Monomer units of the main PHAs: (a) P3HB; (b) P4HB; (c) P3HV; (d) P4HV; (e) PHP; (f) PHHx; (g) PHO, letter (*n*) and asterisks (*) represent the number of repeat units and the chiral centers, respectively

(P3HB3HV4HB) [25–27], poly(3-hydroxybutyrate-*co*-3-hydroxyvalerate-*co*-3-hydroxyhexanoate) (P3HB3HVHHx) [28, 29] and poly(3-hydroxybutyrate-*co*-4-hydroxybutyrate-*co*-3-hydroxyhexanoate) (P3HB4HBHHx) [30, 31] have be synthesized by changing the feedstock and microorganisms.

Natural blocky-structured PHAs have been successfully synthesized *in vivo* by microorganisms and *in vitro*. Diblock copolymer PHB-*b*-PHHx was produced by a recombinant *Pseudomonas putida* KT2442 with its *β*-oxidation cycle deleted to its maximum [32]. P3HB-*b*-P3HP was biosynthesized *via* the engineered *Escherichia coli* strain from two parallel synthetic pathways that were modulated by independent regulatory systems to produce the 3HB and 3HP monomers, respectively [33]. PHA synthase from *Ralstonia eutropha* (PhaCRe) was engineered to acquire an unusual lactate (LA)-polymerizing activity, which incorporated LA units into the P3HB backbone with a block sequence *in vivo* using recombinant *Escherichia coli* LS5218 [34]. The mutated PhaC1SG from a thermo-tolerant bacterium (*Pseudomonas sp.* SG4502) showed high thermal stability in synthesizing P(LA-*co*-3HB) in an *in vitro* reaction system by sequential feeding of the corresponding two substrates [35]. Fermentation of *Alcaligenes eutrophus* in a culture containing polyethylene glycol (PEG) or polysaccharide has produced a hydroxyterminated block copolymer consisting of PHA [36, 37].

Biosynthesis provides a versatile way to produce the copolymers with desired sequence patterns, random or block. However, PHAs still suffer from some disadvantages: the deficiency of the commercialized PHAs, high cost compared to that of petroleum-based polyesters, and the difficulty in controlling the structure and molecular mass, which would be solved to some extent *via* synthesizing copolymer or functionalizing PHAs chemically. This paper summarized the chemical synthesis of the PHAs derivatives.

2. PHAs with unsaturated side chains and their derivatives

The introduction of other functional groups in PHAs has also been achieved *via* the biosynthesis route. Poly(3-hydroxy undecenoate) (PHU, Figure 2), being obtained from *P. oleovorans* with a mixture of sodium octanoate and 10-undecenoic acid [38], is a novel and multifunctional type of PHA, which has attracted much attention owing to its unsaturated side chains. These vinyl groups can be oxidized to carboxylic acid using osmium tetraoxide/oxone or acidic potassium permanganate treatment [39, 40], or converted to alcohol (nearly 100% hydroxylation) using 9-borobicyclononane [41]. The partially hydroxylated (50~60%) PHU being treated with potassium permanganate at 20°C was completely soluble in polar solvents (80/20 acetone/water, methanol or dimethyl sulfoxide), indicating a considerably enhanced
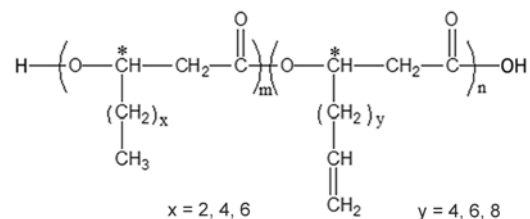

Figure 2. Monomer unit of PHU, letters (*n*, *m*) and asterisks (*) represent the number of repeat units and the chiral centers, respectively

hydrophilicity [42]. Epoxides-terminated side chains being converted from the vinyl terminal of PHU has been reported to be modified with diethanolamine to obtain a cationic PHA with pendant amine side groups [43, 44]. When exposed to air at room temperature for 40 days, the unsaturated copolyester formed a highly flexible and biocompatible elastomer [45].

The double bonds of the unsaturated PHAs can be homo-/copolymerized *via* free radical mechanisms to graft poly(methyl methacrylate) or by UV irradiating to graft PEG in the presence of benzoyl peroxide [46] and benzoyl peroxide [24], respectively. The halogenated PHU could be transformed to macro reversible addition-fragmentation chain transfer agents *via* the substitution reaction with potassium ethyl xanthate, which further initiated polymerization of *N*-isopropylacryl amide to obtain thermo-responsive and amphiphilic brush copolymers [47, 48].

Though the side chains of the unsaturated PHAs can be easily grafted to add chemical groups or cross-link with other polymer chains, it has been very difficult to obtain structurally controllable block-PHAs. A *β*-oxidation deleted *Pseudomonas entomophila* was used to biosynthesize block copolymers of 3-hydroxydodecanoate (3HDD) and 3-hydroxy-9-decenoate (3H9D), which was produced by feeding dodecanoic acid firstly to form a P3HDD block followed by adding 9-decenol to form a P3H9D block [49]. This method allows further chemical modification to widen PHA diversity, promising to control the PHA functionality to meet various requirements.

3. PHAs copolymer *via* an oligomer-first method

A two-step reaction is applied in this route: PHAs are first functionalized with termini other than the native hydroxyl and carboxyl groups to produce PHAs oligomers, and these telechelic chains of PHAs have been used for the chain-extension reaction to synthesize new copolymers. PHAs oligomers could be obtained *via* various thermal or chemical methods with the concomitant partial depolymerization in order to reduce solution viscosities and facilitate subsequent modification.

Pyrolysis is an easy method to produce the functionalized PHA macromonomers. At the moderately low temperature (170~200°C), PHB degraded into a well-defined oligomer containing one unsaturated end group, predominantly a trans-alkenyl end group,

as well as a carboxylic end group [50]. The dominant thermal degradation occurred *via* a random chain scission (*cis*-elimination) with a six-membered ring ester intermediate [51–54]. If 2,2′-bis(2-oxazoline) was introduced in the thermal degradation, a hydroxyl-terminated PHBV was achieved with an improved thermal stability [55].

Telechelic oligomers with hydroxyl groups are commonly produced *via* alcohololysis, a transesterification reaction of alkanediols and high molecular-weight PHAs. The chain length of the macrodiols could be easily controlled by the alcoholysis time. When a catalyst (dibutyltin dilaurate) has been applied along with diethylene glycol, a yield of the telechelic hydroxylated PHB (PHB-diol) has been reported to be 80% [56]. Acid (hydrochloric acid or sulfuric acid) catalyzed the methanolysis to produce PHB and PHBV oligomers, having a free secondary hydroxyl as well as a methyl ester protected carboxylic acid for the two respective chain ends [57, 58]. Špitalský *et al.* [59] and Akita *et al.* [60] have studied the alcoholysis of PHB with two types of alcohol (ethylene glycol or glycerol) in the presence of *p*-toluene sulfonic acid, and found that the controlled degradation of PHB proceeded by random chain scission, and the molecular mass decreased by almost two orders of magnitude. The alcoholysis with ethylene glycol was significantly faster than that with glycerol. Different from the thermal degradation, the crystallinity did not change significantly during the alcoholysis.

Abiotic hydrolysis of PHAs is a relatively slow process under mild conditions [61, 62]. Based on the mechanism of the heterogeneous hydrolysis, the scission of PHB chains occurs at the surfaces and interfaces of lamellar crystals. In acidic or alkaline solutions, PHB can be hydrolyzed *via* the random scission of the ester bonds, forming insoluble/soluble oligomers or monomeric acids [63]. The unsaturated end group was formed by dehydration of the chain ends by *β*-elimination after ester hydrolysis, different from the mechanism of thermal decomposition [64].

Other PHAs oligomers, such as PHB macrodiols with a hydroxyl group and a double bond at different chain ends [65], PHB-amine conjugate containing hydrolysable imine bond [66], chlorination of PHAs (PHB or PHO) and their corresponding quaternary ammonium salts, sodium sulfate salts, and phenyl derivatives [67], have also been produced by

various chemical methods. These PHAs oligomers could be used for building the block (diblock, triblock, or star block), graft, or even brush type graft copolymers of PHAs *via* different mechanism, mainly coupling reaction and macroinitiating reaction, to explore the suitable chemical and physical properties, processability and biocompatibility.

3.1. Coupling reaction

Coupling reaction is a general and powerful strategy for preparing PHAs derivatives. For example, PHB oligomers were directly coupled with amino groups of chitosan to synthesize graft copolymers [68, 69], though the yield was rather low. The indirect coupling reaction usually uses an agent between the PHAs macromonomer and the second component. Acyl chloride, 1,3-*N,N*-dicyclohexylcarbodiimide (DCC)/4-(dimethylamino) pyridine (DMAP), and diisocyanate are three main coupling agents that

have been employed to synthesize PHAs derivatives (Table 1). It should be noted that these impurities (coupling agents) would be left inside the copolymers, so that the coupling reaction is often used for systems without other options.

3.1.1. Acyl chloride

Coupling mechanism using acyl chloride as a bridge to link the hydroxyl-terminated PHAs macromonomers with other dihydroxyl-teminated oligomers is a direct method to produce block copolymer. For example, a PHO-diol and a PHB-diol were chosen to produce block copolyesters with terephthaloyl chloride (Figure 3), where a polycondensation reaction occurred between COCl and OH groups. Since water can inhibit the polymerization by reacting with TeCl to give the corresponding acid, the reaction must be carried out under an anhydrous condition and a nitrogen atmosphere [70].

Table 1. Coupling reaction for the synthesis of PHAs derivatives

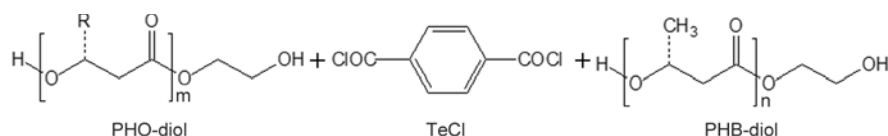| Coupling agent	PHAs macromonomers	Other components	Copolymer	References
Terephthaloyl chloride	PHB-diol	PHO-diol	Block	[70]
1,3-*N,N*-dicyclohexylcarbodiimide 4-(dimethylamino)pyridine	PHB-diol	Methoxy-PEG-monocarboxylic acid	Block	[71, 72]
	PHB-diol	Multifunctional cores (trimethyol propane, pentaerythritol or dipentaerthritol), *ε*-caprolactone	Star block	[73]
	PHB-COOH (*via* thermal degradation)	Hydroxyethyl methacrylate	Comb graft	[74]
1,6-hexamethylene diisocyanate	PHB-diol	PCL-diol	Block	[78]
	PHB-diol	PEG	Block	[82, 85–87]
	PHB-diol	PCL-PEG-PCL triblock copolydiol	Block	[88]
	PHB-diol	Poly(propylene glycol), PEG	Block	[92, 93]
	PHB-diol	Poly(butylene glycol adipate)-diol *OR* Poly(diethylene glycol adipate)-diol	Block	[79–81]
	P3HB4HB-diol	PHBHHx-diol	Block	[75]
	P3HB4HB-diol	PHHxHO-diol	Block	[76]
	P3HB4HB-diol	P3HB4HB-diol with different 4HB contents and segment lengths	Block	[77]
	P3HB4HB-diol	PEG	Block	[83]
	PHBHHx-diol	PEG	Block	[84]
Toluene diisocyanate	PHB-diol	PCL-diol	Block	[94]
2,2,4-Trimethylhexamethylene diisocyanate	PHBV-diol	Poly[glycolide-co-(*ε*-caprolactone)]-diol Poly[(L-lactide)-co-(*ε*-caprolactone)]-diol	Block	[95]
	PHBV-diol		Block	[96]
	PHB-diol	PCL-diol	Block	[97]
L-Lysine methyl ester diisocyanate	PHB-diol	PHO-diol	Block	[98]
	PHBV-diol		Block	[96]
	PHB-diol	PCL-diol	Block	[97]
PEG-diisocyanates	P3HB4HB-diol	–	Alternative block	[99]

Figure 3. Components for the synthesis of PHO-*b*-PHB copolymer using terephthaloyl chloride as the coupling agent

3.1.2. DCC/DMAP

DCC/DMAP system induces the esterification reaction between PHAs macromonomers and other components. Li and coworkers [71, 72] have synthesized a PEO-*b*-PHB-*b*-PEO triblock copolymers from PHB-diol and methoxy-PEG-monocarboxylic acid by esterification reaction for drug delivery applications. PEO and PHB blocks formed separate crystalline phases in the copolymers: the crystallinity of PHB block increased, while that of the PEO block decreased. The amphiphilic copolymer could self-aggregate into micelles in the aqueous medium, being composed of the hydrophobic PHB core and the hydrophilic PEO corona shell. Once coupled with multifunctional cores (trimethyol propane, pentaerythiritol or dipentaerthritol), the PHB-diol could initiate the ring opening polymerizations of *ε*-caprolactone (CL) to form star block copolymers with structural variation on arm numbers and lengths [73]. Methacrylic macromonomers of PHB *via* thermal degradation could copolymerize with hydroxyethyl methacrylate to yield a comb graft, containing 0.5~14 mol% of PHB blocks. However, the graft was controlled poorly with unpredictable molecular mass and broad polydispersity [74].

3.1.3. Diisocyanate

1,6-Hexamethylene diisocyanate is a common coupling agent to prepare PHAs elastomers whose segmented and domain structure can be easily controlled by a selection of the monomer units for building the segments, their relative proportions and the length of segments. P3HB4HB has been reported to couple with PHBHHx [75], PHHxHO [76], or only P3HB4HB with different 4HB contents and segment lengths [77] based on the dihydroxyl-teminated precursors by melting polymerization. Hydrophobic and biodegradable PCL (soft segment) has been designed to synthesize PCL-*b*-PHB by one-step solution polymerization. The block polymer was semicrystalline, having a PCL crystalline phase along with the PHB crystalline phase and the melting temperature within 126~148°C [78]. Poly (butylenes glycol adipate)-diol (PBA-diol) or poly (diethylene glycol adipate)-diol (PDEGA-diol) as soft segments was also coupled with PHB-diol. When PHB-diol was less than 50 wt%, PBA and PHB phases crystallized separately in PBA-*b*-PHB. However, only PHB segments crystallized in PHB-*b*-PDEGA. Both copolymers showed three-step decom-

position, being assigned to the thermal degradation of PHB hard blocks, PBA or PDEGA soft blocks, and the urethane linkage, respectively [79–81].

Hydrophilic PEG could function as the soft segment to synthesize block copolymers, along with PHB [82], P3HB4HB [83], or PHBHHx [84] segment (Figure 4/I). PHB and PEG segments formed separate crystalline phases with a lower crystallinity and a lower melting point than those of their corresponding pre-polymers, and a glass transition temperature between two pre-polymers. Young's modulus and the stress at break of the copolymers increased with increasing PHB segment length or PEG segment length, whereas the strain at break increased with increasing PEG segment length or decreasing PHB segment length [85, 86]. When fabricated into an electrospun fibrous scaffold, it can be coated with calcium minerals by simple incubation in simulated body fluid, showing a potential application for bone regeneration [87]. The multi-block based on PHB-diol and PCL-PEG-PCL triblock copolydiol by one step solution polymerization was a semicrystalline with two crystallizable PHB and PCL-PEG-PCL blocks. The melting temperature of PHB segments was ~40°C, less than that of neat PHB. Only one glass temperature was exhibited, which corresponded to PCL-PEG-PCL components [88].

Proper choice of the composition of the copolymers (input ratio of hard and soft segments) and the type of macrodiols allows the production of various materials that possess a wide range of thermal and mechanical properties, procesability, hydrophilicity and degradability [89]. It should be noted that small crystalline particles of short-chain PHB (PHB-P, M_n = 2300) released when the block copolymers degraded. Phagocytosis of PHB-P with an irregular shape (1~ 10 µm) at high concentrations (>10 µg/mL) was dose dependent and associated with cell damage in macrophages (J774), but not in mouse fibroblasts (3T3) [90]. Primary rat tibia osteoblasts were capable of phagocytosing PHB-P (diameter of 2~20 µm), and this process was accompanied at low PHB-P concentrations by dose- and time-dependent alteration of alkaline phospatase activity, but not of collagen type I or osteocalcin [91].

Coupling the second (PEG) and even the third component (polypropyleneglycol, PPG) provided the PHB-based copolymers with an unexpected and unique function. The amphiphilic and thermosensitive triblock underwent a sol-gel-sol transition as
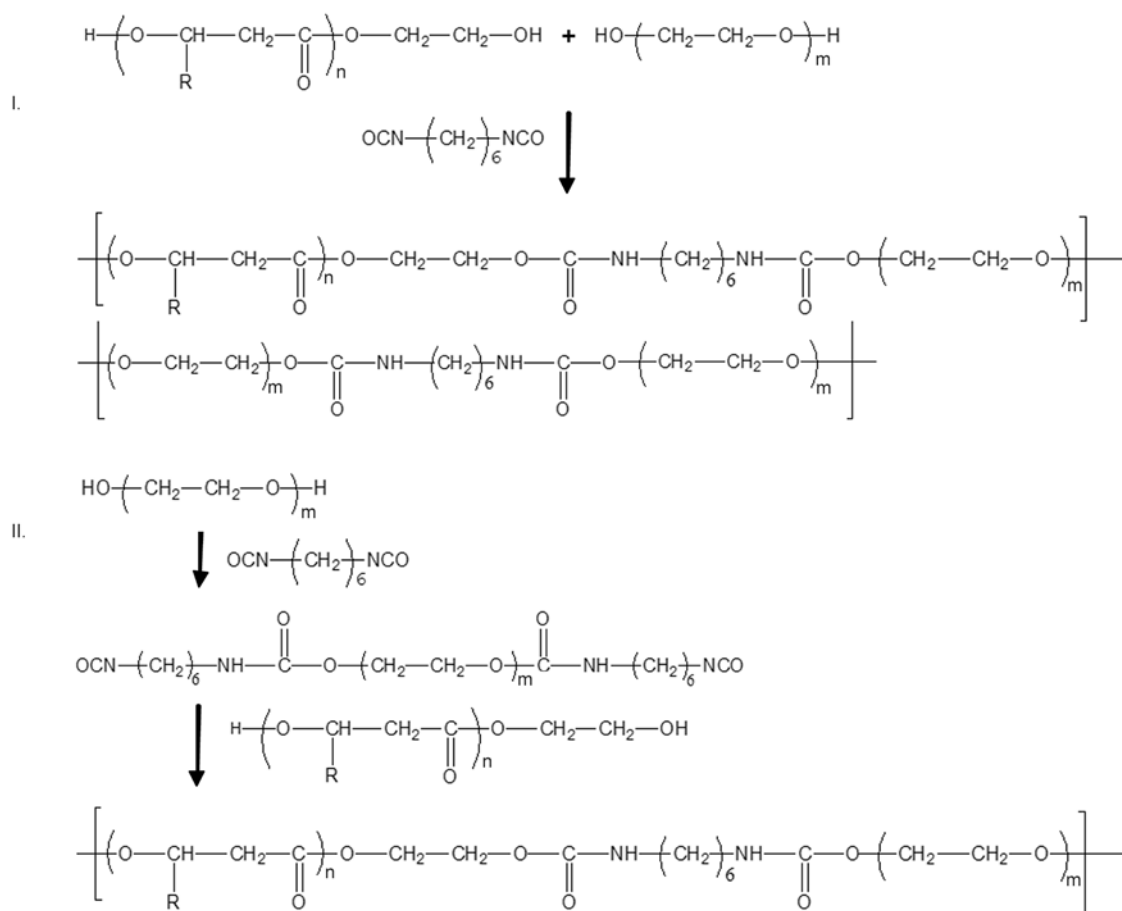
Figure 4. Scheme of the synthesis of the random block copolymer (I) and alternative block copolymer (II) based on PHAs-diol and PEG, R = CH₃, C₂H₅, C₃H₇, C₅H₁₁

the temperature increased from 4 to 80°C. It showed a very low critical gelation concentration ranging from 2 to 5 wt%, much lower than that of the commercial thermogelling PEG-PPG-PEG triblock copolymers (15~20 wt% or above). Moreover, non-biodegradable PEG-PPG-PEG triblock copolymers have been reported to show hyperlipidemia and high plasma level of cholesterol in rabbits and rats [92], and less cells (L929 mouse fibroblasts) attachment [93], suggesting that introducing a hydrophilic, biodegradable and biocompatible soft phase in the PHAs block copolymers is an effective way to design novel biomaterials.

Other diisocyanate, including toluene diisocyanate [94], 2,2,4-trimethylhexamethylene diisocyanate [95–97], and L-lysine methyl ester diisocyanate [96–98] have also been applied to synthesize block copolymer. The coupling reaction *via* diisocyanate must be carried out under anhydrous conditions and an argon or nitrogen atmosphere due to the moisture sensitivity of the coupling agent. More importantly, the above coupling approach lacks the block

selectivity and provides the copolymers with the blocks in a random manner, so that the properties of the copolymer were not able to be tuned finely. Pan *et al*. [99] have attempted to prepare a series of amphiphilic alternative block copolymers based on P3HB4HB-diol and PEG *via* the terminal coupling reaction of hydroxyl group of P3HB4HB-diol with isocyanate group of PEG-diisocyanates, so that one component can be fully characterized (Figure 4/II). This synthetic methodology provides a way to tailor the exact structure of the biomaterials.

3.2. Macro-initiating reaction

Macro-initiators can be used as precursors for the synthesis of block copolymers through radical and ionic polymerization. Arslan *et al*. [100] have suggested a two-step route to synthesize PHB-*b*-PMMA (where polymethylmethacrylate, PMMA) as follows: A PHB macroinitiator (PHB-MI), having hydroxyl groups at two ends of the polymer chain and an internal azo group, was obtained through the condensation reaction of PHB-diol with 4,4′-azobis(4-

cyanopentanoyl chloride). Through a redox free-radical polymerization of methyl methacrylate (MMA) with a PHB-MI/Ce(IV) redox system, a multiblock active copolymers with azo groups (PMMA-PHB-MI) were prepared, which was further used in the thermal polymerization of MMA to obtain the final block copolymer. However, it is difficult to produce copolymers with well-controlled molecular mass and low polydispersity in this way.

3.2.1. Ring opening polymerization

Ring opening polymerization (ROP) is a useful synthetic route to synthesize biomaterials (Table 2) with various controllable properties for medicinal and pharmaceutical applications [101, 102]. The oligo (3-hydroxybutyrate) conjugates with sorbic acid, benzoic acid and *p*-coumaric acid have been obtained *via* the anionic ring-opening oligomerization of racemic *β*-butyrolactone being initiated by sodium sorbate, sodium benzoate, and *p*-coumaric acid potassium salt, respectively [103, 104]. PHAs macroinitiators containing olefinic and carboxylic end groups were obtained by the controlled depolymerization of natural PHAs (PHB, PHBV or PHO), being catalyzed by KOH/18-crown-6 complex in a CHCl$_3$/H$_2$O system. These macroinitiators, having similar molecular mass (M_n = 3000) and a unimodal molecular mass distribution, were then used in anionic ROP of *β*-butyrolactone to obtain the respective diblock copolymers of natural origin PHA and a-PHB [105–107].

Macroinitiators of PHAs, PHB-O-AlEt$_2$ being produced from PHB-diol and AlEt$_3$, can initiate ROP of other monomers (*ε*-caprolactone and lactic acid) to produce PHB-PCL, PHB-D,L-PLA, and PHB-L-PLA diblock copolymers, respectively. These diblock copolymers may serve as emulsifiers for the respective blends of the homopolymers [58]. However, it is well accepted that aluminum ethyl cannot be used to synthesize degradable biomaterials due to the retention of aluminum *in vivo* and low catalytic efficiency.

Alkyl tin carboxylate is the most common catalyst for the synthesis of PLA and PCL because of the high catalytic activity. The triblock copolymers containing PHBV and PCL units were synthesized by using PHBV2000 as a macroinitiator to carry out ROP of *ε*-caprolactone in the presence of dibutyltin dilaurate at 130°C. It was found that the crystallization rate of PCL block increased gradually with the increase of PCL content, though both blocks crystallized more difficultly than the corresponding homopolymers [108]. Methyl-PHB oligomers containing hydroxyl and carboxyl end groups have been reported to initiate a controlled coordination insertion ROP of D,L-lactide and *ε*-caprolactone *via* the catalyst of stannous 2-ethylhexanoate, respectively (Figure 5). The triblock copolymers PHB-PLA-PCL showed potential applications as drug release carriers, or surface coatings on other biomedical devices [109]. It should be noted that the toxic nature of stannous ethylhexanoate is a big obstacle for its use
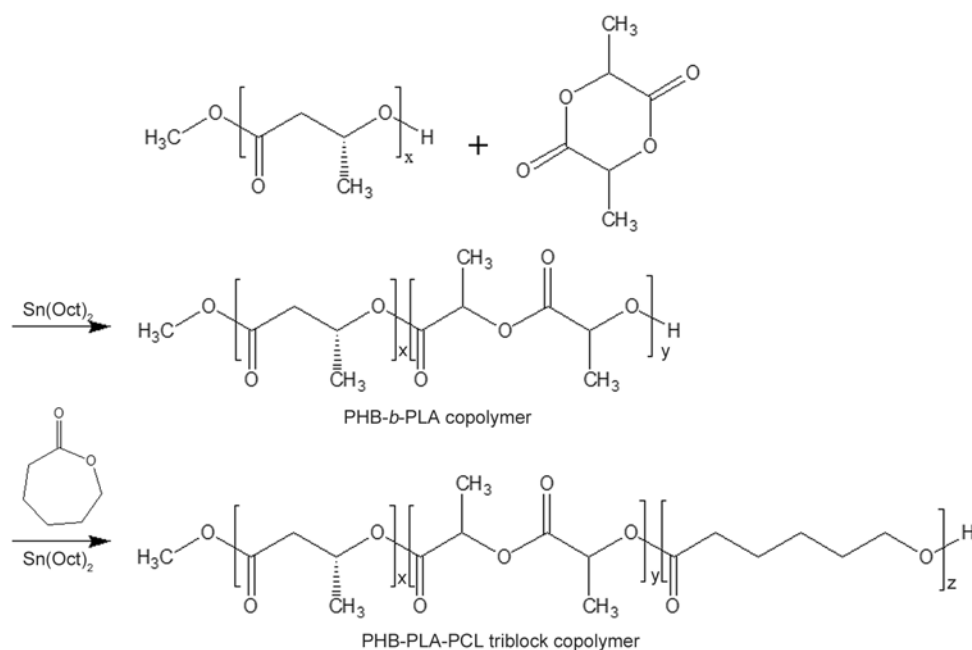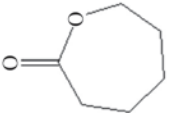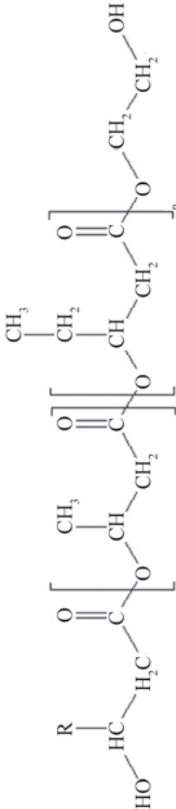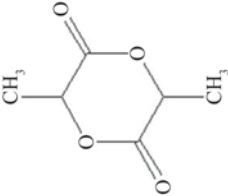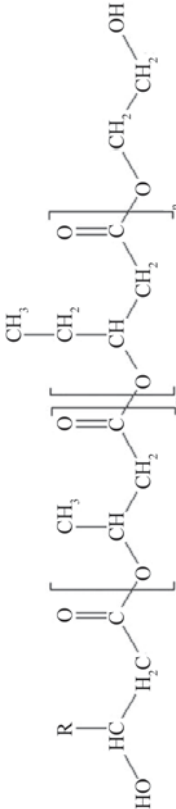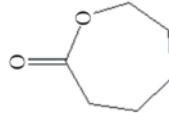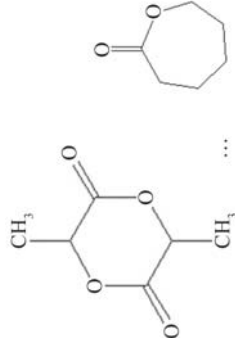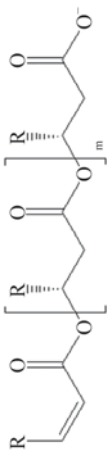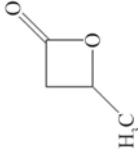

Figure 5. Scheme of the two-step synthesis of the PHB-PLA-PCL triblock copolymer through ring opening polymerization

Table 2. Synthesis of the PHAs-based block copolymers via ROP

Low-molecular PHAs	Monomers	Block copolymers	Mechanism	References
		PHB-PCL	Coordination-insertion ROP	[58]
		PHB-PLA	Coordination-insertion ROP	[108]
		PCL- PHBV-PCL	Coordination-insertion ROP	[109]
		PHB-PLA-PCL	Coordination-insertion ROP	
		PHA-(a-PHB) PHA:PHB, PHBV, PHO	Anionic ROP	[105–107]

in biomedical application, though it has been granted as a food additive by FDA. Another problem is the rather low rate of ROP. Therefore, catalysts or co-catalysts that enable the rate of polymerization and/or the applicability of the reactions to commercially viable systems to be increased would be the focus of ROP in the next few years.

3.2.2. Atom transfer radical polymerization

Atom transfer radical polymerization (ATRP) has been attracting much attention as a new route to synthesizing well-defined polymers [110, 111]. Halogenated PHAs as macroinitiators can be used in ATRP of vinyl monomers to obtain the block, graft, or brush type multi-graft copolymers. The starting dibromo-terminated PHB (Br-PHB-Br) macroinitiator (Figure 6/II) was usually obtained by the reaction of the terminal hydroxyl of PHB-diol (Figure 6/I) with 2-bromoisobutyryl bromide. The macroinitiator then initiated *N*-isopropylacrylamide in dioxane to form the triblock copolymer with PHB as the central hydrophobic block and PNIPAAm as the flanking block segment (Figure 6/III, 6a). The exciting potential for PNIPAAm-PHB-PNIPAAm lied in its

low critical micelle concentrations, the tunability of the biodegradability and the loading capacities by variation in its composition. The water-soluble copolymers formed core-corona-type micelle aggregates with the critical micelle concentrations of (1.5~41.1) mg/L and the partition coefficients of $(1.64~20.42) \cdot 10^5$. The length of PNIPAAm blocks on either side of the PHB block could be restricted to a molecular mass of <20 000 g/mol so as to allow the final degraded fragment to be easily excreted from the body *via* renal filtration. Moreover, the hydrophobicity of the micellar core could be controlled by adjusting the composition of the copolymer to tune the encapsulation efficiency of hydrophobic drugs [112].

The dibromo-terminated PHB macroinitiator induced the polymerization of 2-(dimethylamino)ethyl methacrylate (DMAEMA, Figure 6/III, 6b) and poly(tertbutyl acrylate) (Figure 6/III, 6c) either. The former amphiphilic PDMAEMA-PHB-PDMAEMA triblock copolymer showed lower toxicity and better gene transfection efficiency than polyethyleneimine or PDMAEMA homopolymers [113]. The latter presented a microphase-separated structure at higher
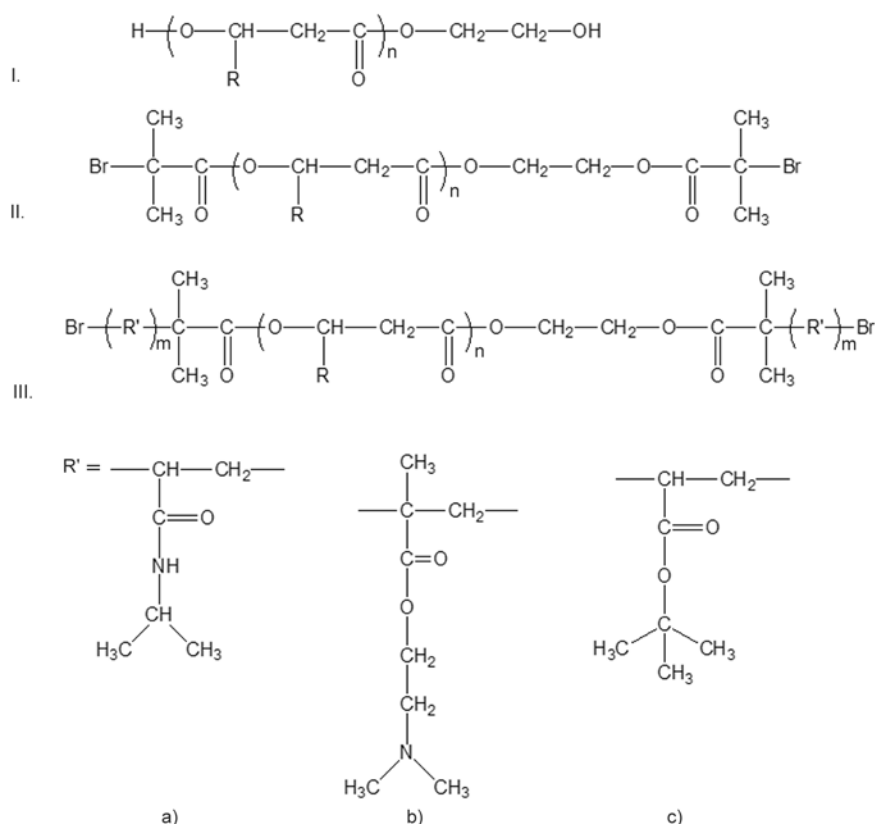

Figure 6. Synthesis of PHB based triblock copolymer by ATRP. I. PHB-diol; II. Br-PHB-Br; III. R′-PHB-R′ triblock copolymer: (a) poly(*N*-isopropylacrylamide); (b) poly(2-(dimethylamino)ethyl methacrylate); (c) poly(tertbutyl acrylate), R = CH_3, C_2H_5, C_3H_7, C_5H_{11}

PHB block content, along with better thermal stability than their respective homopolymers [114]. Graft copolymers based on PHB macromonomers can be synthesized in a one-step procedure *via* ATRP [115]. Vinyl monomers, methyl methacrylate (MMA) or styrene (S), have been initiated by PHA-Cl (macroinitiator) using cuprous chloride (CuCl)/2,2′-bipyridine complex (catalyst) to obtain PHA-*g*-PMMA or PHA-*g*-PS brush type graft copolymers with different numbers of side arms. Further, the multigraft brush copolymers PHO-*g*-PMMA (with more PMMA content) and PHO-*g*-(PMMA-*b*-PS) were synthesized *via* ATRP of MMA and S using PHO-*g*-PMMA-Cl as macroinitiator [116, 117]. A brush copolymer composed of the PHB chain and PEG brushes was designed as amphiphilic self-aggregating species with potential application in the healthcare field [118].

The graft copolymers *via* ATRP were of lower polydispersity (~1.2) than the ones by the conventional free radical polymerization (FRP, 1.6~2.1), and lower molecular mass (~20 000 for ATRP, 31800~84100 for FRP) [119]. Usually, ATRP is characterized by the well-controlled molecular mass and polydispersity of a polymer, which depends on fast initiation with respect to propagation at a low radical concentration and a fast dynamic equilibrium between the active and dormant radicals. Therefore, the rate of polymerization is rather slow, and the solvent polarity could significantly affect the equilibrium of the active and dormant species. The reaction should be performed under a nitrogen atmosphere and anhydrous conditions, because O_2 and water could be a hindrance to the polymerization. Another key problem is the ageing of macromolecules by the remaining transition metal complex.

4. Direct route to synthesizing PHAs derivatives

Theoratically, the simplest method to synthesize PHAs derivatives is to link the second component and PHAs directly through a coupling agent (Table 3), for example, PHB-*co*-PEG copolymer by toluene diisocyanate (coupling agent). Unexpectedly, the main product was the homopolymer PEG other than the copolymer owing to the limited hydroxyl on the macromolecular chains [120]. Active polymers containing peroxide groups 'in chain' have been reported as coupling agents to be grafted onto poly(hydroxyl nonanoate) at 80°C. But polystyrene or poly(methyl methacrylate) need to be treated first by using oligo(adipoyl-2,5-dimethylhexane-2,5-diyl peroxide) or oligo(dodecanedioyl peroxide) to obtain the active polymers [121–123].

Catalyzed transesterification is a green chemical method, accompanied with the pyrolysis of PHAs melt of high molecular mass. Increasing reaction temperature and/or reaction time are advantageous to the reaction. Through a transesterification reaction in the presence of 4-toluenesulfonic acid monohydrate, oligo(3HB-*co*-4HB) conjugate with (4-chloro-2-methylphenoxy)acetic acid was synthesized in one pot under an argon atmosphere. This conjugate could be used as biodegradable controlled-release systems of pesticides with potentially higher resistance to weather conditions in comparison to conventional forms of pesticides [124]. If a nucleophile (monomethoxy PEG, mPEG) empolyed in the trans-

Table 3. Direct route to synthesizing PHAs derivatives

| Second monomer/polymer	PHAs	Copolymer	Initiator/catalyst	Synthetic route	References
Acrylic acid	PHB PHBV	Graft	γ radiation	Free radical polymerization	[137]
Isoprene	PHB	Graft	γ radiation	Free radical polymerization	[136]
Maleic anhydride	PHB	Graft	Benzoyl peroxide	Free radical polymerization	[128–131]
		Graft	γ radiation	Free radical polymerization	[138]
Phenyl vinyl ketone	PHBV	Graft	Benzoyl peroxide	Free radical polymerization	[127]
Methyl methacrylate 2-Hydroxyethyl methacrylate	PHBPHBV	Graft	γ radiation	Free radical polymerization	[132, 133]
Methyl methacrylate	PHU	Graft	Benzoyl peroxide	Free radical polymerization	[46]
Monoacrylate PEG	PHU	Graft	Benzoyl peroxide	Free radical polymerization	[139]
Monomethoxy PEG	PHB	Diblock	Bis(2-ethylhexanoate) tin	Transesterification	[125]
N-isopropyl acryl amide	PHU-Br	Graft	–	Reversible addition-fragmentation chain transfer	[47]
PCL	PHB	Diblock	Stannous octoate	Transesterification	[126]
Styrene	PHBPHBV	Graft	γ radiation	Free radical polymerization	[134, 135]
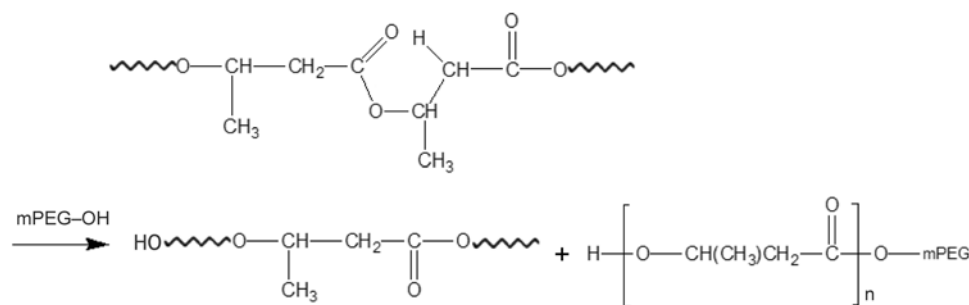
Figure 7. Scheme of the catalyzed transesterification reaction between PHB and mPEG

esterification under bis(2-ethylhexanoate) tin (catalyst), a PHB-*b*-mPEG copolymer was formed (Figure 7). The diblock copolymers were amphiphilic and could be self-assembled into sterically stabilized colloidal suspensions of PHB crystalline lamellae. This process was faster than the condensation reactions between mPEG and PHB oligomers, so that it is difficult to control the molecular mass of the PHB moiety. The yield was much higher and the contamination of products by the reagents like DCC and DMAP was avoided [125]. The transesterification of thermally unstable copolymer PHB-*b*-PCL could be conducted in liquid phase using stannous octoate as a catalyzer. The crystallization behavior of PHB-*b*-PCL copolyesters altered evidently with the increase in PCL content, though the crystalline structure of PHB remained unchanged [126].

Grafting polymerization using benzoyl peroxide as an initiator was often applied to introduce second component onto the PHAs chains, such as grafting polymerization of phenyl vinyl ketone onto PHBV under nitrogen atmosphere [127]. However, long graft chains may cause new environmental problems. Maleic anhydride showed good reactivity and controllability in free-radical polymerization so as to avoid long and undegradable graft chains *via* homopolymerization. The crystallization temperature of the graft decreased, and the thermal decomposition temperature increased by ~20°C compared with that of PHB homopolymer [128–131]. The drawback of the benzoyl peroxide-initiated grafting polymerization lies in the high reaction temperature, the large amount of solvents and high energy consumption, and the difficulties in purifying the product. The γ-radiation grafting polymerization could be done at the ambient temperature without any initiator. Vinyl monomers, such as methyl methacrylate or 2-hydroxyethyl methacrylate [132, 133],

styrene [134, 135], isoprene [136], acrylic acid [137], and maleic anhydride [138] have been reported to be grafted onto PHB or PHBV with a high yield (up to 80%).

5. Conclusions

New commercialized PHAs *via* biosynthesis route would burst with the development of research and industrial technique in the next few years, though time- and money-consuming procedures to bio-synthesize PHAs with specific functional groups are needed. The derivatives based on these novel PHAs will increase to meet the requirement for the final applications. The direct route to synthesizing the PHAs derivatives is limited owing to the low yield and purity, while the two-step route is advantageous to developing the structure- and property-controlled PHAs derivatives, especially when the living polymerization is applied in the second step. The challenge involves preparing the PHAs' oligomers with low polydispersity index.

The new macromolecular synthesis reaction and mechanism stimulates us to develop the block (diblock, triblock, or star block), graft, or even brush type graft copolymers of PHAs into promising candidates as biomaterials. The biocompatibility is still the most essential properties of the PHAs derivatives for the biomedical application. Therefore, the research relevant to the biocompatible components and initiator/stimulators will be an important key to developing the PHAs derivatives.

References

[1] Poirier Y., Somerville C., Schechtman L. A., Satkowski M. M., Noda I.: Synthesis of high-molecular-weight poly([r]-(-)-3-hydroxybutyrate) in transgenic *Arabidopsis thaliana* plant cells. International Journal of Biological Macromolecules, **17**, 7–12 (1995).
DOI: 10.1016/0141-8130(95)93511-U

[2] Steinbüchel A., Valentin H. E., Schönebaum A. J.: Application of recombinant gene technology for production of polyhydroxyalkanoic acids: Biosynthesis of poly(4-hydroxybutyric acid) homopolyester. Journal of Environmental Polymer Degradation, **2**, 67–74 (1994).
DOI: 10.1007/BF02074775

[3] Anderson A. J., Dawes E. A.: Occurrence metabolism metabolic role and industrial uses of bacterial polyhydroxyalkanoates. Microbiological Reviews, **54**, 450–472 (1991).

[4] Batcha A. F. M., Prasad D. M. R., Khan M. R., Abdullah H.: Biosynthesis of poly(3-hydroxybutyrate) (PHB) by *Cupriavidus necator* H16 from jatropha oil as carbon source. Bioprocess and Biosystems Engineering, **37**, 943–951 (2014).
DOI: 10.1007/s00449-013-1066-4

[5] Holmes P. A.: Applications of PHB – A microbially produced biodegradable thermoplastic. Physics in Technology, **16**, 32–36 (1985).
DOI: 10.1088/0305-4624/16/1/305

[6] Lee S. Y.: Plastic bacteria? Progress and prospects for polyhydroxyalkanoate production in bacteria. Trends in Biotechnology, **14**, 431–438 (1996).
DOI: 10.1016/0167-7799(96)10061-5

[7] Bugnicourt E., Cinelli P., Lazzeri A., Alvarez V.: Polyhydroxyalkanoate (PHA): Review of synthesis characteristics processing and potential applications in packaging. Express Polymer Letters, **8**, 791–808 (2014).
DOI: 10.3144/expresspolymlett.2014.82

[8] Lemoigne M.: Products of dehydration and polymerisation of hydroxybutyric acid (in French). Bulletin de la Société de Chimie Biologique, **8**, 770–782 (1926).

[9] Meszynska A., Pollet E., Odelius K., Hakkarainen M., Avérous L.: Effect of oligo-hydroxyalkanoates on poly (3-hydroxybutyrate-*co*-4-hydroxybutyrate)-based systems. Macromolecular Materials and Engineering, **300**, 661–666 (2015).
DOI: 10.1002/mame.201500026

[10] An J., Wang K., Chen S., Kong M., Teng Y., Wang L., Song C., Kong D., Wang S.: Biodegradability, cellular compatibility and cell infiltration of poly(3-hydroxybutyrate-*co*-4-hydroxybutyrate) in comparison with poly(ε-caprolactone) and poly(lactide-*co*-glycolide). Journal of Bioactive and Compatible Polymers, **30**, 209–221 (2015).
DOI: 10.1177/0883911515569006

[11] Sridhar V., Lee I., Chun H. H., Park H.: Graphene reinforced biodegradable poly(3-hydroxybutyrate-*co*-4-hydroxybutyrate) nano-composites. Express Polymer Letters, **7**, 320–328 (2013).
DOI: 10.3144/expresspolymlett.2013.29

[12] Doi Y., Kunnioka M., Nakamura Y., Soga K.: Biosynthesis of copolyesters in *Alcaligenes eutrophus* H16 from carbon-13 labeled acetate and propionate. Macromolecules, **20**, 2988–2991 (1987).
DOI: 10.1021/ma00178a006

[13] Kamiya N., Yamamoto Y., Inoue Y., Chujo R., Doi Y.: Microstructure of bacterially synthesized poly(3-hydroxybutyrate-*co*-3-hydroxyvalerate). Macromolecules, **22**, 1676–1682 (1989).
DOI: 10.1021/ma00194a030

[14] Mitomo H., Morishita N., Doi Y.: Composition range of crystal phase transition of isodimorphism in poly(3-hydroxybutyrate-*co*-3-hydroxyvalerate). Macromolecules, **26**, 5809–5811 (1993).
DOI: 10.1021/ma00073a041

[15] García I. L., López J. A., Dorado M. P., Kopsahelis N., Alexandri M., Papanikolaou S., Villar M. A., Koutinas A. A.: Evaluation of by-products from the biodiesel industry as fermentation feedstock for poly(3-hydroxybutyrate-*co*-3-hydroxyvalerate) production by *Cupriavidus necator*. Bioresource Technology, **130**, 16–22 (2013).
DOI: 10.1016/j.biortech.2012.11.088

[16] Phukon P., Saikia J. P., Konwar B. K.: Bio-plastic (P-3HB-*co*-3HV) from *Bacillus circulans* (MTCC 8167) and its biodegradation. Colloids and Surfaces B: Biointerfaces 92, 30-34 (2012).
DOI: 10.1016/j.colsurfb.2011.11.011

[17] Doi Y., Segawa M., Kunika M.: Biosynthesis and characterization of poly(3-hydroxybutyrate-*co*-4-hydroxybutyrate) in *Alcaligenes eutrophus*. International Journal of Biological Macromolecules, 12, 106-111 (1990).
DOI: 10.1016/0141-8130(90)90061-E

[18] Shi F., Ashby R. D., Gross R. A.: Fractionation and characterization of microbial polyesters containing 3-hydroxybutyrate and 4-hydroxybutyrate repeat units. Macromolecules, **30**, 2521–2523 (1997).
DOI: 10.1021/ma9617375

[19] Hiramitsu M., Doi Y.: Microbial synthesis and characterization of poly(3-hydroxybutyrate-*co*-3-hydroxypropionate). Polymer, **34**, 4782–4786 (1993).
DOI: 10.1016/0032-3861(93)90719-Q

[20] Shimamura E., Scandora M., Doi Y.: Microbial synthesis and characterization of poly(3-hydroxybutyrate-*co*-3-hydroxypropionate). Macromolecules, **27**, 4429–4435 (1994).
DOI: 10.1021/ma00094a003

[21] Shimamura E., Kasuya K., Kobayashi G., Shiotani T., Shima Y., Doi Y.: Physical properties and biodegradability of microbial poly(3-hydroxybutyrate-*co*-3-hydroxyhexanoate). Macromolecules, **27**, 878–880 (1994).
DOI: 10.1021/ma00081a041

[22] Doi Y., Kitamura S., Abe H.: Microbial synthesis and characterization of poly(3-hydroxybutyrate-*co*-3-hydroxyhexanoate). Macromolecules, **28**, 4822–4828 (1995).
DOI: 10.1021/ma00118a007

[23] Lee S. H., Oh D. H., Ahn W. S., Lee Y., Choi J-I., Lee S. Y.: Production of poly(3-hydroxubutyrate-*co*-3-hydroxyhexanoate) by high-cell-density cultivation of *Aeromonas hydrophila*. Biotechnology and Bioengineering, **67**, 240–244 (2000).
DOI: 10.1002/(SICI)1097-0290(20000120)67:2<240::AID-BIT14>3.0.CO;2-F

[24] Lee J., McCarthy S.: Biodegradable poly(lactic acid) blends with chemically modified polyhydroxyoctanoate through chain extension. Journal of Polymers and the Environment, **17**, 240–247 (2009).
DOI: 10.1007/s10924-009-0144-9

[25] Madden L. A., Anderson A. J., Asrar J., Berger P., Garrett P.: Production and characterization of poly(3-hydroxybutyrate-*co*-3-hydroxyvalerate-*co*-4-hydroxybutyrate) synthesized by *Ralstonia eutropha* in fed-batch cultures. Polymer, **41**, 3499–3505 (2000).
DOI: 10.1016/S0032-3861(99)00611-4

[26] Chanptateep S., Kulpreecha S.: Production and characterization of biodegradable terpolymer poly(3-hydroxybutyrate-*co*-3-hydroxyvalerate-*co*-4-hydroxybutyrate) by *Alcaligenes* sp. A-04. Journal of Bioscience and Bioengineering, **101**, 51–56 (2006).
DOI: 10.1263/jbb.101.51

[27] Hermann-Krauss C., Koller M., Muhr A., Fasl H., Stelzer F., Braunegg G.: Archaeal production of polyhydroxyalkanoate (PHA) *co*- and terpolyesters from biodiesel industry-derived by-products. Archaea, **2013**, 129268/1–129268/10 (2013).
DOI: 10.1155/2013/129268

[28] Park S. J., Ahn W. S., Green P. R., Lee S. Y.: Biosynthesis of poly(3-hydroxybutyrate-*co*-3-hydroxyvalerate-*co*-3-hydroxyhexanoate) by metabolically engineered *Escherichia coli* strains. Biotechnology and Bioengineering, **74**, 81–86 (2001).

[29] Zhao W., Chen G-Q.: Production and characterization of terpolyester poly(3-hydroxybutyrate-*co*-3-hydroxyvalerate-*co*-3-hydroxyhexanoate) by recombinant *Aeromonas hydrophila* 4AK4 harboring genes *phaAB*. Process Biochemistry, 42, 1342-1347 (2007).
DOI: 10.1016/j.procbio.2007.07.006

[30] Xie W. P., Chen G-Q.: Production and characterization of terpolyester poly(3-hydroxybutyrate-*co*-4-hydroxybutyrate-*co*-3-hydroxyhexanoate) by recombinant *Aeromonas hydrophila* 4AK4 harboring genes *phaPCJ*. Biochemical Engineering Journal, **38**, 384–389 (2008).
DOI: 10.1016/j.bej.2007.08.002

[31] Liu Q., Chen G-Q.: *In vitro* biocompatibility and degradation of terpolyester 3HB-*co*-4HB-*co*-3HHx, consisting of 3-hydroxybutyrate, 4-hydroxybutyrate and 3-hydroxyhexanoate. Journal of Biomaterials Science, Polymer Edition, **19**, 1521–1533 (2008).
DOI: 10.1163/156856208786140391

[32] Tripathi L., Wu L-P., Chen J., Chen G-Q.: Synthesis of diblock copolymer poly-3-hydroxybutyrate-*block*-poly-3-hydroxyhexanoate [PHB-*b*-PHHx] by a β-oxidation weakened *Pseudomonas putida* KT2442. Microbial Cell Factories, **11**, 44/1–44/11 (2012).
DOI: 10.1186/1475-2859-11-44

[33] Wang Q., Yang P., Xian M., Liu H., Cao Y., Yang Y., Zhao G.: Production of block copolymer poly(3-hydroxybutyrate)-*block*-poly(3-hydroxypropionate) with adjustable structure from an inexpensive carbon source. ACS Macro Letters, **2**, 996–1000 (2013).
DOI: 10.1021/mz400446g

[34] Ochi A., Matsumoto K., Ooba T., Sakai K., Tsuge T., Taguchi S.: Engineering of class I lactate-polymerizing polyhydroxyalkanoate synthases from *Ralstonia eutropha* that synthesize lactate-based polyester with a block nature. Applied Microbiology and Biotechnology, **97**, 3441–3447 (2013).
DOI: 10.1007/s00253-012-4231-9

[35] Tajima K., Han X., Satoh Y., Ishii A., Araki Y., Munekata M., Taguchi S.: *In vitro* synthesis of polyhydroxyalkanoate (PHA) incorporating lactate (LA) with a block sequence by using a newly engineered thermostable PHA synthase from *Pseudomonas* sp. SG4502 with acquired LA-polymerizing activity. Applied Microbiology and Biotechnology, **94**, 365–376 (2012).
DOI: 10.1007/s00253-011-3840-z

[36] Shi F. Y., Gross R. A., Rutherford D. R.: Microbial polyester synthesis: Effects of poly(ethylene glycol) on product composition, repeat unit sequence, and end group structure. Macromolecules, **29**, 10–17 (1996).
DOI: 10.1021/ma950707j

[37] Shi F., Ashby R., Gross R. A.: Use of poly(ethylene glycol)s to regulate poly(3-hydroxybutyrate) molecular weight during *Alcaligenes eutrophus* cultivations. Macromolecules, **29**, 7753–7758 (1996).
DOI: 10.1021/ma960805k

[38] Park W. H., Lenz R. W., Goodwin S.: Epoxidation of bacterial polyesters with unsaturated side chains. I. Production and epoxidation of polyesters from 10-undecenoic acid. Macromolecules, **31**, 1480–1486 (1998).
DOI: 10.1021/ma9714528

[39] Stigers D. J., Tew G. N.: Poly(3-hydroxyalkanoate)s functionalized with carboxylic acid groups in the side chain. Biomacromolecules, **4**, 193–195 (2003).
DOI: 10.1021/bm025728h

[40] Kurch N., Renard E., Brachet F., Robic D., Guerin P., Bourbouze R.: Poly(3-hydroxyoctanoate) containing pendant carboxylic groups for the preparation of nanoparticles aimed at drug transport and release. Polymer, **43**, 1095–1101 (2002).
DOI: 10.1016/S0032-3861(01)00692-9

[41] Eroğlu M. S., Hazer B., Ozturk T., Caykara T.: Hydroxylation of pendant vinyl groups of poly(3-hydroxy undec-10-enoate) in high yield. Journal of Applied Polymer Science, **97**, 2132–2139 (2005).
DOI: 10.1002/app.21943

[42] Lee M. Y., Park W. H., Lenz R. W.: Hydrophilic bacterial polyesters modified with pendant hydroxyl groups. Polymer, **41**, 1703–1709 (2000).
DOI: 10.1016/S0032-3861(99)00347-X

[43] Sparks J., Scholz C.: Synthesis and characterization of a cationic poly(β-hydroxyalkanoate). Biomacromolecules, **9**, 2091–2096 (2008).
DOI: 10.1021/bm8005616

[44] Bear M-M., Leboucher-Durand M-A., Langlois V., Lenz R. W., Goodwin S., Guerin P.: Bacterial poly-3-hydroxyalkenoates with epoxy groups in the side chains. Reactive and Functional Polymers, **34**, 65–77 (1997).
DOI: 10.1016/S1381-5148(97)00024-2

[45] Hazer D. B., Hazer B., Kaymaz F.: Synthesis of microbial elastomers based on soybean oily acids. Biocompatibility studies. Biomedical Materials, **4**, 035011/1–035011/9 (2009).
DOI: 10.1088/1748-6041/4/3/035011

[46] Ilter S., Hazer B., Borcakli M., Atici O.: Graft copolymerisation of methyl methacrylate onto a bacterial polyester containing unsaturated side chains. Macromolecular Chemistry and Physics, **202**, 2281–2286 (2001).
DOI: 10.1002/1521-3935(20010701)202:11<2281::AID-MACP2281>3.0.CO;2-9

[47] Toraman T., Hazer B.: Synthesis and characterization of the novel thermoresponsive conjugates based on poly (3-hydroxy alkanoates). Journal of Polymers and the Environment, **22**, 159–166 (2014).
DOI: 10.1007/s10924-014-0646-y

[48] Arkin A. H., Hazer B., Borcakli M.: Chlorination of poly (3-hydroxy alkanoates) containing unsaturated side chains. Macromolecules, **33**, 3219–3223 (2000).
DOI: 10.1021/ma991535j

[49] Li S., Cai L., Wu L., Zeng G., Chen J., Wu Q., Chen G-Q.: Microbial synthesis of functional homo-, random, and block polyhydroxyalkanoates by β-oxidation deleted *Pseudomonas entomophila*. Biomacromolecules, **15**, 2310–2319 (2014).
DOI: 10.1021/bm500669s

[50] Nguyen S., Yu G. E., Marchessault R. H.: Thermal degradation of poly(3-hydroxyalkanoates): Preparation of well-defined oligomers. Biomacromolecules, **3**, 219–224 (2002).
DOI: 10.1021/bm0156274

[51] Kim J. K., Doi Y., Abe H.: Effects of residual metal compounds and chain-end structure on thermal degradation of poly(3-hydroxybutyric acid). Polymer Degradation and Stability, **91**, 769–777 (2006).
DOI: 10.1016/j.polymdegradstab.2005.06.004

[52] Lehrle R. S., Williams R. J.: Thermal degradation of bacterial poly(hydroxybutyric acid): Mechanisms from the dependence of pyrolysis yields on sample thickness. Macromolecules, **27**, 3782–3789 (1994).
DOI: 10.1021/ma00092a017

[53] Aoyagi Y., Yamashita K., Doi Y.: Thermal degradation of poly[(*R*)-3-hydroxybutyrate], poly[ε-caprolactone], and poly[(*S*)-lactide]. Polymer Degradation and Stability, **76**, 53–59 (2002).
DOI: 10.1016/S0141-3910(01)00265-8

[54] Kawalec M., Sobota M., Scandola M., Kowalczuk M., Kurcok P.: A convenient route to PHB macromonomers *via* anionically controlled moderate-temperature degradation of PHB. Journal of Polymer Science Part A: Polymer Chemistry, **48**, 5490–5497 (2010).
DOI: 10.1002/pola.24357

[55] Liu Q-S., Zhu M-F., Wu W-H., Qin Z-Y.: Reducing the formation of six-membered ring ester during thermal degradation of biodegradable PHBV to enhance its thermal stability. Polymer Degradation and Stability, **94**, 18–24 (2009).
DOI: 10.1016/j.polymdegradstab.2008.10.016

[56] Hirt T. D., Neuenschwander P., Suter U. W.: Telechelic diols from poly[(*R*)-3-hydroxybutyric acid] and poly{[(*R*)-3-hydroxybutyric acid]-*co*-[(*R*)-3-hydroxyvaleric acid]}. Macromolecular Chemistry and Physics, **197**, 1609–1614 (1996).
DOI: 10.1002/macp.1996.021970503

[57] Ballistreri A., Garozzo D., Giuffrida M., Impallomeni G., Montaudo G.: Sequencing bacterial poly(β-hydroxybutyrate-*co*-β-hydroxyvalerate) by partial methanolysis, HPLC fractionation, and fast-atom-bombardment mass spectrometry analysis. Macromolecules, **22**, 2107–2111 (1989).
DOI: 10.1021/ma00195a016

[58] Reeve M. S., McCarthy S. P., Gross R. A.: Preparation and characterization of (*R*)-poly(β-hydroxybutyrate)-poly(ε-caprolactone) and (*R*)-poly(β-hydroxybutyrate)-poly(lactide) degradable diblock copolymers. Macromolecules, **26**, 888–894 (1993).
DOI: 10.1021/ma00057a002

[59] Špitalský Z., Lacík I., Lathová E., Janigová I., Chodák I.: Controlled degradation of polyhydroxybutyrate *via* alcoholysis with ethylene glycol or glycerol. Polymer Degradation and Stability, **91**, 856–861 (2006).
DOI: 10.1016/j.polymdegradstab.2005.06.019

[60] Akita S., Einaga Y., Miyaki Y., Fujita H.: Solution properties of poly(D-β-hydroxybutyrate). 1. Biosynthesis and characterization. Macromolecules, **9**, 774–780 (1976).
DOI: 10.1021/ma60053a017

[61] Freier T., Kunze C., Nischan C., Kramer S., Sternberg K., Saß M., Hopt U. T., Schmitz K. P.: *In vitro* and *in vivo* degradation studies for development of a biodegradable patch based on poly(3-hydroxybutyrate). Biomaterials, **23**, 2649–2657 (2002).
DOI: 10.1016/S0142-9612(01)00405-7

[62] Ke Y., Qu Z., Wu G., Wang Y.: Thermal and *in vitro* degradation properties of the NH_2-containing PHBV films. Polymer Degradation and Stability, **105**, 59–67 (2014).
DOI: 10.1016/j.polymdegradstab.2014.03.039

[63] Yu J., Plackett D., Chen L. X. L.: Kinetics and mechanism of the monomeric products from abiotic hydrolysis of poly[(*R*)-3-hydroxybutyrate] under acidic and alkaline conditions. Polymer Degradation and Stability, **89**, 289–299 (2005).
DOI: 10.1016/j.polymdegradstab.2004.12.026

[64] Yu G-E., Marchessault R. H.: Characterization of low molecular weight poly(β-hydroxybutyrate)s from alkaline and acid hydrolysis. Polymer, **41**, 1087–1098 (2000).
DOI: 10.1016/S0032-3861(99)00230-X

[65] Deng X. M., Hao J. Y.: Synthesis and characterization of poly(3-hydroxybutyrate) macromer of bacterial origin. European Polymer Journal, **37**, 211–214 (2001).
DOI: 10.1016/S0014-3057(00)00090-2

[66] Michalak M., Marek A. A., Zawadiak J., Kawalec M., Kurcok P.: Synthesis of PHB-based carrier for drug delivery systems with pH-controlled release. European Polymer Journal, **49**, 4149–4156 (2013).
DOI: 10.1016/j.eurpolymj.2013.09.021

[67] Arkin A. H., Hazer B.: Chemical modification of chlorinated microbial polyesters. Biomacromolecules, **3**, 1327–1335 (2002).
DOI: 10.1021/bm020079v

[68] Yalpani M., Marchessault R. H., Morin F. G., Monasterios C. J.: Synthesis of poly(3-hydroxyalkanoate) (PHA) conjugates: PHA-carbohydrate and PHA-synthetic polymer conjugates. Macromolecules, **24**, 6046–6049 (1991).
DOI: 10.1021/ma00022a024

[69] Yu G., Morin F. G., Nobes G. A. R., Marchessault R. H.: Degree of acetylation of chitin and extent of grafting PHB on chitosan determined by solid state ^{15}N NMR. Macromolecules, **32**, 518–520 (1999).
DOI: 10.1021/ma9813338

[70] Andrade A. P., Witholt B., Chang D. L., Li Z.: Synthesis and characterization of novel thermoplastic polyester containing blocks of poly[(*R*)-3-hydroxyoctanoate] and poly[(*R*)-3-hydroxybutyrate]. Macromolecules, **36**, 9830–9835 (2003).
DOI: 10.1021/ma035164p

[71] Li J., Li X., Ni X., Leong K. W.: Synthesis and characterization of new biodegradable amphiphilic poly(ethylene oxide)-*b*-poly[(*R*)-3-hydroxy butyrate]-*b*-poly(ethylene oxide) triblock copolymers. Macromolecules, **36**, 2661–2667 (2003).
DOI: 10.1021/ma025725x

[72] Li X., Mya K. Y., Ni X. P., He C. B., Leong K. W., Li J.: Dynamic and static light scattering studies on self-aggregation behavior of biodegradable amphiphilic poly(ethylene oxide)–poly[(*R*)-3-hydroxybutyrate]–poly(ethylene oxide) triblock copolymers in aqueous solution. Journal of Physical Chemistry B, **110**, 5920–5926 (2006).
DOI: 10.1021/jp057004g

[73] Wu L. P., Wang L., Wang X. J., Xu K. T.: Synthesis, characterizations and biocompatibility of novel biodegradable star block copolymers based on poly[(*R*)-3-hydroxybutyrate] and poly(ε-caprolactone). Acta Biomaterialia, **6**, 1079–1089 (2010).
DOI: 10.1016/j.actbio.2009.08.014

[74] Nguyen S., Marchessault R. H.: Synthesis and properties of graft copolymers based on poly(3-hydroxybutyrate) macromonomers. Macromolecular Bioscience, **4**, 262–268 (2004).
DOI: 10.1002/mabi.200300088

[75] Chen Z., Cheng S., Li Z., Xu K., Chen G.: Synthesis, characterization and cell compatibility of novel poly (ester urethane)s based on poly(3-hydroxybutyrate-*co*-4-hydroxybutyrate) and poly(3-hydroxybutyrate-*co*-3-hydroxyhexanoate) prepared by melting polymerization. Journal of Biomaterials Science, Polymer Edition, **20**, 1451–1471 (2009).
DOI: 10.1163/092050609X12457419007621

[76] Chen Z., Cheng S., Xu K.: Block poly(ester-urethane)s based on poly(3-hydroxybutyrate-*co*-4-hydroxybutyrate) and poly(3-hydroxyhexanoate-*co*-3-hydroxyoctanoate). Biomaterials, **30**, 2219–2230 (2009).
DOI: 10.1016/j.biomaterials.2008.12.078

[77] Ou W., Qiu H., Chen Z., Xu K.: Biodegradable block poly(ester-urethane)s based on poly(3-hydroxybutyrate-*co*-4-hydroxybutyrate) copolymers. Biomaterials, **32**, 3178–3188 (2011).
DOI: 10.1016/j.biomaterials.2011.01.031

[78] Saad G. R., Lee Y. J., Seliger H.: Synthesis and characterization of biodegradable poly(ester-urethanes) based on bacterial poly(R-3-hydroxybutyrate). Journal of Applied Polymer Science, **83**, 703–718 (2002).
DOI: 10.1002/app.2265

[79] Saad G. R., Seliger H.: Biodegradable copolymers based on bacterial poly((*R*)-3-hydroxybutyrate): Thermal and mechanical properties and biodegradation behaviour. Polymer Degradation and Stability, **83**, 101–110 (2004).
DOI: 10.1016/S0141-3910(03)00230-1

[80] Häberlein H., Seliger H., Kohler R., Sulzberger P.: Cost-effective synthesis of environmentally benign materials on the basis of poly-3-hydroxybutyrate. Polímeros, **15**, 122–126 (2005).
DOI: 10.1590/S0104-14282005000200011

[81] Seliger H., Häberlein H.: Biodegradable composite system and the use thereof. U.S. Patent 8835573, USA (2014).

[82] Zhao Q., Cheng G.: Preparation of biodegradable poly (3-hydroxybutyrate) and poly(ethylene glycol) multiblock copolymers. Journal of Materials Science, **39**, 3829–3831 (2004).
DOI: 10.1023/B:JMSC.0000030750.87512.07

[83] Li Z., Cheng S., Li S., Liu Q., Xu K., Chen G.: Novel amphiphilic poly(ester-urethane)s based on poly[(*R*)-3-hydroxyalkanoate]: Synthesis, biocompatibility and aggregation in aqueous solution. Polymer International, **57**, 887–894 (2008).
DOI: 10.1002/pi.2424

[84] Li Z., Yang X., Wu L., Chen Z., Lin Y., Xu K., Chen G.: Synthesis, characterization and biocompatibility of biodegradable elastomeric poly(ether-ester urethane)s based on poly(3-hydroxybutyrate-*co*-3-hydroxyhexanoate) and poly(ethylene glycol) *via* melting polymerization. Journal of Biomaterials Science, Polymer Edition, **20**, 1179–1202 (2009).
DOI: 10.1163/156856209X452944

[85] Zhao Q., Cheng G., Li H., Ma X., Zhang L.: Synthesis and characterization of biodegradable poly(3-hydroxybutyrate) and poly(ethylene glycol) multiblock copolymers. Polymer, **46**, 10561–10567 (2005).
DOI: 10.1016/j.polymer.2005.08.014

[86] Li X., Loh X. J., Wang K., He C. B., Li J.: Poly(ester urethane)s consisting of poly[(*R*)-3-hydroxybutyrate] and poly(ethylene glycol) as candidate biomaterials: Characterization and mechanical property study. Biomacromolecules, **6**, 2740–2747 (2005).
DOI: 10.1021/bm050234g

[87] Liu K. L., Choo E. S. G., Wong S. Y., Li X., He C. B., Wang J., Li J.: Designing poly[(*R*)-3-hydroxybutyrate]-based polyurethane block copolymers for electrospun nanofiber scaffolds with improved mechanical properties and enhanced mineralization capability. Journal of Physical Chemistry B, **114**, 7489–7498 (2010).
DOI: 10.1021/jp1018247

[88] Naguib H. F., Aziz M. S. A., Sherif S. M., Saad G. R.: Synthesis and thermal characterization of poly(ester-ether urethane)s based on PHB and PCL-PEG-PCL blocks. Journal of Polymer Research, **18**, 1217–1227 (2011).
DOI: 10.1007/s10965-010-9525-y

[89] Saad G. R.: Calorimetric and dielectric study of the segmented biodegradable poly(ester-urethane)s based on bacterial poly[(*R*)-3-hydroxybutyrate]. Macromolecular Bioscience, **1**, 387–396 (2001).
DOI: 10.1002/1616-5195(20011201)1:9<387::AID-MABI387>3.0.CO;2-4

[90] Saad B., Ciardelli G., Matter S., Welti M., Uhlschmid G. K., Neuenschwander P., Suter U. W.: Characterization of the cell response of cultured macrophages and fibroblasts to particles of short-chain poly[(R)-3-hydroxybutyric acid]. Journal of Biomedical Materials Research, **30**, 429–439 (1996).
DOI: 10.1002/(SICI)1097-4636(199604)30:4<429::AID-JBM1>3.0.CO;2-R

[91] Saad B., Ciardelli G., Matter S., Welti M., Uhlschmid G. K., Neuenschwander P., Suter U. W.: Degradable and highly porous polyesterurethane foam as biomaterial: Effects and phagocytosis of degradation products in osteoblasts. Journal of Biomedical Materials Research, **39**, 594–602 (1998).
DOI: 10.1002/(SICI)1097-4636(19980315)39:4<594::AID-JBM14>3.0.CO;2-7

[92] Loh X. J., Goh S. H., Li J.: New biodegradable thermogelling copolymers having very low gelation concentrations. Biomacromolecules, **8**, 585–593 (2007).
DOI: 10.1021/bm0607933

[93] Loh X. J., Goh S. H., Li J.: Biodegradable thermogelling poly[(*R*)-3-hydroxybutyrate]-based block copolymers: Micellization, gelation, and cytotoxicity and cell culture studies. Journal of Physical Chemistry B, **113**, 11822–11830 (2009).
DOI: 10.1021/jp903984r

[94] Liu Q., Cheng S., Li Z., Xu K., Chen G-Q.: Characterization, biodegradability and blood compatibility of poly[(R)-3-hydroxybutyrate] based poly(ester-urethane)s. Journal of Biomedical Materials Research Part A, **90**, 1162–1176 (2009).
DOI: 10.1002/jbm.a.32180

[95] Lendlein A., Neuenschwander P., Suter U. W.: Tissue-compatible multiblock copolymers for medical applications, controllable in degradation rate and mechanical properties. Macromolecular Chemistry and Physics, **199**, 2785–2796 (1998).
DOI: 10.1002/(SICI)1521-3935(19981201)199:12<2785::AID-MACP2785>3.0.CO;2-X

[96] Hirt T. D., Neuenschwander P., Suter U. W.: Synthesis of degradable, biocompatible, and tough block-copolyesterurethanes. Macromolecular Chemistry and Physics, **197**, 4253–4268 (1996).
DOI: 10.1002/macp.1996.021971221

[97] Saad B., Neuenschwander P., Uhlschmid G. K., Suter U. W.: New versatile, elastomeric, degradable polymeric materials for medicine. International Journal of Biological Macromolecules, **25**, 293–301 (1999).
DOI: 10.1016/S0141-8130(99)00044-6

[98] Andrade A. P., Neuenschwander P., Hany R., Egli T., Witholt B., Li Z.: Synthesis and characterization of novel copoly(ester–urethane) containing blocks of poly-[(*R*)-3-hydroxyoctanoate] and poly-[(*R*)-3-hydroxybutyrate]. Macromolecules, **35**, 4946–4950 (2002).
DOI: 10.1021/ma012223v

[99] Pan J., Li G., Chen Z., Chen X., Zhu W., Xu K.: Alternative block polyurethanes based on poly(3-hydroxybutyrate-*co*-4-hydroxybutyrate) and poly(ethylene glycol). Biomaterials, **30**, 2975–2984 (2009).
DOI: 10.1016/j.biomaterials.2009.02.005

[100] Arslan H., Menteş A., Hazer B.: Synthesis and characterization of diblock, triblock, and multiblock copolymers containing poly(3-hydroxy butyrate) units. Journal of Applied Polymer Science, **94**, 1789–1796 (2004).
DOI: 10.1002/app.21112

[101] Nuyken O., Pask S. D.: Ring-opening polymerization – An introductory review. Polymers, **5**, 361–403 (2013). DOI: 10.3390/polym5020361

[102] Isono T., Asai S., Satoh Y., Takaoka T., Tajima K., Kakuchi T., Satoh T.: Controlled/living ring-opening polymerization of glycidylamine derivatives using *t*-Bu-P4/alcohol initiating system leading to polyethers with pendant primary, secondary, and tertiary amino groups. Macromolecules, **48**, 3217–3229 (2015). DOI: 10.1021/acs.macromol.5b00556

[103] Kwiecień I., Adamus G., Bartkowiak A., Kowalczuk M.: Synthesis and structural characterization at the molecular level of oligo(3-hydroxybutyrate) conjugates with antimicrobial agents designed for food packaging materials. Designed Monomers and Polymers, **17**, 311–321 (2014). DOI: 10.1080/15685551.2013.840505

[104] Maksymiak M., Kowalczuk M., Adamus G.: Electrospray tandem mass spectrometry for the structural characterization of p-coumaric acid–oligo(3-hydroxybutyrate) conjugates. International Journal of Mass Spectrometry, **359**, 6–11 (2014). DOI: 10.1016/j.ijms.2013.11.009

[105] Adamus G., Sikorska W., Janeczek H., Kwiecień M., Sobota M., Kowalczuk M.: Novel block copolymers of atactic PHB with natural PHA for cardiovascular engineering: Synthesis and characterization. European Polymer Journal, **48**, 621–631 (2012). DOI: 10.1016/j.eurpolymj.2011.12.017

[106] Adamus G., Sikorska W., Kowalczuk M., Montaudo M., Scandola M.: Sequence distribution and fragmentation studies of bacterial copolyester macromolecules: Characterization of PHBV macroinitiator by electrospray ion-trap multistage mass spectrometry. Macromolecules, **33**, 5797–5802 (2000). DOI: 10.1021/ma000005g

[107] Iwata T., Doi Y., Kasuya K-I., Inoue Y.: Visualization of enzymatic degradation of poly[(*R*)-3-hydroxybutyrate] single crystals by an extracellular PHB depolymerase. Macromolecules, **30**, 833–839 (1997). DOI: 10.1021/ma961352m

[108] Liu Q., Deng B., Tung C-H., Zhu M., Shyr T-W.: Non-isothermal crystallization kinetics of poly(ε-caprolactone) blocks in double crystalline triblock copolymers containing poly(3-hydroxybutyrate-*co*-3-hydroxyvalerate) and poly(ε-caprolactone) units. Journal of Polymer Science Part B: Polymer Physics, **48**, 2288–2295 (2010). DOI: 10.1002/polb.22112

[109] Wu L., Chen S., Li Z., Xu K., Chen G-Q.: Synthesis, characterization and biocompatibility of novel biodegradable poly[((*R*)-3-hydroxybutyrate)-*block*-(D,L-lactide)-*block*-(ε-caprolactone)] triblock copolymers. Polymer International, **57**, 939–949 (2008). DOI: 10.1002/pi.2431

[110] Ayres N.: Atom transfer radical polymerization: A robust and versatile route for polymer synthesis. Polymer Reviews, **51**, 138–162 (2011). DOI: 10.1080/15583724.2011.566402

[111] Xue C-H., Guo X-J., Ma J-Z., Jia S-T.: Fabrication of robust and antifouling superhydrophobic surfaces via surface-initiated atom transfer radical polymerization. ACS Applied Materials and Interfaces, **7**, 8251–8259 (2015). DOI: 10.1021/acsami.5b01426

[112] Loh X. J., Zhang Z-X., Wu Y-L., Lee T. S., Li J.: Synthesis of novel biodegradable thermoresponsive triblock copolymers based on poly[(*R*)-3-hydroxybutyrate] and poly(*N*-isopropylacrylamide) and their formation of thermoresponsive micelles. Macromolecules, **42**, 194–202 (2009). DOI: 10.1021/ma8019865

[113] Loh X. J., Ong S. J., Tung Y. T., Choo H. T.: Incorporation of poly[(*R*)-3-hydroxybutyrate] into cationic copolymers based on poly(2-(dimethylamino)ethyl methacrylate) to improve gene delivery. Macromolecular Bioscience, **13**, 1092–1099 (2013). DOI: 10.1002/mabi.201300050

[114] Zhang X., Yang H., Liu Q., Zheng Y., Xie H., Wang Z., Cheng R.: Synthesis and characterization of biodegradable triblock copolymers based on bacterial poly[(*R*)-3-hydroxybutyrate] by atom transfer radical polymerization. Journal of Polymer Science Part A: Polymer Chemistry, **43**, 4857–4869 (2005). DOI: 10.1002/pola.20953

[115] Neugebauer D., Rydz J., Goebel I., Dacko P., Kowalczuk M.: Synthesis of graft copolymers containing biodegradable poly(3-hydroxybutyrate) chains. Macromolecules, **40**, 1767–1773 (2007). DOI: 10.1021/ma062251j

[116] Arslan H., Yesilyurt N., Hazer B.: Brush type copolymers of poly(3-hydroxybutyrate) and poly(3-hydroxyoctanoate) with same vinyl monomers *via* 'grafting from' technique by using atom transfer radical polymerization method. Macromolecular Symposia, **269**, 23–33 (2008). DOI: 10.1002/masy.200850905

[117] Arslan H., Yeşilyurt N., Hazer B.: The synthesis of poly(3-hydroxybutyrate)-*g*-poly(methylmethacrylate) brush type graft copolymers by atom transfer radical polymerization method. Journal of Applied Polymer Science, **106**, 1742–1750 (2007). DOI: 10.1002/app.26870

[118] Koseva N. S., Novakov C. P., Rydz J., Kurcok P., Kowalczuk M.: Synthesis of aPHB-PEG brush copolymers through ATRP in a macroinitiator–macromonomer feed system and their characterization synthesis of aPHB-PEG brush co-polymers through ATRP in a macroinitiator–macromonomer feed system and their characterization. Designed Monomers and Polymers, **13**, 579–595 (2010). DOI: 10.1163/138577210X530675

[119] Nguyen S., Marchessault R. H.: Atom transfer radical copolymerization of bacterial poly(3-hydroxybutyrate) macromonomers and methyl methacrylate. Macromolecules, **38**, 290–296 (2005).
DOI: 10.1021/ma048899i

[120] Cai Z. J., Yang G.: Copolymerization of poly(hydroxybutyrate) and poly(ethylene glycol) by coupling method (in Chinese). Polymer Materials Science and Engineering, **27**, 145–148 (2011).

[121] Hazer B.: Preparation of polystyrene poly(β-hydroxy nonanoate) graft copolymers. Polymer Bulletin, **33**, 431–438 (1994).
DOI: 10.1007/BF00293487

[122] Hazer B.: Poly(β-hydroxynonanoate) and polystyrene or poly(methyl methacrylate) graft copolymers: Microstructure characteristics and mechanical and thermal behavior. Macromolecular Chemistry and Physics, **197**, 431–441 (1996).
DOI: 10.1002/macp.1996.021970202

[123] Erbil H. Y., Hazer B.: Surface free energy analysis of polystyrene–poly(β-hydroxynonanoate) graft copolymers. Journal of Applied Polymer Science, **60**, 1313–1320 (1996).
DOI: 10.1002/(SICI)1097-4628(19960531)60:9<1313 ::AID-APP6>3.0.CO;2-M

[124] Kwiecień I., Radecka I., Kowalczuk M., Adamus G.: Transesterification of PHA to oligomers covalently bonded with (bio)active compounds containing either carboxyl or hydroxyl functionalities. PloS one, **10**, e0120149/1–e0120149/20 (2015).
DOI: 10.1371/journal.pone.0120149

[125] Ravenelle F., Marchessault R. H.: One-step synthesis of amphiphilic diblock copolymers from bacterial poly([*R*]-3-hydroxybutyric acid). Biomacromolecules, **3**, 1057–1064 (2002).
DOI: 10.1021/bm025553b

[126] Chen C., Fei B., Peng S. W., Zhuang Y. G., Chen X. S., Dong L. S., Feng Z. L.: Study on the transesterification of poly(β-hydroxybutyrate) and poly(ε-caprolactone) (in Chinese). Acta Polymerica Sinica, **2**, 142–148 (2002).

[127] Park J., Park J-G., Choi W-M., Ha C-S., Cho W-J.: Synthesis and photo- and biodegradabilities of poly [(hydroxybutyrate-*co*-hydroxyvalerate)-*g*-phenyl vinyl ketone]. Journal of Applied Polymer Science, **74**, 1432–1439 (1999).
DOI: 10.1002/(SICI)1097-4628(19991107)74:6<1432 ::AID-APP16>3.0.CO;2-Z

[128] Chen C., Peng S., Fei B., An Y., Zhuang Y., Dong L., Feng Z., Chen S., Xia H.: Study on the properties of poly(β-hydroxybutyrate) grafted with maleic anhydride (in Chinese). Acta Polymerica Sinica, **4**, 450–454 (2001).

[129] Chen C., Peng S. W., Fei B., Zhuang Y. G., Dong L. S., Feng Z. L., Chen S., Xia H. M.: Synthesis and characterization of maleated poly(3-hydroxybutyrate). Journal of Applied Polymer Science, **88**, 659–668 (2003).
DOI: 10.1002/app.11771

[130] Chen C., Fei B., Peng S. W., Zhuang Y. G., Dong L. S., Feng Z. L.: Isothermal crystallization kinetics and melting behavior of poly(β-hydroxybutyrate) and maleated poly(β-hydroxybutyrate) (in Chinese). Acta Polymerica Sinica, **1**, 68–72 (2002).

[131] Chen C., Peng S. W., Fei B., An Y. X., Zhuang Y. G., Dong L. S., Feng Z. L.: Study on the free radical graft copolymerization of maleic anhydride onto poly(β-hydroxybutyrate) (in Chinese). Chinese Journal of Applied Chemistry, **1**, 12–15 (2001).

[132] Mitomo H., Enjôji T., Watanabe Y., Yoshii F., Makuuchi K., Saito T.: Radiation-induced graft polymerization of poly(3-hydroxybutyrate) and its copolymer. Journal of Macromolecular Science Part A: Pure and Applied Chemistry, **32**, 429–442 (1995).
DOI: 10.1080/10601329508013674

[133] Mitomo H., Watanabe Y., Yoshii F., Makuuchi K.: Radiation effect on polyesters. Radiation Physics and Chemistry, **46**, 233–238 (1995).
DOI: 10.1016/0969-806X(95)00018-S

[134] Bahari K., Mitomo H., Enjôji T., Hasegawa S., Yoshii F., Makuuchi K.: Radiation-induced graft polymerization of styrene onto poly(3-hydroxybutyrate) and its copolymer with 3-hydroxyvalerate. Die Angewandte Makromolekulare Chemie, **250**, 31–44 (1997).
DOI: 10.1002/apmc.1997.052500103

[135] Bahari K., Mitomo H., Enjôji T., Yoshii F., Makuuchi K.: Degradability of poly(3-hydroxybutyrate) and its copolymer grafted with styrene by radiation. Polymer Degradation and Stability, **61**, 245–252 (1998).
DOI: 10.1016/S0141-3910(97)00147-X

[136] Jiang T., Hu P.: Radiation-induced graft polymerization of isoprene onto polyhydroxybutyrate. Polymer Journal, **33**, 647–653 (2001).
DOI: 10.1295/polymj.33.647

[137] Mitomo H., Sasaoka T., Yoshii F., Makuuchi K., Saito T.: Radiation-induced graft polymerization of acrylic acid onto poly (3-hydroxybutyrate) and its copolymer. Sen'i Gakkaishi, **52**, 623–626 (1996).
DOI: 10.2115/fiber.52.11_623

[138] Ye H., Yang D., Hu P., Zhang F., Qi Q., Zhao W.: Grafting of maleic anhydride onto poly(β-hydroxybutyrate) by [60]Co γ radiation. Acta Polymerica Sinica, **5**, 678–682 (2005).

[139] Hazer B., Lenz R. W., Çakmakli B., Borcakli M., Koçer H.: Preparation of poly(ethylene glycol) grafted poly(3-hydroxyalkanoate) networks. Macromolecular Chemistry and Physics, **200**, 1903–1907 (1999).
DOI: 10.1002/(SICI)1521-3935(19990801)200:8<1903 ::AID-MACP1903>3.0.CO;2-J

Efficient surface modification of MWCNTs with vitamin B₁ and production of poly(ester-imide)/MWCNTs nanocomposites containing L-phenylalanine moiety: Thermal and microscopic study

S. Mallakpour[1,2,3*], *S. Soltanian*[1]

[1]Organic Polymer Chemistry Research Laboratory, Department of Chemistry, Isfahan University of Technology, 84156-83111 Isfahan, Islamic Republic of Iran
[2]Nanotechnology and Advanced Materials Institute, Isfahan University of Technology, 84156-83111 Isfahan, Islamic Republic of Iran
[3]Center of Excellence in Sensors and Green Chemistry, Department of Chemistry, Isfahan University of Technology, 84156-83111 Isfahan, Islamic Republic of Iran

Abstract. A simple and efficient method was presented for chemical functionalization of multi-walled carbon nanotubes (MWCNTs) with vitamin B₁. Poly(ester-imide) (PEI) based nanocomposites were prepared by the incorporation of different amounts of modified MWCNTs (5, 10, 15 wt%) into a chiral and biodegradable PEI by solution blending and ultrasonic dispersion methods. The chiral PEI was produced by a step-growth polymerization of chiral diacid with 4,4′-thiobis(2-tert-butyl-5-methylphenol). Spectroscopic and microscopic techniques were used to examine the chemical structure, morphology and thermal stability of the functionalized MWCNTs and the obtained nanocomposites. The microstructure study revealed the homogeneous dispersion of modified MWCNTs throughout the PEI matrix. Thermogravimetric analysis results confirmed that the heat stability of the prepared composites was improved compared to the pure PEI.

Keywords: polymer composites, multi-walled carbon nanotubes, functionalization, vitamin B₁, ultrasonic process

1. Introduction

Carbon nanotubes (CNTs) have attracted many basic research efforts since their discovery in 1991 [1]. They have an exceptional structure with superior physical and chemical properties as well as excellent mechanical performance. Owing to these properties, they have been widely used in nanoelectronic devices, actuators, air and water filters, chemical sensors, biosensors, drug delivery, phototherapy, etc. [2–4]. They can serve as a promising reinforcement phase incorporated into a polymer matrix to prepare high-performance polymer nanocomposites [5–10].

It has been found that the as-produced CNTs tend to agglomerate together due to the high aspect ratios and very strong van der Waals forces between the nanotubes. Therefore, poor dispersion, the lack of solubility and weak chemical compatibility with the polymer matrix have become a bottleneck in the application of CNTs [11]. Mechanical methods such as ultrasonication and high-shear mixing as well as chemical methods including non-covalent and covalent functionalization were among the commonly used methods to prevent CNTs aggregation and achieve good dispersion in the polymer matrix. The chemical functionalization of CNTs not only

---

enhances the dispersion ability of CNTs in solvents and composites, but can also improve the compatibility of CNTs with the composite matrix [3, 12, 13]. Ultrasonic irradiation is widely used to dispersing nanoparticles and colloids, functionalization of CNTs and produce nanocomposites, nanomaterials, and nanoforms of chemical compounds [14]. The chemical effects of ultrasound derive from acoustic cavitation. The ultrasonic cavitation can generate bubble collapse and high-energy inter-particle collisions, producing intense local heating and high pressures together with implosion shock waves and micro jets in the liquid medium. The combined effect is able to provoke chemical reactions on the CNTs [15].

Poly(ester-imide)s (PEI)s show good mechanical properties, high thermal stability, facile processing and electrical insulation [16–18]. This class of polymers brings together the desirable characteristics from both polyesters and polyimides. These properties make them suitable for different applications in printed circuit boards, engineering thermoplastics, electronic devices, membranes, and adhesives, [19–21] being a promising matrix candidate for hybrid materials.

In this paper, the attaching of thiamine hydrochloride (vitamin B_1) on carboxylated-multi-walled carbon nanotubes (MWCNTs-COOH) was carried out under ultrasonic irradiation. The chiral PEI was prepared by a direct polycondensation of equimolecular amounts of aromatic diol and natural amino acid based diacid. The different loading levels of functionalized MWCNTs (5, 10, 15 wt%) were effectively dispersed in the aromatic polymer through ultrasonic irradiation to prepare MWCNTs reinforced polymer nanocomposites. The structure and morphology characterization as well as thermal stability of the modified MWCNTs and the obtained nanocomposites were investigated by FT-IR spectroscopy, thermogravimetric analysis (TGA), X-ray diffraction (XRD), transmission electron microscopy (TEM), and field emission scanning electron microscopy (FE-SEM).

2. Experimental
2.1. Materials
MWCNTs-COOH synthesized by thermal chemical vapor deposition process (CVD), having inner diameter of 5–10 nm, outer diameter of 10–20 nm, purity >95 wt%, carboxyl content of 2.00 wt% and length ~30 μm were used. Other solvents and chemicals were reagent-grade quality, achieved commercially from Aldrich Chemical Co. (Milwaukee, WI), Fluka Chemical Co. (Buchs, Switzerland), Riedel-deHaen AG (Seelze, Germany) and Merck Chemical Co. (Germany). Pyromellitic dianhydride (benzen-1,2,4,5-tetracarboxylic dianhydride) (1) was purified by recrystallization from acetic anhydride followed by sublimation. N,N-dimethylformamide (DMF) and N,N-dimethylacetamide (DMAc) were distilled over barium oxide under reduced pressure. Thiamine hydrochloride, 4,4′-thiobis(2-tert-butyl-5-methylphenol) (TTMP) and L-phenylalanine were used as obtained without further purification.

2.2. Measurements
FE-SEM images were obtained at 15 kV using a HITACHI S-4160 instrument (Tokyo, Japan). TEM analyses were performed using a Philips CM 120 operating at 100 kV (Germany). The XRD patterns of the samples were recorded using a Philips X'PERT MPD with a copper target at 40 kV and 35 mA and Cu Kα λ =1.54 Å in the range 10–80° at the speed of 0.05 °C/min. TGA data were taken on a STA503 instrument (Bahr-Thermoanalyse GmbH, Hüllhorst, Germany) in a nitrogen atmosphere at a rate of 20 °C/min. FT-IR spectra were recorded with a Jasco-680 (Tokyo, Japan) spectrometer at a resolution of 4 cm^{-1} and scanned at wavenumber range of 400–4000 cm^{-1}. The spectra of solids were obtained using KBr pellets. Band intensities were assigned as weak (*w*), medium (*m*), shoulder (*sh*), strong (*s*) and broad (*br*). The reaction was carried out on MISONIX ultrasonic liquid processors, XL-2000 SERIES (Raleigh, NC, USA). Ultrasound was a wave of frequency 2.25·10^4 Hz and power of 100 W.

2.3. Monomer synthesis
N,N′-(pyromellitoyl)-bis-L-phenylalanine diacid (3) as an optically active monomer was prepared based on our previous research (Figure 1) [22].

2.4. Polymerization procedure
Optically active and biodegradable PEI was synthesized by the direct polycondensation of equimolecular amounts of aromatic diol (4) and chiral diacid (3), using TsCl/DMF/Py as a condensing agent (Figure 1) [23].
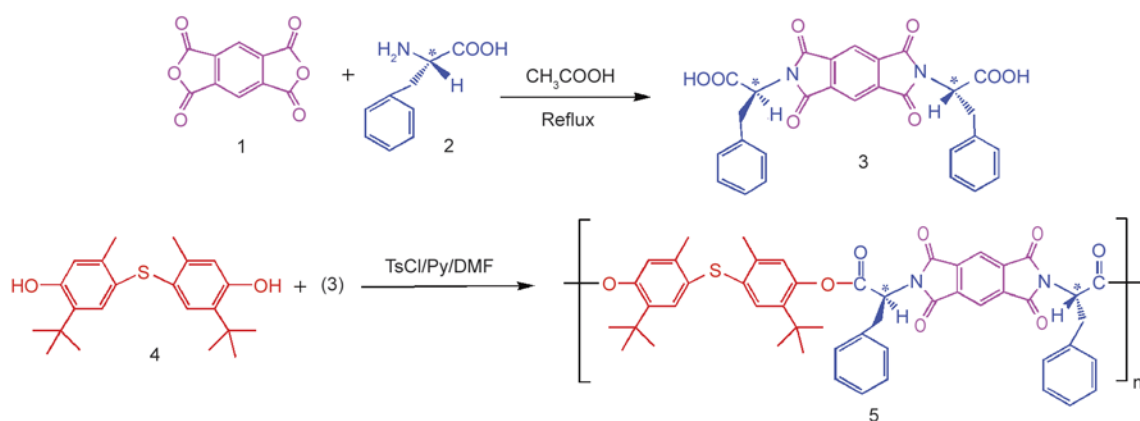
Figure 1. Synthetic route used to prepare the PEI

2.5. Thiamine functionalized MWCNTs (Tm-MWCNTs)

The MWCNTs-COOH was chemically modified with vitamin B_1 as shown in Figure 2. 100 mg of vitamin B_1 was dissolved in 10 mL of H_2O. Then the MWCNTs-COOH (50 mg) and 0.10 mL of conc. HCl were added to this solution and the whole mixture was ultrasonicated for one hour. After irradiation, the mixture was centrifuged, washed thoroughly with water, and dried under vacuum to give the product of Tm-MWCNTs.

2.6. Preparation of the PEI/Tm-MWCNTs nanocomposites

The different amounts of functionalized MWCNTs (5, 10, 15 wt%) were dispersed in DMAc solvent and stirred for 1 day at 30–40 °C. Then, the PEI was added into this solution and ultrasonicated in a water bath for 1 h. Finally, the obtained suspension was poured into glass Petri dishes, followed by solvent evaporation at room temperature. The obtained nanocomposites were further dried under vacuum at 120 °C for 6 h to remove the remaining solvent.

3. Results and discussion
3.1. Fabrication of Tm-MWCNTs

Weakly dispersed CNTs often weaken the performance of CNTs-based composites materials. Chemical modification of the CNTs is essential to achieve a sufficient interfacial adhesion and obtain the advantage of exceptional properties of the CNTs to prepare polymer composites with enhanced performance [24]. In this work, the surface of MWCNTs-COOH was chemically functionalized with vitamin B_1 as a biological molecule, under ultrasonic irradiation. Vitamin B_1 is a water-soluble vitamin, pharmaceutically and biologically important compound. It plays a major role in the carbohydrate metabolism and good health of the body, mainly in terms of emotional health and well being [25, 26]. The carboxylic acid groups on the surface of MWCNTs could be reacted with the hydroxyl group of vitamin B_1 to form ester groups. The vitamin B_1 is expected to interact with different polar groups on the surface of MWCNTs through van der Waals, hydrogen bonding, electrical and hydrophobic interaction. Also, the aromatic structure of vitamin B_1
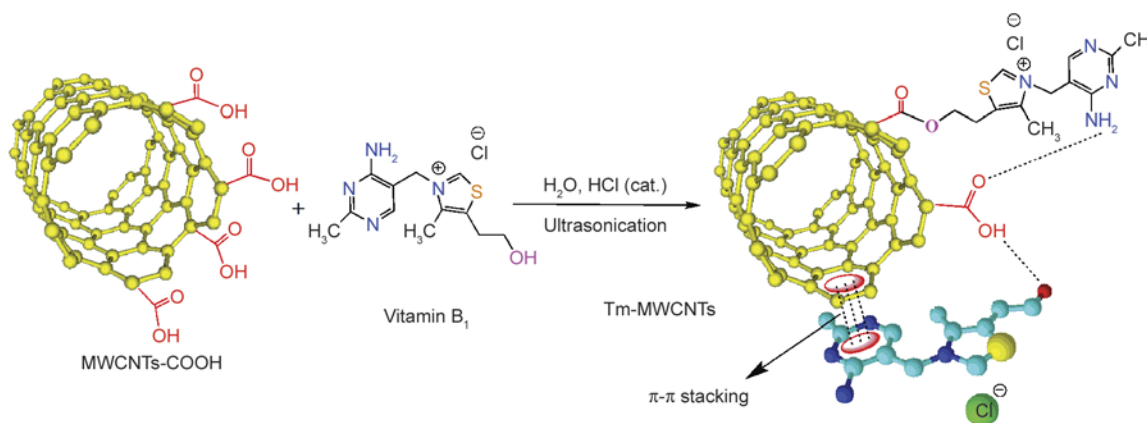

Figure 2. Chemical attachment of vitamin B_1 to MWCNTs-COOH

could provide the possibility for π–π interactions with the delocalized π-bonds on the CNTs wall (Figure 2). The modification of CNTs surface with vitamin B_1 is anticipated to reduce the tendency of CNTs to aggregate, increase its dispersion in solvents and improve interfacial interaction between polymer matrix and the Tm-MWCNTs.

3.2. Preparation of PEI/Tm-MWCNTs nanocomposites

The novel nanocomposites were prepared by mixing the appropriate amounts of functionalized MWCNTs and the optically active PEI under ultrasonic irradiations. CNTs functionalization and ultrasonication were used as useful methods to improve the interfacial interaction between MWCNTs and PEI matrix leading to efficient MWCNTs dispersion [27–31]. The obtained PEI contains heteroatoms with high-electron density, such as sulfur, nitrogen, and oxygen in its molecular structure, which provide the possibility for hydrogen bonding, van der Waals, electrical and hydrophobic interaction with different polar groups on the surface of modified MWCNTs. Also, the aromatic structure of PEI prefers to form π–π interactions with the delocalized π-bonds on the CNTs wall, as well as pyrimidine and thiazole ring of vitamin B_1 attached on the CNTs surface. Figure 3 illustrates possible interactions between the PEI chains and Tm-MWCNTs.

3.3. FT-IR spectroscopy

Figure 4 shows the FT-IR spectra of MWCNTs-COOH, Tm-MWCNTs, vitamin B_1, PEI and nanocomposites with 5, 10 and 15 wt% of Tm-MWCNTs. For MWCNTs-COOH, a characteristic peak at wavenumber of 3454 cm^{-1} corresponded to the O–H stretching mode of the carboxylic acid groups and the absorption peaks at 2852 and 2922 cm^{-1} could be related to C–H stretching vibrations of MWCNTs-COOH defects [32]. The peaks at 1629 and 1431 cm^{-1} could be assigned to the C=C aromatic ring stretching of the CNTs backbone [33] (Figure 4 curve (a)). For functionalized MWCNTs, the appearance of new peaks resulted from the functionalization of MWCNTs with vitamin B_1. The absorption bands at 1735 and 3464 cm^{-1} could be attributed to the stretching vibration of C=O and O–H groups, respectively (Figure 4 curve (b)). For pure PEI, the bands at 1383 and 726 cm^{-1} were related to the presence of the imide heterocycle in this polymer. The absorption bands at 1780 and 1726 cm^{-1} corresponded to the carbonyl stretching vibrations of the imide and ester groups, respectively (Figure 4 curve (d)). The presence of CNTs in the polymer matrix demonstrated little changes in the FT-IR spectrum. It was probably attributed to low MWCNTs content, the weak vibration signal of MWCNTs and overlapping with the absorption peaks of pure PEI (Figure 4 curves (e–g)).
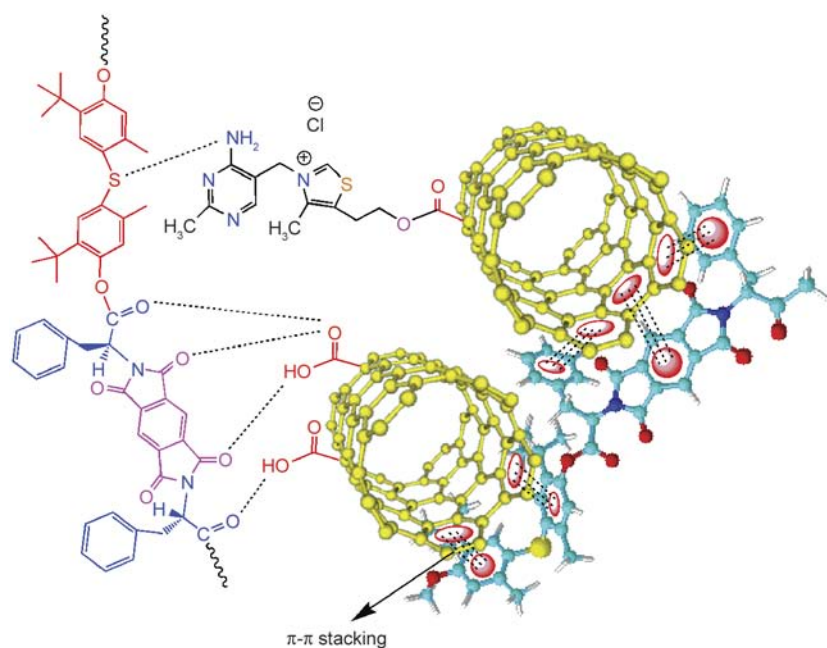

Figure 3. Schematic illustration of the possible interaction between the Tm-MWCNTs and the PEI matrix
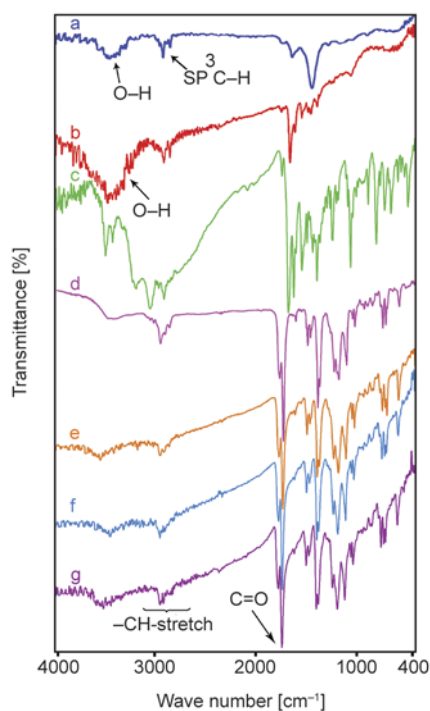
Figure 4. FT-IR spectra of (a) MWCNTs-COOH, (b) Tm-MWCNTs, (c) thiamine hydrochloride, (d) pure PEI, (e) PEI/Tm-MWCNTs 5 wt%, (f) PEI/Tm-MWCNTs 10 wt%, (g) PEI/Tm-MWCNTs 15 wt%
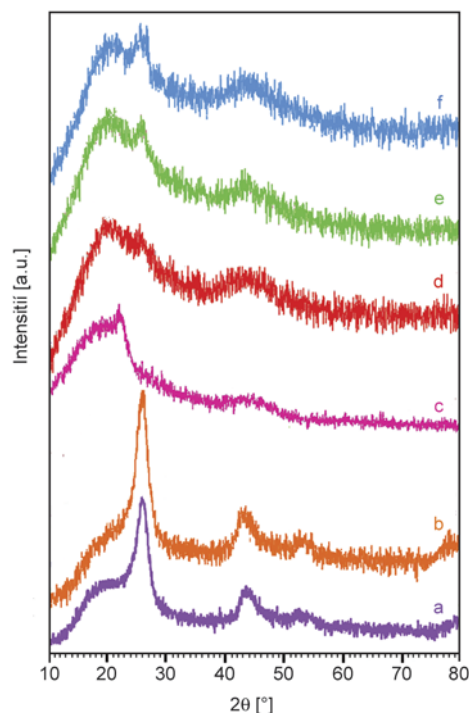

Figure 5. XRD curves of (a) MWCNTs-COOH, (b) Tm-MWCNTs, (c) PEI, (d) PEI/Tm-MWCNTs 5 wt%, (e) PEI/Tm-MWCNTs 10 wt%, (f) PEI/Tm-MWCNTs 15 wt%

3.4. XRD studies

The XRD patterns of MWCNTs-COOH, Tm-MWCNTs, pure PEI, and nanocomposites with different loadings (5, 10, 15 wt%) are demonstrated in Figure 5. MWCNTs-COOH showed two peaks around $2\theta = 26$ and $43°$, which related to the interlayer spacing d(002) and d(100) reflections of the carbon atoms, respectively (Figure 5 curve (a)) [34]. The XRD pattern of Tm-MWCNTs was similar to MWCNTs-COOH. It confirmed that the cylinder wall structure and inter planner spacing of MWCNTs did not change (Figure 5 curve (b)). For the neat PEI, a broad peak centering at $2\theta = 18°$ suggested that the PEI was in amorphous nature (Figure 5 curve (c)). For the nanocomposites, both characteristic peaks of the MWCNTs and the broad amorphous peak of PEI were observed. The peak intensity of Tm-MWCNTs was enhanced by the increasing of the loading level of Tm-MWCNTs in the nanocomposites (Figure 5 curves (d–f)).

3.5. Surface morphology studies

The morphological characterization of MWCNTs-COOH and Tm-MWCNTs was obtained using FE-SEM and the results are shown in Figure 6. The change of morphology after functionalization was evidenced. The diameter of the Tm-MWCNTs became a little bigger than that of MWCNTs-COOH. This could be due to the absorption of vitamin B_1 on the surface of MWCNTs during the functionalization. The FE-SEM images of the fracture surfaces of pure PEI and nanocomposites are presented in Figure 7. It could be seen that the pure PEI had nanostructured morphology with a relatively spherical and smooth surface compared to the fracture surfaces of the nanocomposites (Figure 7a, 7b). For the nanocomposites, the distribution of bright dots and lines with protruding out of the polymer matrix was seen. These dots and lines represented the ends of the functionalized MWCNTs. It is clear that the Tm-MWCNTs were well dispersed in the PEI matrix and the increase of CNTs content did not lead to the formation of noticeable aggregation. The histograms of CNTs diameter distribution for the nanocomposites 10 and 15 wt%, showed mean CNTs diameter sizes of 30.98 and 34.50 nm, respectively (Figure 7). The effect of functionalization on the structure of the MWCNTs was studied by TEM (Figure 8). The MWCNTs-COOH were observed in the form of bundle and showed smooth surface with obvious aggregation (Figure 8e). After the attachment of vitamin B_1 onto the surface of MWCNTs, the debundling
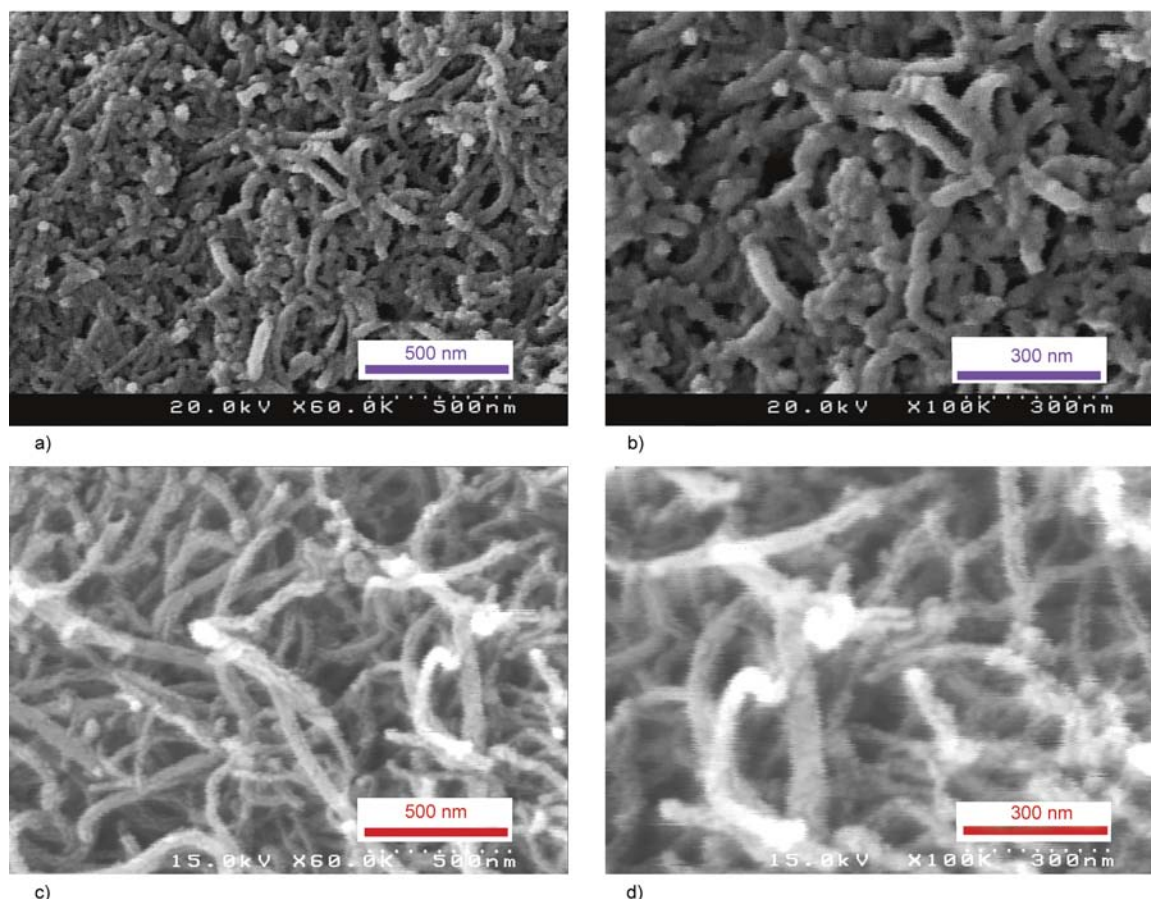
Figure 6. The FE-SEM images of the fracture surfaces of Tm-MWCNTs (a, b) and MWCNTs-COOH (c, d)

of aggregates was observed and the diameter of MWCNTs was slightly increased. Moreover, the increased roughness of modified CNTs surface was apparent, which could be attributed to the functionalization (Figure 8a–8d).

The TEM images of nanocomposites containing 10 wt% Tm-MWCNTs are shown in Figure 9. The presence of isolated and well distributed nanotubes was clearly observed. The Tm-MWCNTs were embedded in the polymer matrix and the polymer layer wrapped around them. The result indicated a good compatibility and strong interfacial adhesion between modified CNTs and the polymer matrix.

3.6. Thermal properties

Figure 10 shows the TGA curve of MWCNTs-COOH, Tm-MWCNTs, pure PEI and the nanocomposites with different contents of Tm-MWCNTs. The thermal analysis data of the samples are summarized in Tables 1 and 2. Table 1 demonstrates ther-

Table 2. Thermal stability of CNTs samples obtained from TGA thermograms

Sample	T_5 [°C][a]	Char yield [%]
MWCNTs-COOH	550	90
Tm-MWCNTs	227	42

[a]Temperature at which 5% weight loss was recorded by TGA at the heating rate of 20 °C/min under a nitrogen atmosphere.

Table 1. Thermal properties of the PEI and nanocomposites

Sample	T_5 [°C][a]	T_{10} [°C][b]	Char yield [%][c]	LOI[d]
Pure PEI	387	410	20	25.5
PEI/Tm-MWCNTs 5 wt%	388	414	30	29.5
PEI/Tm-MWCNTs 10 wt%	399	435	36	31.9
PEI/Tm-MWCNTs 15 wt%	417	459	38	32.7

[a]Temperature at which 5% weight loss was recorded by TGA at heating rate of 20 °C/min under a nitrogen atmosphere.
[b]Temperature at which 10% weight loss was recorded by eTGA at heating rate of 20 °C/min under a nitrogen atmosphere.
[c]Weight percentage of material left undecomposed after TGA analysis at a temperature of 800 °C under a nitrogen atmosphere.
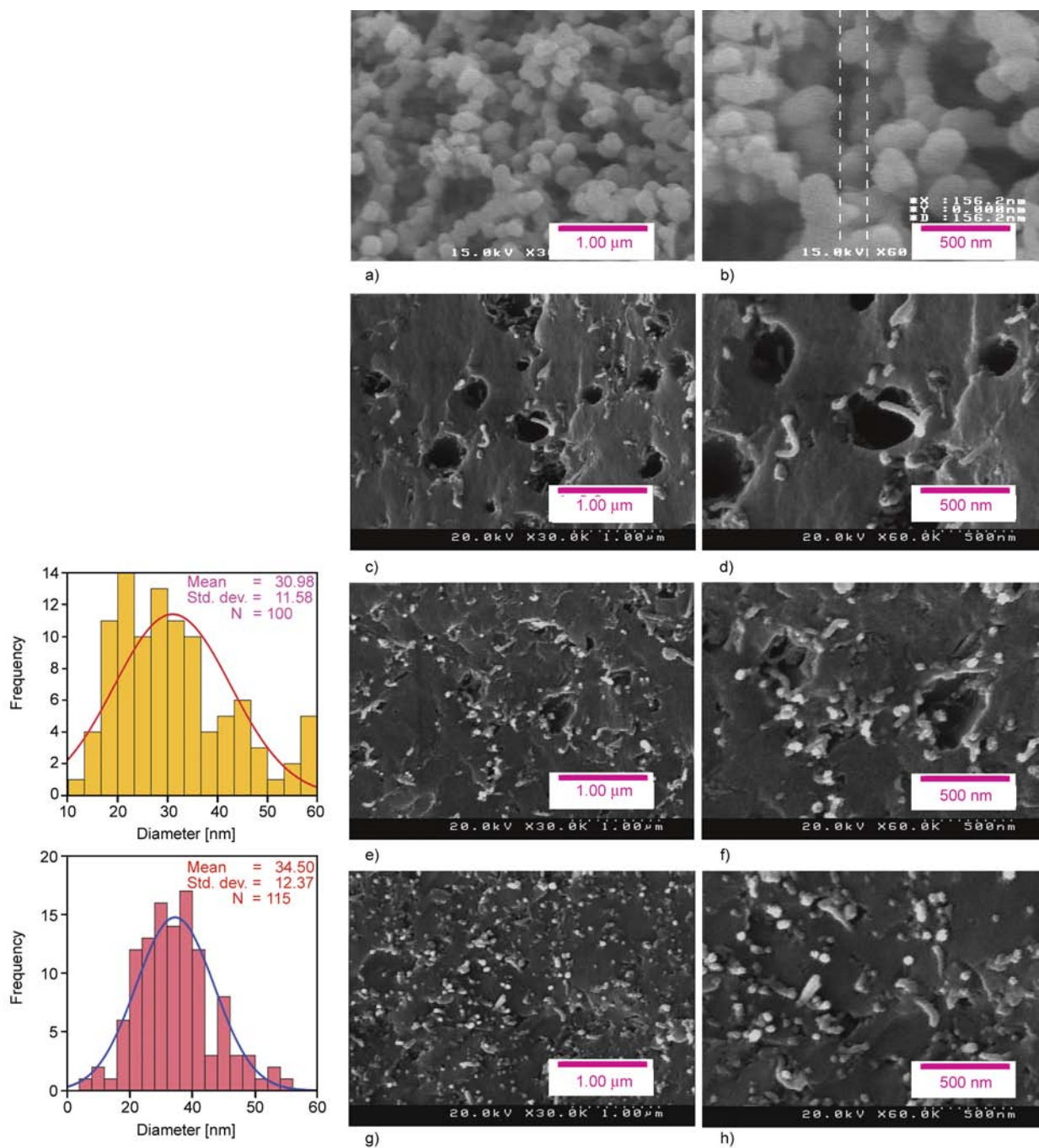[d]Limiting oxygen index (LOI) evaluating at char yield at 800 °C.

Figure 7. FE-SEM photographs of pure PEI (a, b), PEI/Tm-MWCNTs (5 wt%) (c, d), PEI/Tm-MWCNTs (10 wt%) (e, f), PEI/Tm-MWCNTs (15 wt%) (g, h) and size distribution histograms of PEI/Tm-MWCNTs (10, 15 wt%) (e, g)

mal stabilities of the PEI and nanocomposites based on 5 and 10% weight loss (T_5, T_{10}), residue at 800 °C (char yield) and limiting oxygen index (LOI).

Pure PEI did not show substantial weight loss until 387 °C and this value was gradually increased with raising the concentration of Tm-MWCNTs in the nanocomposites, showing that an improvement was achieved due to the presence of Tm-MWCNTs as reinforcement. This could be ascribed to the excellent thermal stability of CNTs and their effective interactions with the PEI matrix.

The extent of surface functionalization can be evaluated by the percentage of weight loss in the TGA curves. The MWCNTs-COOH exhibited approximately a minor weight loss of 10 wt% and the functionalized MWCNTs showed 58 wt%, when the temperature was up to 800 °C. The comparative analysis proved the existence of vitamin B_1 grafted on the surface of MWCNTs. The relative content of vitamin B_1 was determined about 48 wt% (Table 2). LOI could be used to evaluate the flame-retardancy of materials and theoretically predicted in accor-
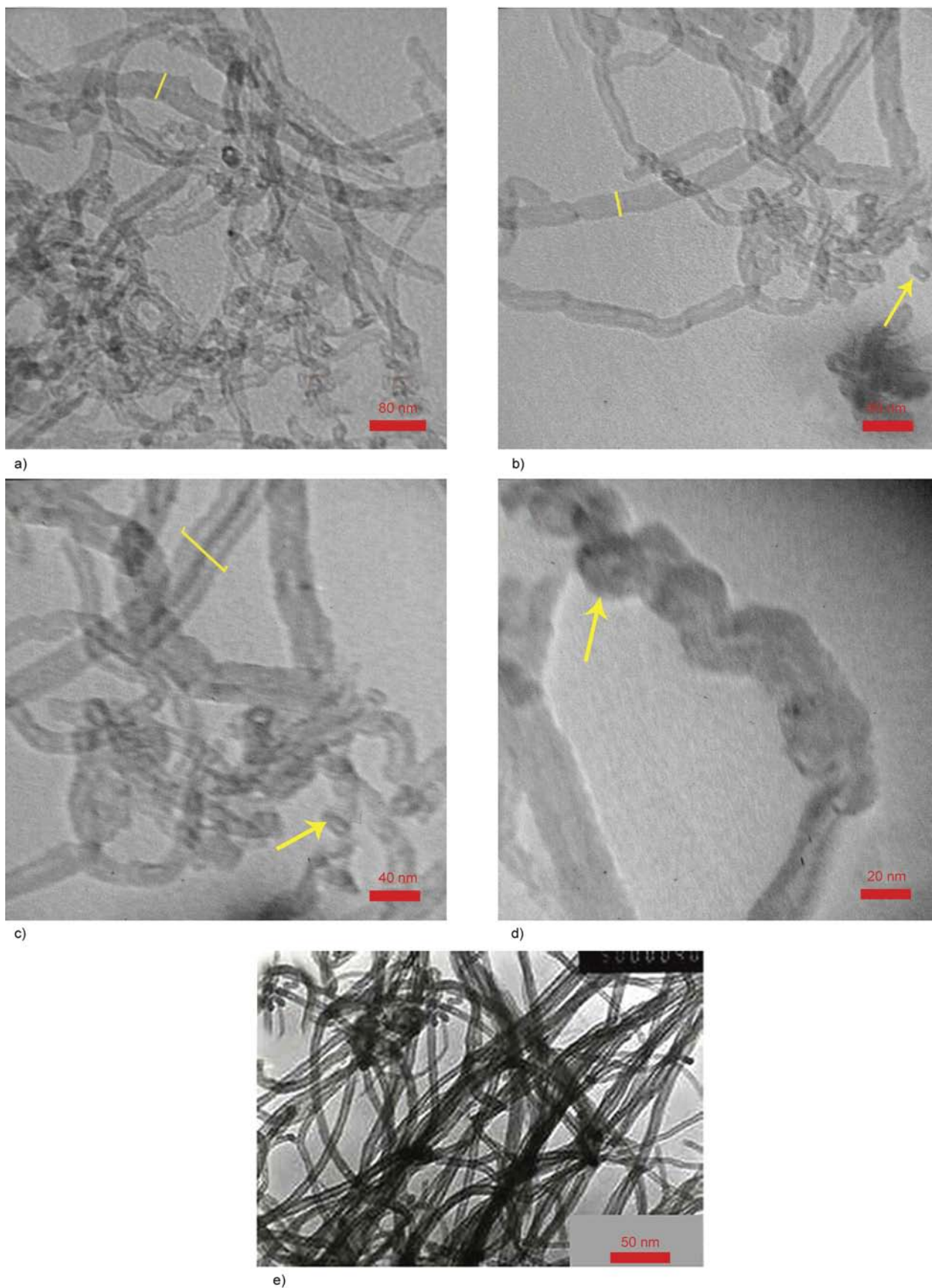
Figure 8. TEM images of Tm-MWCNTs at different magnifications (a–d) and MWCNTs-COOH (e)
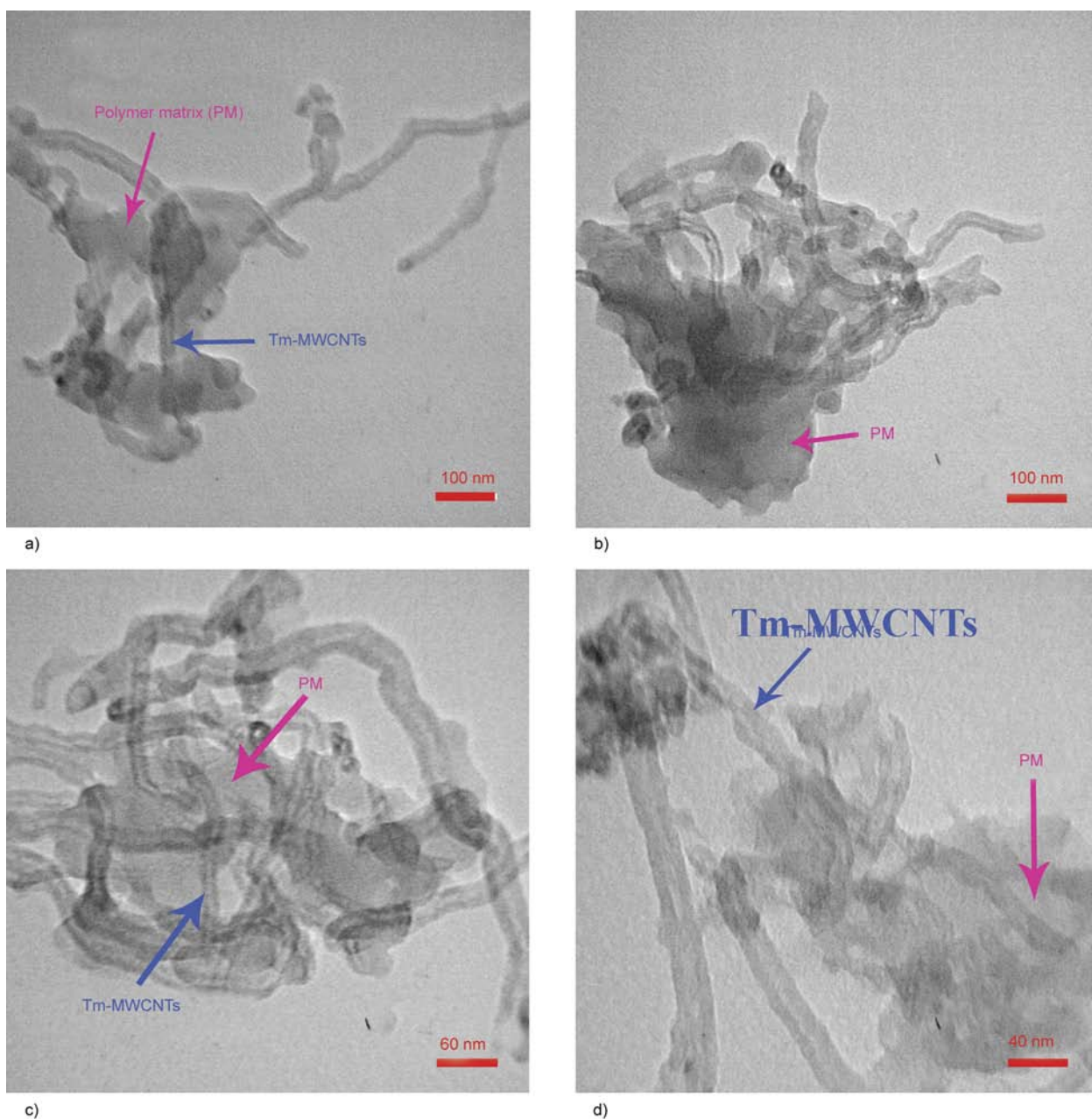
Figure 9. TEM micrographs of PEI/Tm-MWCNTs nanocomposites (10 wt%)
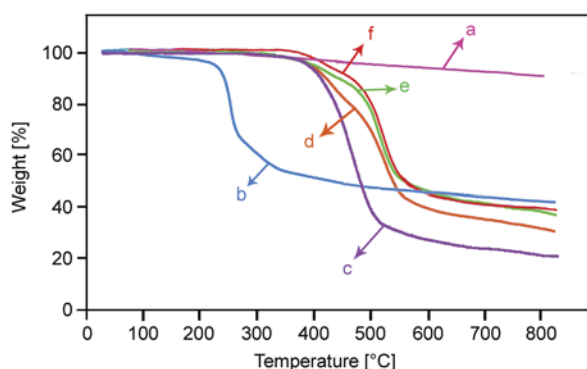
Figure 10. TGA curves of (a) MWCNTs-COOH, (b) Tm-MWCNTs, (c) pure PEI, (d) PEI/Tm-MWCNTs 5 wt%, (e) PEI/Tm-MWCNTs 10 wt%, (f) PEI/Tm-MWCNTs 15 wt%

dance with Van Krevelen and Hoftyzer equation [35]. Materials with an LOI above 28% will demonstrate self-extinguishing behavior. A self-extinguishing material is one that would stop burning after the elimination of the fire or ignition source. The LOI for the pure PEI was obtained 25.5%, while for those of the nanocomposites were in the range of 29.5–32.7%. Therefore, all nanocomposites can be classified as self-extinguishing materials.

LOI = 17,5 + 0,4*CR*, where *CR* = Char yield)

4. Conclusions

In this study, the surface of MWCNTs-COOH was functionalized with vitamin B$_1$ as a biological and

environmental-friendly molecule under ultrasonic irradiation. The chemical functionalization of MWCNTs could improve their compatibility with PEI, leading to better interaction of the polymer chains with Tm-MWCNTs and efficient load transfer from the polymer matrix to the CNTs. The grafting was confirmed by FT-IR spectroscopy, TGA, and electron microscopic techniques. A biodegradable and optically active PEI was synthesized by a direct polycondensation of L-phenylalanine based diacid and 4,4′-thiobis(2-tert-butyl-5-methylphenol) and used as a continuous medium to prepare PEI/Tm-MWCNTs composites. The obtained nanocomposites were studied in the terms of chemical structure, morphology and thermal stability by FT-IR, XRD, TGA, TEM and FE-SEM techniques. Based on TGA data, the comparative extent of grafted vitamin B_1 onto MWCNTs surface was estimated to be around 48 wt%. The incorporation of Tm-MWCNTs into the PEI matrix exhibited obvious improvements in the thermal properties as a result of homogenous and efficient dispersion of CNTs throughout the polymer matrix. Electron microscopic studies revealed that the Tm-MWCNTs were well dispersed and embedded in the PEI matrix, showing good compatibility of Tm-MWCNTs with the polymer matrix.

Acknowledgements

References

[1] Iijima S.: Helical microtubules of graphitic carbon. Nature, **354**, 56–58 (1991).
DOI: 10.1038/354056a0

[2] Alimohammadi F., Gashti M. P., Shamei A.: Functional cellulose fibers *via* polycarboxylic acid/carbon nanotube composite coating. Journal of Coatings Technology and Research, **10**, 123–132 (2013).
DOI: 10.1007/s11998-012-9429-3

[3] Madni I., Hwang C-Y., Park S-D., Choa Y-H., Kim H-T.: Mixed surfactant system for stable suspension of multiwalled carbon nanotubes. Colloids and Surfaces A: Physicochemical and Engineering Aspects, **358**, 101–107 (2010).
DOI: 10.1016/j.colsurfa.2010.01.030

[4] Kruss S., Hilmer A. J., Zhang J., Reuel N. F., Mu B., Strano M. S.: Carbon nanotubes as optical biomedical sensors. Advanced Drug Delivery Reviews, **65**, 1933–1950 (2013).
DOI: 10.1016/j.addr.2013.07.015

[5] Cui L-J., Wang Y-B., Xiu W-J., Wang W-Y., Xu L-H., Xu X-B., Meng Y., Li L-Y., Gao J., Chen L-T., Geng H-Z.: Effect of functionalization of multi-walled carbon nanotube on the curing behavior and mechanical property of multi-walled carbon nanotube/epoxy composites. Materials and Design, **49**, 279–284 (2013).
DOI: 10.1016/j.matdes.2013.01.050

[6] Yesil S.: Effect of carbon nanotube reinforcement on the properties of the recycled poly(ethylene terephthalate)/poly(ethylene naphthalate) (r-PET/PEN) blends containing functional elastomers. Materials and Design, **52**, 693–705 (2013).
DOI: 10.1016/j.matdes.2013.05.101

[7] Mallakpour S., Zadehnazari A.: The production of functionalized multiwall carbon nanotube/amino acid-based poly(amide–imide) composites containing a pendant dopamine moiety. Carbon, **56**, 27–37 (2013).
DOI: 10.1016/j.carbon.2012.12.089

[8] Tang L-C., Zhang H., Han J-H., Wu X-P., Zhang Z.: Fracture mechanisms of epoxy filled with ozone functionalized multi-wall carbon nanotubes. Composites Science and Technology, **72**, 7–13 (2011).
DOI: 10.1016/j.compscitech.2011.07.016

[9] Mallakpour S., Soltanian S.: Investigation on production and characterization of bionanocomposites based on surface functionalized multi-walled carbon nanotubes and optically active poly(ester-imide) having L-isoleucine units. Progress in Organic Coatings, **77**, 1023–1029 (2014).
DOI: 10.1016/j.porgcoat.2014.02.011

[10] Martone A., Faiella G., Antonucci V., Giordano M., Zarrelli M.: The effect of the aspect ratio of carbon nanotubes on their effective reinforcement modulus in an epoxy matrix. Composites Science and Technology, **71**, 1117–1123 (2011).
DOI: 10.1016/j.compscitech.2011.04.002

[11] Liu S., Wang C., Wei Z., Lv W., Fan S., Zhu S., Wang F.: One-step surface modification of multi-walled carbon nanotubes by pyrrole. Materials Letters, **134**, 91–94 (2014).
DOI: 10.1016/j.matlet.2014.07.011

[12] Baibarac M., Baltog I., Lefrant S.: Composites based on conducting polymers and carbon nanotubes. in 'Nanostructured conductive polymers' (ed.: Eftekhari A.) 209–260 (2010).
DOI: 10.1002/9780470661338.ch5

[13] Andrews R., Jacques D., Minot M., Rantell T.: Fabrication of carbon multiwall nanotube/polymer composites by shear mixing. Macromolecular Materials and Engineering, **287**, 395–403 (2002).
DOI: 10.1002/1439-2054(20020601)287:6<395::AID-MAME395>3.0.CO;2-S

[14] Kharissova O. V., Kharisov B. I., Valdés J. J. R., Méndez U. O.: Ultrasound in nanochemistry: Recent advances. Synthesis and Reactivity in Inorganic, Metal-Organic, and Nano-Metal Chemistry, **41**, 429–448 (2011). DOI: 10.1080/15533174.2011.568424

[15] Kotsilkova R., Ivanov E., Bychanok D., Paddubskaya A., Demidenko M., Macutkevic J., Maksimenko S., Kuzhir P.: Effects of sonochemical modification of carbon nanotubes on electrical and electromagnetic shielding properties of epoxy composites. Composites Science and Technology, **106**, 85–92 (2015). DOI: 10.1016/j.compscitech.2014.11.004

[16] Hamciuc C., Vlad-Bubulac T., Petreus O., Lisa G.: Synthesis and characterization of new aromatic polyesters and poly(ester-imide)s containing phosphorous cyclic bulky groups. Polymer Bulletin, **60**, 657–664 (2008). DOI: 10.1007/s00289-008-0901-2

[17] Li C-H., Chen C-C., Chen K-M.: Studies on the synthesis and properties of copolyesterimide. Journal of Applied Polymer Science, **52**, 1751–1757 (1994). DOI: 10.1002/app.1994.070521209

[18] Mehdipour-Ataei S., Bahri-Laleh N., Amirshaghaghi A.: Comparison of one-step and two-step methods of polyimidization and substitution effect in the synthesis of new poly(ester-imide)s with bulky pendent group. Polymer Degradation and Stability, **91**, 2622–2631 (2006). DOI: 10.1016/j.polymdegradstab.2006.05.004

[19] Liaw D-J., Fan C-L., Lin C-C., Wang K-L.: Synthesis and characterization of new soluble poly(ester-imide)s containing noncoplanar 2,2′-dimethyl-4,4′-biphenylene unit. Journal of Applied Polymer Science, **92**, 2486–2493 (2004). DOI: 10.1002/app.20173

[20] Mallakpour S., Kowsari E.: Synthesis of novel optically active poly(ester imide)s by direct polycondensation reaction promoted by tosyl chloride in pyridine in the presence of *N,N*-dimethyformamide. Journal of Applied Polymer Science, **101**, 455–460 (2006). DOI: 10.1002/app.23289

[21] Lienert K-W.: Poly(ester-imide)s for industrial use. Progress in Polyimide Chemistry II, **141**, 45–82 (1999). DOI: 10.1007/3-540-49814-1_2

[22] Mallakpour S., Dinari M.: Progress in synthetic polymers based on natural amino acids. Journal of Macromolecular Science Part A: Pure and Applied Chemistry, **48**, 644–679 (2011). DOI: 10.1080/15226514.2011.586289

[23] Mallakpour S., Soltanian S., Sabzalian M. R.: Fabrication and *in vitro* degradation study of novel optically active polymers derived from amino acid containing diacids and 4,4′-thiobis(2-tert-butyl-5-methylphenol). Journal of Polymer Research, **18**, 1679–1686 (2011). DOI: 10.1007/s10965-011-9573-y

[24] Spitalsky Z., Tasis D., Papagelis K., Galiotis C.: Carbon nanotube–polymer composites: Chemistry, processing, mechanical and electrical properties. Progress in Polymer Science, **35**, 357–401 (2010). DOI: 10.1016/j.progpolymsci.2009.09.003

[25] Tarigh G. D., Shemirani F.: Simultaneous *in situ* derivatization and ultrasound-assisted dispersive magnetic solid phase extraction for thiamine determination by spectrofluorimetry. Talanta, **123**, 71–77 (2014). DOI: 10.1016/j.talanta.2014.01.045

[26] Brahman P. K., Dar R. A., Pitre K. S.: DNA-functionalized electrochemical biosensor for detection of vitamin B$_1$ using electrochemically treated multiwalled carbon nanotube paste electrode by voltammetric methods. Sensors and Actuators B: Chemical, **177**, 807–812 (2013). DOI: 10.1016/j.snb.2012.11.073

[27] Koval'chuk A. A., Shevchenko V. G., Shchegolikhin A. N., Nedorezova P. M., Klyamkina A. N., Aladyshev A. M.: Effect of carbon nanotube functionalization on the structural and mechanical properties of polypropylene/MWCNT composites. Macromolecules, **41**, 7536–7542 (2008). DOI: 10.1021/ma801599q

[28] Amiri A., Maghrebi M., Baniadam M., Zeinali Heris S.: One-pot, efficient functionalization of multi-walled carbon nanotubes with diamines by microwave method. Applied Surface Science, **257**, 10261–10266 (2011). DOI: 10.1016/j.apsusc.2011.07.039

[29] Chua T., Mariatti M., Azizan A., Rashid A. A.: Effects of surface-functionalized multi-walled carbon nanotubes on the properties of poly(dimethyl siloxane) nanocomposites. Composites Science and Technology, **70**, 671–677 (2010). DOI: 10.1016/j.compscitech.2009.12.023

[30] Sahoo N. G., Cheng H. K. F., Bao H., Pan Y., Li L., Chan S. H.: Covalent functionalization of carbon nanotubes for ultimate interfacial adhesion to liquid crystalline polymer. Soft Matter, **7**, 9505–9514 (2011). DOI: 10.1039/C1SM05360D

[31] Martins-Franchetti S. M., Domingos R. N., Trombini R. C.: Modifications on PVC films by ultrasound. Ultrasonics Sonochemistry, **9**, 139–141 (2002). DOI: 10.1016/S1350-4177(01)00121-3

[32] Tahermansouri H., Biazar E.: Functionalization of carboxylated multi-wall carbon nanotubes with 3,5-diphenyl pyrazole and an investigation of their toxicity. New Carbon Materials, **28**, 199–207 (2013). DOI: 10.1016/S1872-5805(13)60077-3

[33] Abuilaiwi F. A., Laoui T., Al-Harthi M., Atieh M. A.: Modification and functionalization of multiwalled carbon nanotube (MWCNT) *via* fischer esterification. The Arabian Journal for Science and Engineering, **35**, 37–48 (2010). DOI: 10.13140/2.1.3447.3925

[34] Pirlot C., Willems I., Fonseca A., Nagy J. B., Delhalle J.: Preparation and characterization of carbon nanotube/polyacrylonitrile composites. Advanced Engineering Materials, **4**, 109–114 (2002). DOI: 10.1002/1527-2648(200203)4:3<109::AID-ADEM109 >3.0.CO;2-5

[35] van Krevelen D.: Properties of polymers. Elsevier, Amsterdam (1976).

Magneto-piezoresistivity in iron particle-filled silicone: An alternative outlook for reading magnetic field intensity and direction

V. Iannotti[1], G. Ausanio[1], L. Lanotte[2], L. Lanotte[1]*

[1]CNR-SPIN and Department of Physics, University of Naples 'Federico II', Piazzale V. Tecchio 80, I-80125 Napoli, Italy
[2]Laboratoire Charles Coulomb, Université de Montpellier, Place Eugène Bataillon – Centre de Biochimie Structurale, 29 rue de Navacelles, 34095 Montpellier, France

Abstract. Elastomagnetic effect (strain induced by magnetic field application) and piezoresistivity (change of electron conductivity due to an induced strain) are coupled in composite materials constituted by magnetic and conductive microparticles into an elastic matrix. On the basis of these effects, the principle of a new method to read magnetization direction changes, in a random sequence, is proposed and experimentally demonstrated. We have produced new composite magneto-piezoresistive samples, constituted of thin chip shaped Fe microparticles inside a silicone matrix, which under an applied magnetic field along their longitudinal axis, undergo an induced strain depending on the local magnetization direction. The resulting resistivity change can be easily detected and used to deduce the local magnetization direction. The magnetization and strain processes are reversible so that after the removal of external magnetizing field the sample is ready for new measurements. A demonstrator prototype has been conceived, produced and tested. The experimental results provide interesting data encouraging to continue the research towards nano-scale devices in order to pursue the intriguing perspective to achieve a magnetic field gradient sensitivity able to reveal magnetization of semipermanent nanomagnets, polarized 'up' and 'down'.

1. Introduction

Composite materials based on polymer matrix filled by conductive or magnetic micro/nano particles have shown very interesting mechanical and electrical properties [1–3], and are very promising for application in aeronautical, mechanical and civil engineering [4–7]. In particular, several investigations have highlighted the existence of a giant piezoresistive effect (the electron conductivity can change by 9 orders of magnitude) in composite materials constituted by a silicone matrix filled by conductive microparticles at a volume fraction around percolation threshold [8–10].

On the other hand, composites made of magnetic particles homogeneously dispersed into an elastic matrix (generally known as magnetorheologic materials) present improved mechanical, thermal and magneto-electric properties under the application of an external magnetic field, during the production or onto the produced composite [11–14]. In particular, the inverse elastomagnetic effect is exhibited: strain appears when its state of magnetization is changed, due to the alignment or rotation of magnetic particles and it is not depending on the intrinsic magnetostriction of the particles [15–19].

---

*Corresponding author, e-mail: lanotte@na.infn.it

When the filling particles inside the polymer matrix are magnetic and conductive (Fe, Ni, FeSi, etc.) concomitant effects of piezoresistivity and elastomagnetism appear in the same sample, and their optimization is obtained by a proper combination of the particle size, shape, volume fraction, magnetic permeability and electrical conductivity. In this way, if the filling particles have no preferential orientation, the application of a longitudinal gradient of magnetic induction produces a sample sensible elongation, independent of both intrinsic magnetostriction and particle rotations. Indeed, this strain is prominently produced by the forces applied by the magnetic field gradient (elastomagnetism). As a result of this strain, a decrease of average distance among the particles and a consequent decrease in resistivity occur (piezoresistivity). These are the fundamental mechanisms in the coupling of elastomagnetism and piezoresistivity which produce the magneto-piezoresistive (MPR) effect extensively treated in [20] and [21]. A magneto-piezoresistive sensitivity (change of resistivity on the inducing magnetic field gradient) higher than 10^{11} Ωm/T has been both predicted by theoretical models and experimentally detected [20, 21].

The main objective of this paper is to establish, by means of some basic experiments in the millimeter scale range, that the MPR effect can be used to detect the change of magnetic polarization direction at a magnetization intensity similar to that produced by the semi-permanent nanomagnets of a magnetic memory.

It does not seem easy to produce samples MPR through the nanowires by keeping the used magnetic interaction between nano-particles of iron in it, but there are some encouraging data in the literature [22, 23]. Nevertheless, the methodology, and operation principles of the sensor proposed here, are very promising and intriguing, and can constitute a basic step to open new perspectives in the field of magnetic reading heads with competitive performance and costs in comparison with standard GMR spin valve.

2. Experimental
2.1. Sample preparation
Iron micro-particles have been used as magnetic filling charge of the MPR composite samples used for this investigation. They have been obtained by mechanical crushing of a pure Fe foil (pureness
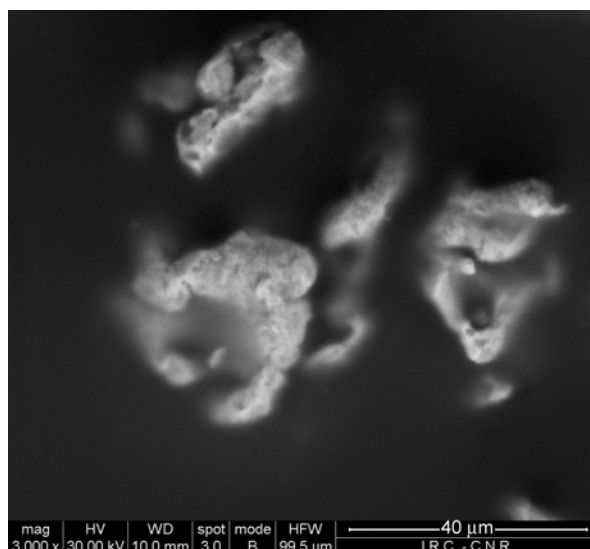
Figure 1. SEM image of iron particles used as filling magnetic/conductive charge

99,99, cod.338141,Aldrich Chemical Company, Inc., U.S.A.) at room temperature and they exhibit a peculiar irregular shape similar to a shrunken little plate or a chip (Figure 1). The elaboration of several SEM images evidenced an average thickness of 7 μm and an average size of particles major axis around 37 μm.

Magnetic particles, at the volume fraction of 39%, were mechanically dispersed into liquid silicone (Essil 291, Axon, France), and hand spatulated carefully for 1 hour, in order to obtain both a homogeneous particle distribution and a good intrusion of silicone among the particle protrusions. After 1 hour of degassing process, at a constant temperature of 40 °C, the solidification process of the polymeric matrix was triggered by adding, and mixing for 20 minutes, a reticulating agent at a percentage of 12% (Essil 292 Catalyseur, Axon, France). Immediately after mixing with the crosslinking agent, the mixture was slowly injected into a Teflon mould $2\times2\times25$ mm^3. The little bar of composite (polymer matrix+magnetic particles) was peeled off from the mould after 48 hours. The sample length can be easily reduced by a laboratory knife. All the process has been described in some detail in previous papers [9, 20, 21]. No methodology has been applied to induce a preferential orientation of the Fe microparticles; therefore they resulted homogeneously distributed and randomly oriented. The peculiar morphology of magnetic particles used in this work is different from the one employed in previous investigations (pseudo-spherical morphology with moderate roughness).

The reason of this choice is to improve composite material performances, delineated on the basis of previous studies [9, 20, 21], in order to achieve three specific characteristics: i) bigger size particles; ii) better silicone entrapping among particle cavities during the mechanical dispersion process to isolate each particle from nearest ones; iii) lower transversal contraction able to give particle contact as consequence of the irregular surface protrusions; iv) preferential in plane magnetization of a single particle due to shape anisotropy. The positive effects of these listed material characteristics were verified by means of the sample performance as will be shown and discussed in Section 3.

2.2. Principles of the experimental demonstrator

The experimental apparatus, specifically arranged to demonstrate the potential of the sensors based on the innovate elastomagnetic composite produced for the present investigation, is shown in Figure 2. The magnet M has a permanent magnetization intensity of $16 \cdot 10^4$ A/m. It produces an initial polariza-
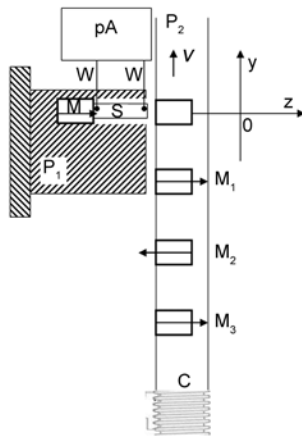

Figure 2. Scheme of the experimental arrangement used to evaluate the capability of a MPR sensor to detect local magnetization direction. S – MPR sample (2 mm×2 mm×6 mm); M – permanent magnet (2 mm×2 mm×3 mm) producing a static polarization of the MPR sample; P_1 – Plexiglas matrix in which M is fixed and S is free to have a variable strain under the action of an additional external magnetizing field; W– microwires for conductive contacts; pA – HP picoammeter to measuring sample electrical resistance; P_2 – sliding Plexiglas holder in which external magnets (M_i, similar to M) are embedded; $M_{i = 1,2,3...}$ – permanent magnets having magnetization direction concordant or opposite to M static polarization; C – mechanical cursor enabling P_2 displacement along y axis, orthogonal to sample longitudinal axis (z).

tion status of the MPR material; in this status the sample resistance is R_0. The magnets M_i (identical in size and magnetization intensity to M) are embedded in the Plexiglas holder P_2 that can run perpendicularly to the longitudinal axis of the MPR sensor core. When a running magnet M_i becomes coaxial with the sample, its magnetizing field adds to initial static polarization induced by the fixed magnet M. As we shall see in the following section, the sample length was designed so that the fields of M and M_i affect only a half of the sample, the one on the side of M and M_i, respectively. On the basis of this experimental expedient, a different MPR core elongation is obtained if the M_i magnetic moment is directed in concordant or opposite direction with respect to M magnetization. According to the MPR model [20, 21], a different sample elongation determines a different decrease of sample initial resistance R_0. We will use the symbol R_{up} for the sample resistance when M and M_i magnetization directions are identical, while we will use R_{down} in case they are opposite.

3. Results and discussion

In Figure 3 the longitudinal magnetization cycle of a MPR sample ($2 \times 2 \times 6$ mm³), produced as described in Section 2, is reported. The magnetization behaviour appears strictly related to both the peculiar morphology of the particles, with a strong shape anisotropy, and the silicone matrix that enables only little rotation of the particles towards the longitudinal magnetizing field axis.

In agreement with these peculiar characteristics of the innovative composite polymer produced for this
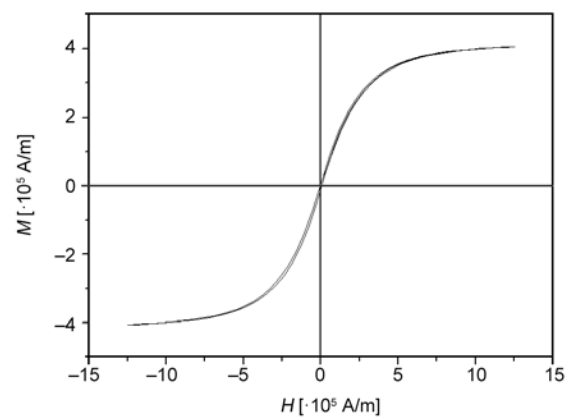

Figure 3. Longitudinal magnetization cycle of the sample constituted by iron microparticles in the volume percentage of 39% homogeneously dispersed into a silicone matrix. Coercive field is 3900 A/m and saturation field higher than 1 MA/m.

investigation, one observes low values of both coercive field and remnant magnetization, together with a progressive approach to saturation of the magnetization that, above $2 \cdot 10^5$ A/m, mainly increases for rotation of magnetic moments towards the applied field axis.

When the magnet M is in contact with the MPR sample S (see scheme in Figure 2) its magnetizing field is not able to homogeneously magnetize all the composite material. In order to monitor this effect, an Hall probe was placed on the MPR sample end located on the opposite side of M magnet (see inset in Figure 4) and, by using samples with variable length l, the magnetization induction B obtained in the MPR material versus the distance l from the magnet pole was measured. Subsequently, the measure of magnetization induction B_0 without MPR sample was performed. The graph in Figure 4 was obtained by calculating $M = (B - B_0)/\mu_0$: at a distance of about 3 mm the magnetization is practically zero. Moreover, also the gradient of magnetic inductions B and B_0 are negligible at a distance from M higher than l/2. This means that, when a magnet M_i is put on the opposite side of M, one can predict the overlap of the magnetization intensity as reported in Figure 5. Since the sample has a length of 6 mm, practically the magnet M gives polarization of Fe particles in one half of the sample, while magnet Mi influences the opposite half of the sample. Since the magnetic induction gradient and the magnetization intensities are practically zero in the sample center, in any case the half of the composite near M is always magnetized in the same way and undertakes the same attractive force towards M, whose longitudinal component is: $F_{1z} = \int_0^{1/2} M_z(\partial B_{0z}/\partial z)\mathrm{d}z$. This force gives an initial con-
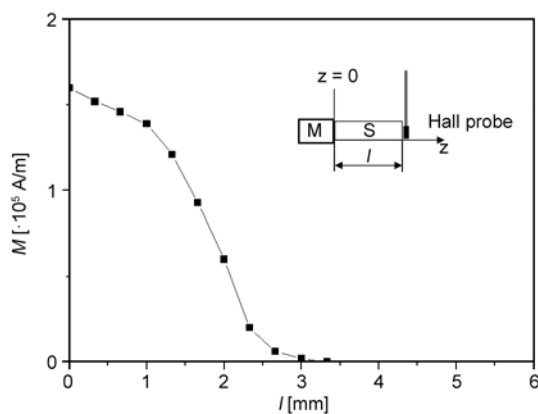

Figure 4. Intensity of magnetization produced statically inside the MPR sample as a function of the distance *l* from the magnet *M*

traction of the interested sample region which determines the conduction status of the MPR sample when M_i action is absent. When the cursor runs and a M_i magnet aligns with sample axis (Figure 2), its presence does not modify the effect of the fixed magnet M. M_i produces induction field gradient and magnetization only in half the sample, the one closer to M_i itself, and a consequent attractive force with a component: $F_{2z} = \int_{1/2}^{1} M_z(\partial B_{0z}/\partial z)\mathrm{d}z$. Since the change of longitudinal magnetizing field, applied by M_i, produces a sign change of both magnetization and magnetic induction gradient, the last force does not change in intensity and direction with direction change of M_i magnetic moment ('up' or 'down'). In conclusion, the MPR core is attracted by the same force towards M_i magnet in any case ('up' or 'down' configuration). The last attractive force produces the same elongation of the MPR sample and an equal resistance decrease.

On the other side, since magnetization cycles exhibit a practically zero remnant magnetization (Figure 3), one can deduce that, also if particle rotations in the elastic matrix occur during the magnetization process, whenever a magnetizing field zero is restored, particle orientations are always randomly distributed around the longitudinal axis of magnetization. This assures that the eventual particle rotations, during the magnetization process in the half sample influenced by M_i gives always a sample elongation independent on magnetization direction. Consequently, also the resistance decrease due to particle rotations is independent of M_i moment direction.

In conclusion, what discriminates the condition 'up' from that 'down' is the fact that the total sensor core strain is also determined by the internal attractive forces that the polarized particles in half sample apply to those ones on the other side. If M and M_i produces the same magnetization directions (configuration 'up'; Figure 5a; see the insert too), the iron particles polarization is the same in all the sample: internal attractive forces are produced that oppose the fixed tensile stress applied by the external magnetic induction gradient and promote a decrement of elongation. On the contrary, if magnetization directions of M and M_i are opposite (configuration 'down'; Figure 5b), iron micro-magnets inside the sample half in proximity of M have a longitudinal magnetic moment anti-parallel with respect those in the sample half closer M_i: repulsive internal forces are present that promote an increment of elongation. Thus,
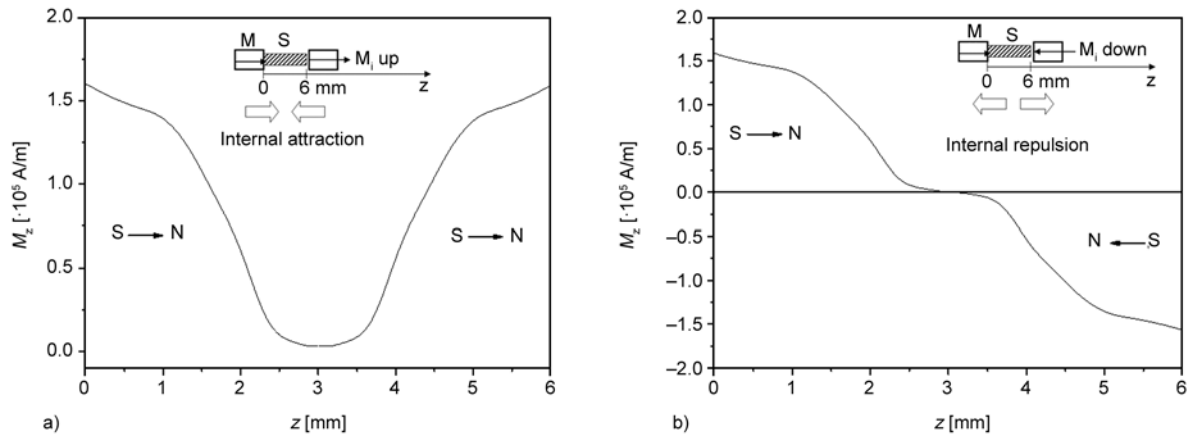
Figure 5. Total behavior of magnetization longitudinal component along the MPR sample as function of the longitudinal coordinate z, in the case of concordant magnetization direction of the external aligned magnets M and M_i (a) and in the case of opposite magnetization directions (b)

in the last case (M_{down}) the sample should have a higher elongation and, on turn, a higher decrease of resistance in comparison with the decrement produced in the condition 'up'.

The scheme in Figure 5 is very effective in explaining the experimental evidences as we will describe below.

The MPR sample resistance has been detected by means of the experimental apparatus described in Section 2, at a displacement velocity of the cursor $C+P_2$ fixed at 1 mm/10 s.

In Figure 6, R behaviour versus the displacement along y axis is reported, starting from the position shown in Figure 2, namely when the P_2 hole in front of the MPR sample is an empty one. On the same figure, along the y axis, the different M_i magnets position is shown, in order to deduce the relative position of external magnets with respect to the sensor core longitudinal axis and their different magnetic polarization directions.

The experimental points are centered in the average R value obtained by several measurement runs. The error bars are contained into the graph point size.

The effects of M_{up} or M_{down} magnets on sample resistance, qualitatively predicted above, are completely verified.

In particular, the resistance decrease ($R_0 - R_{up}$), produced by the alignment of M_{up} magnets with sensor core axis, is around 450 kΩ; while, M_{down} magnets alignment gives ($R_0 - R_{down}$) higher than 700 kΩ. R_{up} and R_{down} values have an average difference higher than 250 kΩ. This enable an easy detection of the M_{up} or M_{down} alignment and a clear discrimination
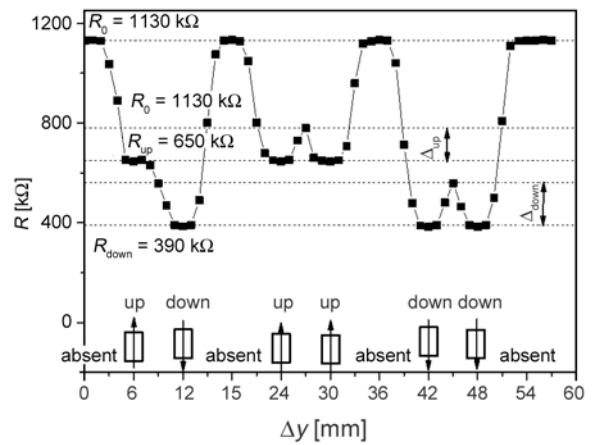
Figure 6. Resistance R of the MPR core measured versus the displacement Δy of the M_i magnets, that, sliding along the y axis (Figure 2), align with the sample z axis, in the sequence reported on the bottom of the figure

between the two cases. Moreover, also the signals produced by a sequence of equal polarization directions, $M_{up} - M_{up}$, or $M_{down} - M_{down}$, can be effectively read. In fact, the two correspondent R minima are well separated by a relative maximum, the amplitude of which, in all cases, exceeds 140 kΩ (Δ_{up} and Δ_{down} in Figure 6).

The running M_i magnets simulate a sequence of registered bits in a magnetic memory and the MPR core works as a reading head, obviously, with a scale factor of about 10^4. Since polymer wires with diameter of 100–200 nm have been already produced [22], as well as iron nanoparticles assembly could maintain magnetic stability down to size of 10–20 nm [23], even if its realization is complex, in

principle it is not to be excluded that the miniaturization of the MPR sensitive core, described in this paper, can achieve similar functionality.

4. Conclusions

A MPR magneto-elastomer constituted by Fe microparticles dispersed into a silicone matrix, at the volume percentage near percolation threshold, was produced on the basis of previous investigation, selecting the particle shape in order to have two main effects: i) improve the capability of entrapping a thin silicone layer among the particles in spite of the high particle density; ii) to give a good magnetization intensity at a moderate external field with a practically reversible magnetization process. A proper experimental system was built in which the MPR material is used as core of a sensor. The last is able to read the magnetization direction in a random sequence of little permanent magnets, which are running orthogonally to the sample longitudinal axis. The sensitive core has a constant square section and its length was properly dimensioned in order that a half of the MPR sample is statically magnetized by a fixed permanent magnet, while the opposite half sample is influenced by the magnetizing field of the external magnets whose magnetization direction should be detected. In this way, the interaction between the two sample halves produces a different elastomagnetic strain distinguishing the external magnetization direction concordant or opposite to the permanent one. In turn, these strains produce different resistance changes which can be detected to determine the exact sequence of polarization directions. So that, if the little magnets are arranged in a binary code, it is easy to read any registered sequence. Taking into account the demonstrated sensitivity (about 1250 kΩ/T), the obtained results constitute a stimulating basis to study the effects of reduction in size, going down to nano-range, on the reported principles and experimental methodology, deeply investigating the potentiality of MPR nanowire (also of different composition with respect that reported in this study) in perspective of innovative and cheap reading heads.

References

[1] Song P., Peng Z-J., Yue Y-L., Zhang H., Zhang Z., Fan Y-C.: Mechanical properties of silicone composites reinforced with micron- and nano-sized magnetic particles. Express Polymer Letters, **7**, 546–553 (2013).
DOI: 10.3144/expresspolymlett.2013.51

[2] Bokobza L.: Multiwall carbon nanotube-filled natural rubber: Electrical and mechanical properties. Express Polymer Letters, **6**, 213–223 (2012).
DOI: 10.3144/expresspolymlett.2012.24

[3] Stassi S., Canavese G.: Spiky nanostructured metal particles as filler of polymeric composites showing tunable electrical conductivity. Journal of Polymer Science Part B: Polymer Physics, **50**, 984–992 (2012).
DOI: 10.1002/polb.23091

[4] Wang J., Dai J., Yarlagadda T.: Carbon nanotube–conducting-polymer composite nanowires. Langmuir, **21**, 9–12 (2005).
DOI: 10.1021/la0475977

[5] Wang L., Li Y.: A review for conductive polymer piezoresistive composites and a development of a compliant pressure transducer. IEEE Transactions on Instrumentation and Measurement, **62**, 495–502 (2013).
DOI: 10.1109/TIM.2012.2215160

[6] Wang L., Li J.: A piezoresistive flounder element based on conductive polymer composite. Sensors and Actuators A: Physical, **216**, 214–222 (2014).
DOI: 10.1016/j.sna.2014.05.010

[7] Patil S. J., Adhikari A., Baghini M. S., Rao V. R.: An ultra-sensitive piezoresistive polymer nano-composite microcantilever platform for humidity and soil moisture detection. Sensors and Actuators B: Chemical, **203**, 165–173 (2014).
DOI: 10.1016/j.snb.2014.06.110

[8] Abyaneh M. K., Ekar S., Kulkarni S. K.: Piezoresistivity and mechanical behavior of metal-polymer composites under uniaxial pressure. Journal of Materials Science Research, **1**, 50–58 (2012).
DOI: 10.5539/jmsr.v1n3p50

[9] Ausanio G., Barone A. C., Campana C., Iannotti V., Luponio C., Pepe G. P., Lanotte L.: Giant resistivity change induced by strain in a composite of conducting particles in an elastomer matrix. Sensors and Actuators A: Physical, **127**, 56–62 (2006).
DOI: 10.1016/j.sna.2005.12.002

[10] Gong S., Zhu Z. H.: Giant piezoresistivity in aligned carbon nanotube nanocomposite: Account for nanotube structural distortion at crossed tunnel junctions. Nanoscale, **7**, 1339–1348 (2015).
DOI: 10.1039/C4NR05656F

[11] Boundenne A., Mamunya Y., Levchenco V., Garnier B., Lebedev E.: Improvement of thermal and electrical properties of Silicone–Ni composites using magnetic field. European Polymer Journal, **63**, 11–19 (2015).
DOI: 10.1016/j.eurpolymj.2014.11.032

[12] Gaska K., Kmita G., Rybak A., Sekula R., Goc K., Kapusta C.: Magnetic-aligned, magnetite-filled epoxy composites with enhanced thermal conductivity. Journal of Materials Science, **50**, 2510–2516 (2015).
DOI: 10.1007/s10853-014-8809-8

[13] Ruiz M., Marchi C., Perez O., Jorge G., Fascio M., D'Accorso N., Negri M.: Structured elastomeric sub-millimeter films displaying magneto and piezo resistivity. Journal of Polymer Science Part B: Polymer Physics, **53**, 574–586 (2015).
DOI: 10.1002/polb.23672

[14] Knaapila M., Høyer H., Kjelstrup-Hansen J., Helgesen G.: Transparency enhancement for photoinitiated polymerization (UV Curing) through magnetic field alignment in a piezoresistive metal/polymer composite. ACS Applied Materials and Interfaces, **6**, 3469–3476 (2014).
DOI: 10.1021/am405625z

[15] Lanotte L., Ausanio G., Iannotti V., Pepe G., Carotenuto G., Netti P., Nicolais L.: Magnetic and magnetoelastic effects in a composite material of Ni microparticles in a silicone matrix. Physical Review B, **63**, 054438/1–054438/6 (2001).
DOI: 10.1103/PhysRevB.63.054438

[16] Lanotte L., Ausanio G., Iannotti V., Luponio C.: Influence of particle pre-orientation on elastomagnetic effect in a composite material of ellipsoidal Ni microparticles in a silicone matrix. Applied Physics A, **77**, 953–958 (2003).
DOI: 10.1007/s00339-002-1939-x

[17] Lanotte L., Ausanio G., Hison C., Iannotti V., Luponio C.: The potentiality of composite elastic magnets as novel materials for sensors and actuators. Sensors and Actuators A: Physical, **106**, 56–60 (2003).
DOI: 10.1016/S0924-4247(03)00133-X

[18] Filipcsei G., Csetneki I., Szilágyi A., Zrínyi M.: Magnetic field-responsive smart polymer composites. Advances in Polymer Science, **206**, 137–189 (2007).
DOI: 10.1007/12_2006_104

[19] Zrinyi M.: Magnetically responsive polymer gels and elastomers: Properties, synthesis and applications. in 'Smart polymers and their applications' (eds: de Aguilar M. R., Roman J. S.) Woodhead Publishing, Cambridge, Part 1, 134–165 (2014)
DOI: 10.1533/9780857097026.1.134

[20] Ausanio G., Hison C. L., Iannotti V., Lanotte L., Lanotte L.: Magneto-piezoresistance in elastomagnetic composites. Journal of Applied Physics, **110**, 063903/1–063903/5 (2011).
DOI: 10.1063/1.3634120

[21] Ausanio G., Iannotti V., Ricciardi E., Lanotte L., Lanotte L.: Magneto-piezoresistance in magnetorheological elastomers for magnetic induction gradient or position sensors. Sensors and Actuators A: Physical, **205**, 235–239 (2014).
DOI: 10.1016/j.sna.2013.10.009

[22] Liu B-T., Huang S-X., Lai M-F., Wei Z-H.: Synthesis of Ag–Ni core–shell nanowires and their application in anisotropic transparent conductive films. RSC Advances, **5**, 1684–1689 (2015)
DOI: 10.1039/C4RA11866A

[23] Allia P., Barrera G., Tiberto P., Nardi T., Leterrier Y., Sangermano M.: Fe_3O_4 nanoparticles and nanocomposites with potential application in biomedicine and in communication technologies: Nanoparticle aggregation, interaction, and effective magnetic anisotropy. Journal of Applied Physics, **116**, 113903/1–113903/9 (2014).
DOI: 10.1063/1.4895837

Influence of pyrolytic carbon black and pyrolytic oil made from used tires on the curing and (dynamic) mechanical properties of natural rubber (NR)/styrene-butadiene rubber (SBR) blends

F. Karabork[1*], *S. T. Tipirdamaz*[2]

[1]Aksaray University, Department of Mechanical Engineering, 68100 Aksaray, Turkey
[2]Aksaray University, Graduate School of Natural and Applied Science, 68100 Aksaray, Turkey

Abstract. Pyrolytic carbon black (CBp) and pyrolytic oil (Op) made from used tires were used in natural rubber (NR)/styrene-butadiene rubber (SBR) blends. The effects of CBp and Op on the processing properties, the mechanical properties and the dynamic mechanical properties of the NR/SBR blends were investigated and compared with a control sample that was prepared with N550 and commercial process oil. It was found that the effect of CBp on the processing properties of the NR/SBR blends was similar to that of N550. With the increase of the CBp content, the curing properties of the NR/SBR blends changed little. The reinforcing effect of CBp was inferior to that of N550. With the increase of the CBp content, the tensile strength, tear strength and modulus at 100% elongation of the NR/SBR vulcanizates decreased significantly. Dynamic mechanical properties of the NR/SBR blends were also affected and all samples comprising CBp have a higher $\tan\delta$ than control sample. It is suggested that the low surface area and high ash content of CBp strongly effects all of these property changes of the NR/SBR blends. The morphology and distribution of the carbon black particles are studied using a scanning electron microscope. It was also found that with the increase of the Op content, the properties of the NR/SBR blends were strongly affected due to the high sulfur content of Op, which produced a high crosslinking density.

Keywords: mechanical properties, pyrolytic carbon black, pyrolytic oil, cure characteristics, dynamical mechanical properties

1. Introduction

The disposal of used tires has become an important issue worldwide and represents a major environmental problem. Therefore, the development of an efficient way to utilize rubber waste is an emerging economic and environmental task faced by the rubber industry worldwide [1–4]. Rubber wastes are chemically crosslinked rubbers and are among the most difficult materials to recycle because they will not dissolve or melt. Tires are a complex mixture of numerous different materials, which include several rubbers, carbon black, steel cord and other organic and inorganic components [5]. This is another reason why used tires are not easily recycled.

Over the years, different alternatives for tire recycling, such as repeated use (retreading), energy recycling (incineration) and grinding have been used, but none of these applications are capable of totally eliminating the waste disposal problem while resulting in adequate profitability. Tire pyrolysis, at present, is an attractive and challenging area of research. The pyrolysis processing of used tires is considered to be an environmentally acceptable and promising disposal method with its high energy recovery and low pollution emission.

---

*Corresponding author, e-mail: fazliyekarabork@hotmail.com

Basically, the pyrolysis process is the thermal decomposition of organic wastes at high temperatures in an oxygen-free environment. The pyrolysis process produces three different fractions: a solid fraction known as char or pyrolytic carbon black (33–38 wt%), a liquid fraction known as pyrolytic oil (38–55 wt%) and a gas fraction (10–30 wt%) [6].

Pyrolytic oil may be used as an industrial fuel after extracting chemical materials. CBp can be used as a filler in asphalt for rheological modification [7, 8]. There are several papers in the literature devoted to the study of tire pyrolysis in liquids and pyrolytic carbon black, and each presents its particular experimental procedure and characterization [6, 9–13] but do not discuss using the products as a process oil and reinforcement additive in rubber compounds, which is focus of this study. In recent years, Du and coworkers [14, 15], Cataldo [16] and Norris *et al*. [17] tested CBp in new rubber compounds. Jie *et al*. [18], Jie *et al*. [19] and Delchev *et al*. [20] investigated the modification of CBp and studied the effect of modified CBp on the properties of NR and SBR vulcanizates. There are fewer reports about Op used in rubbers than about CBp [12, 21].

In this paper, we studied the characteristics of CBp and Op and focused our efforts on the application of CBp and Op in rubber compounds. Rubber compounds are made from a blend of NR/SBR by using several additives. The effects of CBp and Op on the processing properties of NR/SBR compounds and the mechanical and dynamical mechanical properties of NR/SBR vulcanizates were systematically studied and compared with those of commercial carbon black and commercial processing oil.

2. Experimental
2.1. Materials and characterization
The styrene butadiene rubber (SBR 1502; bound styrene (wt%), 22.5, Mooney Viscosity (ML 1+4) at 100 °C, 52), the natural rubber SIR20 (NR) and other curing ingredients (Sulfur, N-Cyclohexyl-2-benzothiazolesulfenamide (CBS), zinc oxide (ZnO) and stearic acid) used in this study, were supplied from Yuksel Rubber Co., Ltd., Konya, Turkey, these ingredients were produced by Bayer AG (Germany). The original carbon black (N550) used in this study was supplied by Tupras Co., Turkey. Octobus N821 used as an original process oil was supplied from Petroyag Chemicals Co., Kocaeli, Turkey. Pyrolytic carbon black (CBp) and pyrolytic oil (Op) were sup-

plied by a local tire pyrolysis plant (Tam Rubber Co., Aksaray, Turkey). The CBp and Op were produced from the used tires by using a fixed bed reactor at a temperature of 500–550 °C in the supplying plant. The CBp was used as a filler in the rubber compound formulation without removing ash or any other purification. The determination of the ash content in CBp was determined according to ASTM D1506. The elemental composition of the CBp was determined by using a Thermo Scientific FLASH 2000 elemental analyzer. The surface area of the CBp was measured using a BET (Brunauer, Emmett and Teller) tester (Quantachrome NovaWin2). The physical properties of the pyrolysis oils were determined according to standards for sulfur content (EN ISO 8754) kinematic viscosity (ASTM D445) and density (ASTM D5002).

2.2. Preparation of rubber compounds
The formulations of the compounds are presented in Table 1. SBR and NR were used in the same ratio (50/50 phr) in all formulations. The amounts of the other additives (ZnO, stearic acid, CBS and sulfur) in the formulations are based on 100 g of rubber. NR/SBR, other additives and various proportions of the CBp or Op were mixed for 15 minutes on an open two-roll mixing mill at room temperature. The first formulation, which is called the control sample, does not contain CBp or Op. Original carbon black and original process oil were partially replaced by the CBp and Op in the other formulations, as shown in Table 1. Samples were identified as PC and PO followed by the sample number, corresponding to the introduction of pyrolytic carbon black and pyrolytic oil, respectively. The cure characteristics of the rubber compounds were characterized using a rheometer, Beijing RADE MR-C3, at 170 °C.

2.3. Measurement of mechanical properties
The tensile properties of the NR/SBR vulcanizates were measured with a Shimadzu AG-IC tensile testing machine, according to ASTM D412, at a testing speed of 500 mm/min. Dumbbell-shaped specimens were punched from compression-molded sheets. The tear strength was tested according to ASTM D624 C with a Gibitre (Tensor Check Profile PC) tensile testing machine. The compression set test was carried out at 100 °C for 24 h, in agreement with ASTM D395-03. The Shore A hardness was measured according to ASTM D 2240. At least three or

Table 1. Formulations of the rubber compounds

Sample code/Ingredients (phr[*])	Control	PC1	PC2	PC3	PC4	PO1	PO2	PO3	PO4
NR/SBR	50/50	50/50	50/50	50/50	50/50	50/50	50/50	50/50	50/50
Carbon black (N550)	50	43.75	37.5	25	0	50	50	50	50
Pyrolytic carbon black (CBp)	0	6.25	12.5	25	50	–	–	–	–
Process oil	20	20	20	20	20	17.5	15	10	0
Pyrolytic oil (Op)	0	–	–	–	–	2.5	5	10	20
ZnO	3	3	3	3	3	3	3	3	3
Stearic acid	1	1	1	1	1	1	1	1	1
CBS	1.8	1.8	1.8	1.8	1.8	1.8	1.8	1.8	1.8
Sulfur	1.75	1.75	1.75	1.75	1.75	1.75	1.75	1.75	1.75

[*]parts per hundred rubber

five samples for each composition were tested, and the average values are reported.

2.4. Dynamic mechanical analysis (DMA)
The dynamic mechanical properties of the NR/SBR vulcanizates were measured with a Perkin Elmer DMA7e in tension mode. The frequency used in this experiment was 1 Hz, with a temperature range from –90 to 60 °C and a heating rate of 5 °C/min.

2.5. Morphology
The morphology of the original carbon black and CBp surfaces and the fracture surfaces of the NR/SBR vulcanizates that were fractured in liquid nitrogen were evaluated with a Fei Quanta 250 FEG scanning electron microscope (SEM). Prior to this operation, the specimens were coated with a thin gold layer.

3. Results and discussion
3.1. Characterization of the pyrolytic carbon black and pyrolytic oil
The most important characteristics of the CBp produced by the tire pyrolysis plant are given in Table 2. An important difference between N550 and CBp is the high ash content, which includes inorganic components. The ash content of CBp is 15.36%, which is much more than that of N550. The most important sources of the inorganic components in CBp are usually ZnO and S, which are used as a curing catalyst and curing agent, respectively, and sometimes mineral fillers or additives such as SiO_2 and Al_2O_3. The composition of the inorganic components in the CBp also depends on the pyrolysis conditions and the quality of the tire feed. The surface area of N550 and CBp was 42 and 30.4 m^2/g, respectively. The lower surface area of the CBp was most probably due to a blockage of a portion of the carbon black

Table 2. Characteristics of pyrolytic carbon black and commercial carbon black

	Specific surface area [m^2/g]	Ash [%]	Sulfur [%]	C [%]	H [%]
CBp	30.4	15.36	1.45	79.15	4.91
N550	42	0.2	0.5	92.36	–

Table 3. Characteristics of pyrolytic oil and commercial oil

	Specific gravity [g/cm^3], at 15 °C	Kinematic viscosity [mm^2/s], at 100 °C	Sulfur [%]
Op	0.937	0.86	2.1
Octobus N821	0.908	8.8	<0.01

surface by carbonaceous deposits [22, 23]. The sulfur content of approximately 1.45% is consistent with literature [6, 13, 24] reports. The residual S in CBp was attributed to the sulfur in the recipe of the tires.

In addition to the ash content and surface area, the surface morphology also plays an important role in the characterization of the carbon black. SEM photos of N550 and CBp are shown in Figure 1a and 1b. The surface morphology of the commercial carbon black shows a rough surface. CBp has a smooth surface due to the deposition of ash and carbonaceous deposits on the surface [22, 23].

The pyrolytic oil was characterized, and the results are presented in Table 3. The specific gravity of Op was found to be higher and the viscosity lower than that of commercial oil. As expected, the sulfur amount in Op was higher than that of commercial oil. This may be explained based on the high content of sulfur in the vulcanization recipe.

3.2. Cure characteristics
The vulcanization curves of the NR/SBR compounds with the additions of CBp and Op are shown in Figure 2a and 2b, respectively. There exist three regions along the vulcanization curves of the compounds
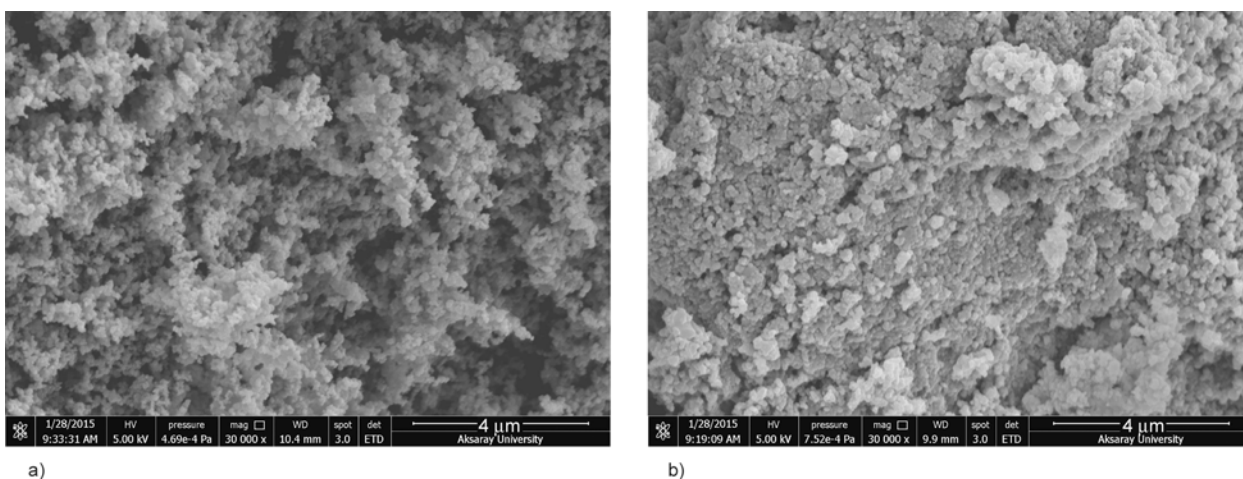
Figure 1. SEM photographs of (a) N550 (b) CBp

containing CBp. The first region is the scorch delay, an induction region during which the majority of the accelerator reactions occur. In this region, the scorch time (ts_2) of the compounds was little or not affected by the addition of the CBp. The minimum torque (M_L), measure of the rubber's resistance to flow during processing increased slightly with the addition of 50 phr CBp. This indicates that the processing of rubber compounds containing only CBp was more difficult than for blends containing commercial carbon black. The second region is the curing reaction period. The optimum cure time (t_{90}), the vulcanization time required to obtain a product with optimum physical characteristics, slightly decreased with the addition of CBp. With the use of only CBp, t_{90} has the lowest value. This is probably due to the some sulfur content of the pyrolytic carbon black. The final region of the vulcanization process is dependent on the crosslink network stability. The modulus can reach a stable plateau (ideal), it can continue to increase (marching modulus), or it can decline (cure reversion). During this period, with the

increase of the CBp content, the maximum torques of the SBR/NR compounds, which are the measure of the compound's final stiffness, are lower than that of the control sample. This should be attributed to the poor reinforcing effect of the CBp in NR/SBR compounds, associated with its smaller surface area [25]. The effect of the Op on the vulcanization curves of the NR/SBR compounds is different from that of CBp, as shown in Figure 2b. The vulcanization curves also have three regions, as in Figure 2a, but the scorch time, optimum cure time, minimum torque and maximum torque of the compounds was significantly affected by the addition and increases in the amount of Op. ts_2 and t_{90} decreased, while M_L and M_H increased. The decreases of ts_2 and t_{90} may be because the content of sulfur in Op is higher than that of the original process oil. The Op can be considered as the sulfur donor, so that the formation of sulfur cross-links was accelerated. The vulcanization process occurs more rapidly when pyrolytic oil is used, as was reported earlier [12]. The increasing of M_H may indicate that NR/SBR compounds loaded
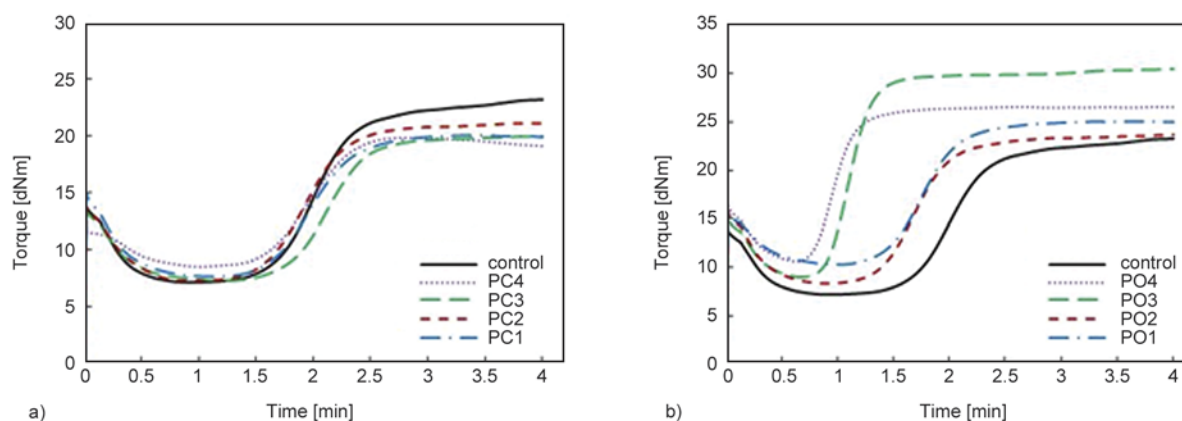

Figure 2. Effects of the (a) CBp and (b) Op on the vulcanization curves of the NR/SBR compounds

with Op tend to become stiff due to the high cross-linking density produced by sulfur curing.

3.3. Mechanical properties

The mechanical properties of the NR/SBR vulcanizates are summarized in Table 4 and 5. CBp and Op showed different effects on the mechanical properties for NR/SBR vulcanizates.

With the increase of the CBp content, all of the properties of the NR/SBR vulcanizates (tensile strength, elongation at break, modulus, tear strength and hardness) except for compression set are decreased. At the higher levels, the CBp (50 phr) gives a larger drop in the mechanical properties relative to the commercial carbon black. The compression set, a measure of the material's elasticity after a prolonged action of compression, gradually increased with the addition of CBp. There are several reasons for these results, such as the surface area and ash content of the pyrolytic carbon black. All of these parameters play a role in rubber reinforcement through different mechanisms such as interfacial interaction between the carbon black and rubber [25, 26]. The measurement of the surface area has been shown to be lower for CBp than for N550 carbon black (approximately 30.4 m^2/g versus 42 m^2/g for N550). It is well known

that the degree of reinforcement increases with a decrease in particle size or an increase in surface area [25]. As the surface area of the carbon black increases, the degree of entanglement between the rubber chains and carbon black particles as well as the degree of crosslinking increases [27, 28]. Therefore, the surface area of carbon black is of great importance for the density of the physical crosslinking. Additionally, in filled rubbers, the fillers act as stress concentrators. The smaller the particle size of the fillers, the more efficient will be the stress transfer from the matrix to the fillers. [25, 29]. Hence, it is understandable that the development of a large polymer-filler interface is the most important factor for the degree of reinforcement provided by the filler [28].

Another factor that may explain the insufficient reinforcing effect of CBp is the high ash content of the pyrolytic carbon black, which limits its use as a reinforcement filler for rubber manufacturing. This means that the real amount of carbon black added to the rubber vulcanizates is only a part of that used in the reference compound filled with N550. The ash content also leads to a low structure, which is the other parameter that affects the reinforcing properties of carbon black in a rubber recipe [16]. There-

Table 4. Effects of pyrolytic carbon black content on mechanical properties of NR/SBR vulcanizates

		Control	PC1	PC2	PC3	PC4
Pyrolytic carbon black	[phr]	0	6.25	12.5	25	50
Elongation at break	[%]	664.31	570.28	548.63	539.82	514.17
Tensile strength	[N/mm^2]	10.91	6.37	5.53	5.13	2.03
100% Modulus	[N/mm^2]	1.68	1.45	1.42	1.35	0.82
200% Modulus	[N/mm^2]	3.04	2.49	2.34	2.21	1.23
300% Modulus	[N/mm^2]	4.62	3.50	3.20	2.88	1.45
Hardness (Shore-A)		52	51	49	45	42
Tear strength	[N/mm]	36.9	28.8	25.6	22.7	14.3
Compression set	[%]	31	34	34	35	41
Density	[g/cm^3]	1.09	1.1	1.08	1.06	1.05

Table 5. Effects of pyrolytic oil content on mechanical properties of NR/SBR vulcanizates

		Control	PO1	PO2	PO3	PO4
Pyrolytic oil	[phr]	0	2.5	5	10	20
Elongation at break	[%]	664.31	697.10	748.69	770.02	732.67
Tensile strength	[N/mm^2]	10.91	10.41	10.29	9.65	11.90
100% Modulus	[N/mm^2]	1.68	1.72	1.74	1.51	2.20
200% Modulus	[N/mm^2]	3.04	3.05	2.97	2.76	3.96
300% Modulus	[N/mm^2]	4.62	4.47	4.31	3.89	5.62
Hardness (Shore-A)		52	54	55	62	58
Tear strength	[N/mm]	36.9	35.1	34.3	26.6	46
Compression set	[%]	31	32	32	36	35
Density	[g/cm^3]	1.09	1.08	1.07	1.11	1.08

fore, the reinforcement effect of CBp is lower compared with that of commercial carbon black. These results are supported by SEM images of the carbon blacks and the fracture surface of the vulcanizates (Figures 1 and 5).

On the other hand, the mechanical properties of NR/SBR vulcanizates obtained from Op loading are quite different from those obtained using CBp, as shown in Table 5. The tensile strength, modulus and tear strength decreased at the loadings of 2.5, 5 and 10 phr, but all of these properties increased remarkably with a loading of over 10 phr. In contrast, the elongation at break, hardness and compression set first increased and then decreased with the additional Op loading. It is well known that the softening effect of process oils leads to improved processing through easier filler incorporation and dispersion, enabling lower processing temperatures and better flow properties [30]. In our opinion, the change in the mechanical properties with the increase of Op content is due to the adverse influence on processing, such as difficult dispersion, slow filler incorporation and inferior flow, due to the low level of purity of Op. However, with the addition of 20 phr Op, the mechanical properties remarkably changed due to the effect of the increasing crosslinking density in the NR/SBR vulcanizates because of the high sulfur content of Op. These results indicate that the pyrolytic and commercial oils interfere with the vulcanized network in different ways. This result is supported by the prior work by Roy *et al*. [12], as well as by the cure properties of NR/SBR compounds.

3.4. Dynamic mechanical properties

The dynamic mechanical behavior of the rubber vulcanizates is the other indicator of the reinforcing effect of CBp. The mechanical loss tangent ($\tan \delta$) is the ratio between the dynamic loss modulus (E'') and the dynamic storage modulus (E') ($\tan \delta = E''/E'$). It naturally represents the macromolecular mobility of the chains and the polymer phase transitions [31–33]. It is accepted that a higher $\tan \delta$ indicates greater mechanical losses, which are related to the high energy input required for the motion of the molecular chains of the polymer as the transition is approached [34, 35].

Figure 3a shows the effect of CBp loading on $\tan \delta$ as a function of the test temperature. It is well known that the $\tan \delta$ peak corresponds to the glass transition temperature (T_g). It can be seen that $\tan \delta$ shows a peak at temperatures between –60 and –10 °C, known as a transition region. By incorporating CBp, the height of the $\tan \delta$ peak and the glass transition temperature change slightly due to the rubber-filler interaction. It is well known that the rubber-filler interaction increases with the increasing surface area of carbon black, reducing the chain mobility and transferring less mechanical energy to the rubber molecules, so that tan δmax decreases [36]. The $\tan \delta$ first increased and then decreased by increasing the CBp level, but all samples comprising CBp have a higher $\tan \delta$ than control sample. The results also suggest that increasing the CBp content causes a decrease in the elastic behavior (increased tan δmax) due to the decreased real amount of carbon black upon increasing the CBp content. The storage moduli were effected by the amount of CBp added as shown in Figure 3b. Accordingly [37], the hydrodynamic reinforcement occurs in the rubber composites filled with the conventional fillers such as CB, giving rise to an increase in the modulus in polymer matrix. The storage modulus (E') values decreased with the
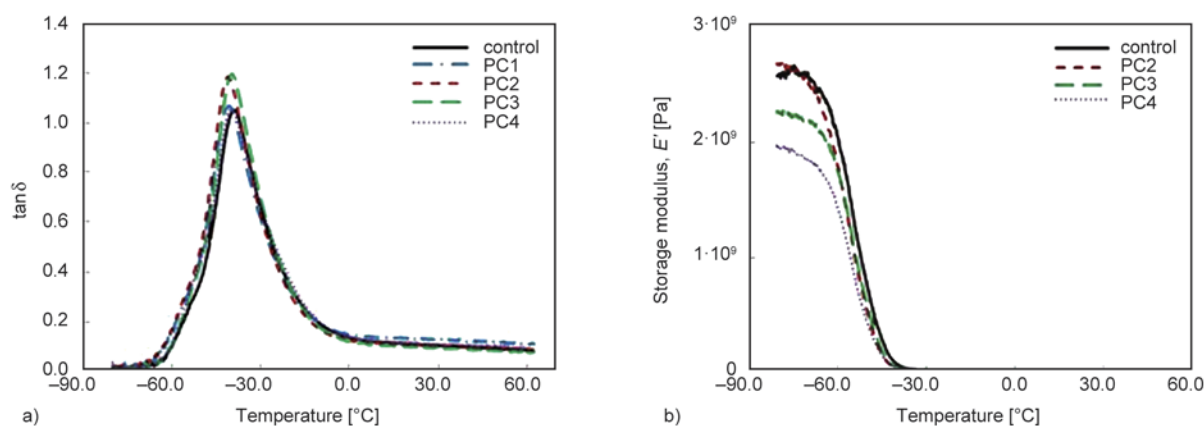

Figure 3. Effect of CBp on (a) $\tan \delta$ and (b) storage modulus as a function of temperature for NR/SBR vulcanizates

increasing CBp amount. This is due to the weaker reinforcing effect of CBp than that of N550s in the NR/SBR matrix as discussed earlier. The obtained results for the dynamic mechanical properties of the investigated NR/SBR vulcanizates can be explained by the difference in the morphology, structure and surface area of the two types of fillers.

The height of the $\tan\delta$ peak decreased and the storage modulus (E') values increased as the Op content increased (Figure 4a and 4b). The results suggest that increasing the Op content caused an increase in the elastic behavior. This is probably due to the increased crosslinking density. The results obtained for the dynamic mechanical properties of the investigated NR/SBR vulcanizates containing Op can be explained by the difference in the plasticizer effects of Op and commercial oil.

In addition, the results of DMA testing of the rubber compounds has also been shown to be a predictor of the compound's performance [38]. SBR/NR blends are used in tire tread compounds for passenger car due to the good wet traction and rolling resistance [39]. Comparison of the $\tan\delta$ values of the compounds from this study and other studies was given in Table 6. A high $\tan\delta$ at 0 °C is correlating with good wet traction and a low $\tan\delta$ at 60 °C correlating with low rolling resistance [40]. Generally, it is difficult to obtain a high $\tan\delta$ at 0 °C and at the same time a low $\tan\delta$ at 60 °C. Therefore, a balance between the $\tan\delta$ values at 0 and 60 °C may suggest the suitable tire tread compound [40]. Both the $\tan\delta$ at 0 °C and the $\tan\delta$ at 60 °C are obtained in this study is lower than commercial tire treads [38]. The
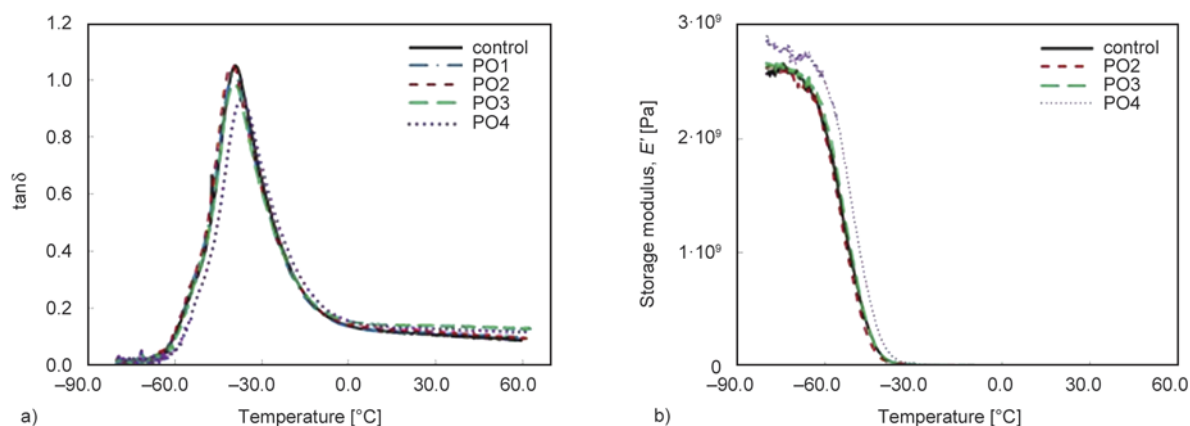

Figure 4. Effect of Op on (a) $\tan\delta$ and (b) storage modulus as a function of temperature for NR/SBR vulcanizates

Table 6. Comparison of the $\tan\delta$ values of the compounds

	This study			Literature				
	Control	**PC4**	**PO4**	**Waddel et al., 1990 [39]**	**Kim et al., 2009 [41]**	**Terrill et al., 2010 [38]***		
						(3287)**	**(3229)****	**(3034)****
Ingredients [phr]								
SBR	50	50	50	50	100	–	–	–
NR	50	50	50	50	–			
Carbon black	50	–	50	45	35			
Silica	–	–	–	–	20			
Pyrolytic carbon black (CBp)	–	50	–	–	–			
Process oil	20	20	–	9	2			
Pyrolytic oil (Op)	–	–	20	–	–			
ZnO	3	3	3	3	3			
Stearic acid	1	1	1	1	1.6			
Sulfur	1.75	1.75	1.75	1.6	1			
Dynamic mechanical properties								
$\tan\delta$ at 0 °C	0.138	0.136	0.155	0.139	0.266	0.174	0.184	0.226
$\tan\delta$ at 60 °C	0.090	0.097	0.115	–	0.169	0.108	0.119	0.178
Ratio of the $\tan\delta$ (0 °C)/$\tan\delta$ (60 °C)	1.53	1.40	1.35	–	1.57	1.61	1.55	1.27

*Terrill et al. [38], 2010, forty-eight commercial tire treads were investigated by authors for prediction of rolling resistance and wet traction. Three samples were given here.
**Barcode numbers are given by the authors.

ratios of the $\tan\delta$ (0 °C)/$\tan\delta$ (60 °C) were obtained in this study are well satisfied with the literature.

3.5. Morphology

Scanning electron micrographs of the fractured surfaces of rubber vulcanizates containing N550 and CBp are shown in Figure 5. The carbon black mainly exists as aggregates in the rubber matrix [42]. In the SEM of all of the NR/SBR vulcanizates, carbon black aggregates can be easily distinguished. The carbon black aggregates for N550 have smaller sizes than the CBp aggregates. As Table 2 demonstrates, N550 has a higher specific surface area than CBp. With the increase of the CBp content, the interfaces between the CBp aggregates and the NR/SBR matrix are apparent. Desirable interaction between the molecules of rubber and carbon black does not exist between the CBp and the NR/SBR matrix due to the surface properties of CBp such as its surface area and the ash on the surface. Hence, CBp has a weaker reinforcing performance than that of N550s in the NR/SBR matrix, which is in agreement with the other conclusions from our experimental results.

On the other hand, the quality of the carbon black containing rubber is extremely dependent on the degree of dispersion the carbon black particles achieved inside the rubber matrix [43]. With the increased CBp loading the fractured surfaces show that the filler is nonuniformly dispersed in the NR/SBR matrix, and the particle size distribution is extended. These results, as seen from Figure 5, lead to the low mechanical properties.

4. Conclusions

In this work, the properties of the NR/SBR blends with the addition of CBp or Op were studied. The following conclusions can be drawn:

- The processability of the blends did not change meaningfully with the increase of the CBp content. However, the processability of the blends is significantly affected by the addition and increases in the amount of the Op. ts_2 and t_{90} were decreased due to the high sulfur content of Op. Vulcanization reactions occurred more rapidly, and the high sulfur content also affected M_L and M_H, which increased due to the high crosslinking density.
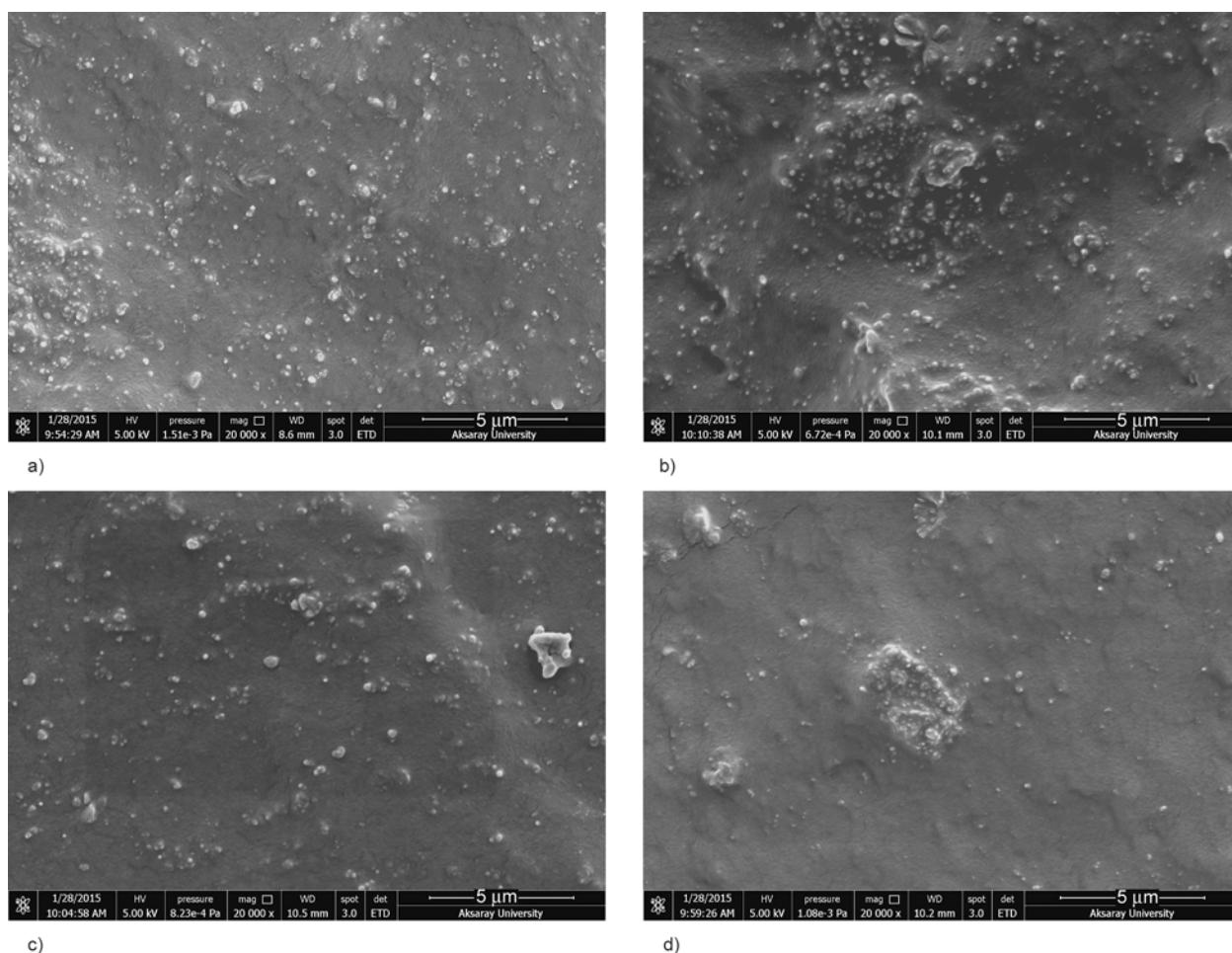

Figure 5. SEM photographs of NR/SBR vulcanizates (a) control (b) PC2 (c) PC3 (d) PC4

- The NR/SBR vulcanizates with increasing CBp content have lower mechanical properties compared with the commercial CB due to the high ash content and low surface area of the pyrolytic carbon black. From this result, it has been found that CBp cannot replace commercial carbon black in a recipe at equal parts, but it may be added in a small amount, or the drop in the mechanical properties may become unacceptable. On the other hand, the mechanical properties of NR/SBR vulcanizates obtained from Op loading were significantly affected by the addition and increases in the amount of the Op. The tensile strength, modulus and tear strength decreased at loadings of 2.5, 5 and 10 phr, but all of these properties increased remarkably with a loading of over 10 phr. In contrast, the elongation at break, hardness and compression set first increased and then decreased with the additional Op loading. This is due to the low influence on the processing because of the chemical composition.

- With the increase in CBp, NR/SBR vulcanizates have a higher $\tan\delta$, which causes a decrease in the elastic behavior compared with the control sample due to the decreasing rubber-filler interaction with the decreasing surface area of CBp. However, the height of the $\tan\delta$ peak reduced with the increase of the Op content. The results suggest that increasing the Op content causes an increase in the elastic behavior. This is probably due to the increased crosslinking density.

- In this work, the variations in the specific surface area, ash content and sulfur content of the carbon blacks and also the variations in the chemical composition of the process oils were found to cause significant changes in the properties of the NR/SBR blends. If the CBp and Op are modified, before adding them to the rubber recipe, they may improve certain properties of the rubber blends.

Acknowledgements

References

[1] Lamminmäki J., Li S., Hanhi K.: Feasible incorporation of devulcanized rubber waste in virgin natural rubber. Journal of Materials Science, **41**, 8301–8307 (2006).
DOI: 10.1007/s10853-006-1010-y

[2] Adhikari B., De D., Maiti S.: Reclamation and recycling of waste rubber. Progress in Polymer Science, **25**, 909–948 (2000).
DOI: 10.1016/S0079-6700(00)00020-4

[3] Karabork F., Pehlivan E., Akdemir A.: Characterization of styrene butadiene rubber and microwave devulcanized ground tire rubber composites. Journal of Polymer Engineering, **34**, 543–554 (2014).
DOI: 10.1515/polyeng-2013-0330

[4] Karger-Kocsis J., Mészáros L., Bárány T.: Ground tyre rubber (GTR) in thermoplastics, thermosets, and rubbers. Journal of Materials Science, **48**, 1–38 (2013).
DOI: 10.1007/s10853-012-6564-2

[5] Laresgoiti M. F., Caballero B. M., de Marco I., Torres A., Cabrero M. A., Chomón M. J.: Characterization of the liquid products obtained in tyre pyrolysis. Journal of Analytical and Applied Pyrolysis, **71**, 917–934 (2004).
DOI: 10.1016/j.jaap.2003.12.003

[6] Helleur R., Popovic N., Ikura M., Stanciulescu M., Liu D.: Characterization and potential applications of pyrolytic char from ablative pyrolysis of used tires. Journal of Analytical and Applied Pyrolysis, **58–59**, 813–824 (2001).
DOI: 10.1016/S0165-2370(00)00207-2

[7] Yousefi A. A., Ait-Kadi A., Roy C.: Effect of used-tire-derived pyrolytic oil residue on the properties of polymer-modified asphalts. Fuel, **79**, 975–986 (2000).
DOI: 10.1016/S0016-2361(99)00216-1

[8] Kebritchi A., Firoozifar H., Shams K., Jalali-Arani A.: Effect of pre-devulcanization and temperature on physical and chemical properties of waste tire pyrolytic oil residue. Fuel, **112**, 319–325 (2013).
DOI: 10.1016/j.fuel.2013.04.054

[9] Kyari M., Cunliffe A. M., Williams P. T.: Characterization of oils, gases, and char in relation to the pyrolysis of different brands of scrap automotive tires. Energy Fuels, **19**, 1165–1173 (2005).
DOI: 10.1021/ef049686x

[10] Aguado R., Olazar M., Vélez D., Arabiourrutia M., Bilbao J.: Kinetics of scrap tyre pyrolysis under fast heating conditions. Journal of Analytical and Applied Pyrolysis, **73**, 290–298 (2005).
DOI: 10.1016/j.jaap.2005.02.006

[11] Fernández A. M., Barriocanal C., Alvarez R.: Pyrolysis of a waste from the grinding of scrap tyres. Journal of Hazardous Materials, **203–204**, 236–243 (2012).
DOI: 10.1016/j.jhazmat.2011.12.014

[12] Roy C., Chaala A., Darmstadt H.: The vacuum pyrolysis of used tires: End-uses for oil and carbon black products. Journal of Analytical and Applied Pyrolysis, **51**, 201–221 (1999).
DOI: 10.1016/S0165-2370(99)00017-0

[13] Martínez J. D., Murillo R., García T.: Production of carbon black from the waste tires pyrolysis. Boletín del Grupo Español Carbón, **30**, 10–14 (2013).

[14] Du A., Zhang Z., Wu M.: The effect of pyrolytic carbon black prepared from junked tires on the properties of ethylene-propylene-diene copolymers (EPDM). Express Polymer Letters, **3**, 295–301 (2009).
DOI: 10.3144/expresspolymlett.2009.37

[15] Du A. H., Wu M. S., Su C. Y., Chen H.: The characterization of pyrolytic carbon black prepared from used tires and its application in styrene–butadiene rubber (SBR). Journal of Macromolecular Science Part B: Physics, **47**, 268–275 (2008).
DOI: 10.1080/00222340701748768

[16] Cataldo F.: Preparation of pyrolytic carbon black from scrap tire rubber crumb and evaluation in new rubber compounds. Macromolecular Materials and Engineering, **290**, 463–467 (2005).
DOI: 10.1002/mame.200400388

[17] Norris C. J., Hale M., Bennett M.: Pyrolytic carbon: Factors controlling in-rubber performance. Plastics, Rubber and Composites, **43**, 245–256 (2014).
DOI: 10.1179/1743289814Y.0000000088

[18] Jie Z., Yong-rong Y., Xiao-hong R., Siegfried S.: Investigation of reinforcement of the modified carbon black from wasted tires by nuclear magnetic resonance. Journal of Zhejiang University SCIENCE A, **7**, 1440–1446 (2006).
DOI: 10.1631/jzus.2006.A1440

[19] Jie Z., Shengji W., Tianming Y., Zhengmiao X.: Modified pyrolytic carbon black from scrap tires and its reinforcement performance in natural rubber. in 'International Conference on Computer Distributed Control and Intelligent Environmental Monitoring, Changsha, Hunan, China' 472–475 (2011).
DOI: 10.1109/CDCIEM.2011.82

[20] Delchev N., Malinova P., Mihaylov M., Dishovsky N.: Effect of the modified solid product from waste tyres pyrolysis on the properties of styrene-butadiene rubber based composites. Journal of Chemical Technology and Metallurgy, **49**, 525–534 (2014).

[21] Leblanc J. L., Roy C., Mirmiran S., Benallal B., Schwerdtfeger A. E.: The plasticizing properties of heavy oils obtained from the vacuum pyrolysis of used tires. Kaustschuk und Gummi Kunststoffe, **49**, 194–199 (1996).

[22] Darmstadt H., Roy C., Kaliaguine S., Joo C. S., Ryoo R.: Pore structure and graphitic surface order of mesoporous carbon molecular sieves by low-pressure nitrogen adsorption. in 'International Conference on Carbon, Lexington, USA' p.9 (2001).

[23] Pantea D., Darmstadt H., Kaliaguine S., Roy C.: Heat-treatment of carbon blacks obtained by pyrolysis of used tires. Effect on the surface chemistry, porosity and electrical conductivity. Journal of Analytical and Applied Pyrolysis, **67**, 55–76 (2003).
DOI: 10.1016/S0165-2370(02)00017-7

[24] Kaminsky W., Mennerich C.: Pyrolysis of synthetic tire rubber in a fluidised-bed reactor to yield 1,3-butadiene, styrene and carbon black. Journal of Analytical and Applied Pyrolysis, **58–59**, 803–811 (2001).
DOI: 10.1016/S0165-2370(00)00129-7

[25] Manoj K. C., Kumari P., Unnikrishnan G.: Cure characteristics, swelling behaviors, and mechanical properties of carbon black filler reinforced EPDM/NBR blend system. Journal of Applied Polymer Science, **120**, 2654–2662 (2011).
DOI: 10.1002/app.33476

[26] Donnet J. B.: Carbon black: Science and technology. CRC Press, New York (1993).

[27] Litvinov V. M., Steeman P. A. M.: EPDM–carbon black interactions and the reinforcement mechanisms, as studied by low-resolution ^{1}H NMR. Macromolecules, **32**, 8476–8490 (1999).
DOI: 10.1021/ma9910080

[28] Li Z. H., Zhang J., Chen S. J.: Effects of carbon blacks with various structures on vulcanization and reinforcement of filled ethylene-propylene-diene rubber. Express Polymer Letters, **2**, 695–704 (2008).
DOI: 10.3144/expresspolymlett.2008.83

[29] Wang M-J.: Effect of polymer-filler and filler-filler interactions on dynamic properties of filled vulcanizates. Rubber Chemistry and Technology, **71**, 520–589 (1998).
DOI: 10.5254/1.3538492

[30] Zweifel H., Maier R. D., Schiller M.: Plastics additives handbook. 6th ed, Hanser Press, Munich (2009).

[31] Brydson J. A.: Rubbery materials and their compounds, Elsevier, London (1988).

[32] Sombatsompop N.: Dynamic mechanical properties of SBR and EPDM vulcanisates filled with cryogenically pulverized flexible polyurethane foam particles. Journal of Applied Polymer Science, **74**, 1129–1140 (1999).
DOI: 10.1002/(SICI)1097-4628(19991031)74:5<1129 ::AID-APP9>3.0.CO;2-Q

[33] Zaimova D., Bayraktar E., Katundi D., Dishovsky N.: Elastomeric matrix composites: Effect of processing conditions on the physical, mechanical and viscoelastic properties. Journal of Achievements in Materials and Manufacturing Engineering, **50**, 81–91 (2012).

[34] Gonzalez L., Rodriguez A., Valentin J. L., Marcos-Fernandez A., Posadas P., Kunstst K. G.: Conventional and efficient cosslinking of natural rubber. Kautschuk und Gummi Kunststoffe, **58**, 638–643 (2005).

[35] Al-Hartomy O. A., Al-Solamy F., Al-Ghamdi A., Dishovsky N., Ivanov M., Mihaylov M., El-Tantawy F.: Influence of carbon black structure and specific surface area on the mechanical and dielectric properties of filled rubber composites. International Journal of Polymer Science, 521985/1–521985/8 (2011).
DOI: 10.1155/2011/521985

[36] Chuayjuljit S., Imvittaya A., Na-Ranong N., Potiyaraj P.: Effects of particle size and amount of carbon black and calcium carbonate on curing characteristics and dynamic mechanical properties of natural rubber. Journal of Metals, Materials and Minerals, **12**, 51–57 (2002).

[37] Zhou X-W., Zhu Y-F., Liang J.: Preparation and properties of powder styrene–butadiene rubber composites filled with carbon black and carbon nanotubes. Materials Research Bulletin, **42**, 456–464 (2007).
DOI: 10.1016/j.materresbull.2006.06.027

[38] Terrill E. R., Centea M., Evans L. R., MacIsaac Jr. J. D.: Dynamic mechanical properties of passenger and light truck tire treads. Report No. DOT HS 811 270, U.S. Department of Transportation, National Highway Traffic Safety Administration, p.28 (2010).

[39] Waddell W. H., Bhakuni R. S., Barbin W. W., Sandstrom P. H.: Pneumatic tire compounding. The Goodyear Tire and Rubber Company, Akron (1990).

[40] Ko J. Y., Prakashan K., Kim J. K.: New silane coupling agents for silica tire tread compounds. Journal of Elastomers and Plastics, **44**, 549–562 (2012).
DOI: 10.1177/0095244312439489

[41] Kim W-S., Lee D-H., Kim I-J., Son M-J., Kim W., Cho S-G.: SBR/organoclay nanocomposites for the application on tire tread compounds. Macromolecular Research, **17**, 776–784 (2009).
DOI: 10.1007/BF03218614

[42] Eirich F. R.: Science and technology of rubber. Academic Press, New York (1978).

[43] Dai S., Ao G., Kim M. S.: Reinforcement of rubbers by carbon black fillers modified by hydrocarbon decomposition. Journal of Industrial and Engineering Chemistry, **13**, 1162–1168 (2007).